Design and Analysis of Multiband Fractal Antenna

by

Vivek Dhoot

201021002

A thesis submitted in the partial fulfillment of the requirements for the degree of

Doctor of Philosophy

in

Information and Communication Technology

to

Dhirubhai Ambani Institute of Information and Communication Technology

Gandhinagar, India

December 2015

Dedicated to 6 Gods of my life;

My Father: Mr. Kamal Kishore Dhoot,

My Mother: Mrs. Shashi Kala Dhoot,

My Sister: Mrs. Arpana Bhangariya,

My Brother: Mr. Neelesh Dhoot,

MaM: Me and Myself, and

Shree Radheshyam

Declaration

This is to certify that

i) the thesis comprises my original work towards the degree of Doctor of Philosophy in Information and Communication Technology at DA-IICT and has not been submitted elsewhere for a degree.

ii) due acknowledgment has been made in the text to all other material used.

Signature of Student

Vivek Dhoot

Certificate

This is to certify that the thesis work entitled *Design and Analysis of Multiband Fractal Antenna* has been carried out by *Vivek Dhoot (201021002)* for the degree of Doctor of Philosophy in Information and Communication Technology at this Institute under my supervision.

Thesis Supervisor

Prof. Sanjeev Gupta

Acknowledgements

This is not copy of views of any other person. This is purely my own words and my own view. I want to thank everyone who has helped me during my research work. First of all, my guide: Prof. Sanjeev Gupta, I would like to thank him for his clear, directive, positive and supportive approach. His exceptional knowledge of RF/Microwave engineering gave me enormous amount of encouragement towards my research. I really believe that if your guide is like Prof. Sanjeev Gupta, half of the pressure is already released due to his enthusiastic attitude towards learning. He treats his students as his own children and helps them in every aspect. He has not only taught me technicality but also professionalism. Entire vocabulary is not sufficient to explain a teacher of his sort. Thanks a lot for giving me this opportunity to work under him. I am honored to have him as my supervisor.

I have to thank Prof. Deepak Ghodgaonkar and Prof. Mukesh Tiwari, for their consistent suggestions on my research work. It helped me in keeping myself focused towards goal. I really admire and thank them both for it.

I would like to thank my family members also for their patience during my research work. I used to become frustrated during my research when results were not obtained, but my family was always there to pull me up and listen to me. Its really important that people around you, listen to your thoughts. I really appreciate that. Thanks to all of them.

I would like to thank few of my other friends and colleagues too, Ramesh Prajapati (For helping in lab for providing support on time for antenna material and connectors etc.), Ashish (For helping me in submissions of Thesis to Institute) Nilay Khatri, Bhavin Shiyani, Riyaz Panarwala and Amit Patel.

Vivek Dhoot

Abstract

Miniaturized Multiband antenna design is an important and challenging task for communication industry. Several constraints like size, position of the antenna, feasibility, reflection coefficient, Specific absorption Rate (SAR), make it more difficult to design a multiband antenna. Current trend suggests that one device (Mobile, Tablet PCs etc.) should cover multiple communication applications (Like GSM, LTE, Bluetooth, Wifi etc.). It implies that antenna design should not only satisfy the constraints but also cover wide multiband range. In this research work, design, analysis and measurement of fractal antennas, are carried out, for such multiband applications. Revised cantor geometry is proposed for antenna design, which produces more than 5 resonances in second iteration only (feasible design). The three dimensional Finite Difference Time Domain (3D-FDTD) Method is used for analyzing the reflection coefficient of the antenna. Revised cantor geometry based compact, low profile LTE fractal antenna is proposed here, for Mobile and Tablet PC applications. The proposed antenna is appropriately covering several wireless applications, including LTE 1.7-1.8 GHz band, 2.3 GHz, 2.6 GHz and 2.9 GHz applications, WLAN 2.4 GHz and 5.8 GHz applications, GSM, UMTS, DCS, ZigBee, PCS, applications. This antenna is designed and analyzed using MATLAB code based on 3D FDTD method. Antenna finger dimensions are optimized using observations in MATLAB and CST Studio Suite. Radiation Patterns show, for all the observed frequencies, Directivity between 7.72 dBi to 8.17 dBi and Radiation Efficiency, within the range of -0.98 dB to -1.95 dB. Experimental reflection coefficient results present accurate matching with theoretical results. Theoretically analyzed SAR is less than 1.6 W/kg for 10 g tissue, without mobile circuitry. SAR reduction technique is also been presented.

In addition to this, fractal antenna on substrate with high dielectric constant, fractal antenna array design and integrated antenna designs, are also studied, as part of this work.

Contents

List of Figures

List of Principal Symbols and Acronyms

Acronyms

FDTD	Finite Difference Time Domain
FIT	Finite Integration Technique
MoM	Method of Moments
FEM	Finite Element Method
CST	Computer Simulation Technology
UWB	Ultra Wideband
WLAN	Wireless Local Area Network
LTE	Long Term Evolution: 4G
GSM	Global System for Mobile Communication
UMTS	Universal Mobile Telecommunications System
SAR	Specific Absorption Rate
PCS	Personal Communication Service

Principal Symbols

Symbol	**Name**	**Unit**	**Abbreviation**
ρ_l	Line Charge Density	Coulombs per meter	C/m
ρ_s	Surface Charge Density	Coulombs per square meter	S/m^2
ρ_v	Volume Charge Density	Coulombs per cubic meter	C/m^3
σ	Conductivity	Siemens per meter	S/m
J	Current density	Ampere per cubic meter	A/m^3
ϵ	Permittivity	Farads per meter	F/m
μ	Permeability	Henry per meter	H/m
E	Electric Field Strength	Volts per meter	V/m
D	Electric Field Displacement	Coulombs per square meter	C/m^2
H	Magnetic Field Strength	Amperes per meter	A/m
B	Magnetic Flux Density	Volt-seconds per square-meter	$V\text{-}s/m^2$
∇	Differential Operator	-	-

Chapter 1

Introduction

In this chapter, flow of the thesis is summarized. Antenna design is not a new topic but multiband antenna design for Mobile and Tablet PCs, is indeed, a new and challenging topic of research today. Motivation behind this research work is, this challenging task only. Increasing number of communication standards has leaded the antenna researchers to optimize the antenna designs for multiband applications. Nowadays several communication equipments are available in the market but very few are providing services in all communication standards. The main reason is that, for multiple communication applications, device needs to operate at multiple resonating frequencies. Therefore antenna designs which can provide multiband application capability with good radiation efficiency and less SAR are much needed. So as an antenna design is proposed in this work, is a better solution in this environment. The design approach and complete processes are explained in individual chapters according the objective and the flow. Every chapter in this work is connected to other chapters. This brief introduction will make those connections explicit, to the readers. It all starts from Electromagnetics waves and their behavior [1], but not everything could be included here in this thesis. Only specific concepts related to this work are incorporated in this thesis but readers are encouraged to go through references as and when required for detailed theories or backgrounds of the work.

1.1 Chapter 2

In chapter 2, the fundamental concepts and design guidelines for Microstrip Antenna are given. Objective of this research work revolves around multiband antenna design. So as fractal antenna concept is utilized. Fractal antenna designs are capable of producing multiple resonances. There are several fractal geometries on the earth. Only Sierpinski Gasket and Cantor Geometries are elaborated here in this chapter. These two are used mostly for antenna design. Cantor based geometry is simpler to design and fabricate, due to rectangular geometry. Revised cantor geometry is explained towards the end. This revised cantor based antenna design is the key for further antenna designing in this work.

1.2 Chapter 3

Main design and analysis portion starts in this chapter. The revised cantor geometry, which is explained in Chapter 2 is utilized here for antenna design. The main objective of this chapter is to show capability of revised cantor geometry in producing multiple resonances with less complex and easy to fabricate antenna design. The FDTD and FIT techniques are utilized to analyze the antenna designs. Observations show that FDTD based MATLAB code is a good alternative to validate the antenna performance parameters. A comparative analysis is presented between, results produced by FDTD and FIT.

1.3 Chapter 4

This chapter is the product of this work. A revised cantor geometry based fractal antenna design is proposed in this chapter, which is suitable for most of the communication standards, used in today's world. Initially design aspects of this antenna are discussed. Revised cantor antenna design begins with Microstrip feed,

and ground plane size. Substrate size is chosen approximately equal to the standard size, used in mobiles for back PCB. An algorithm is presented for revised cantor based antenna design. Observations on effects of modification in finger heights are provided in second sub section. On the basis of observations from initial sections, complete antenna design is created in the final part of initial section. Afterwards, Simulated and measured results are compared in next three sections. Now the main performance parameters of Mobile/Tablet antenna, SAR and Radiation Pattern are analyzed in the end. For SAR analysis a prototype is constructed for Mobile/Tablet.

1.4 Chapter 5

This chapter is containing research work, which is done during the current research work and maybe extended further. In the first section, an important enhancement is shown for multiband antenna design. Fractal antenna, itself yields multiband characteristics, and if substrates with high dielectric constant are added in the design, then antenna resonances are increased drastically. In the next section, fractal antenna array design is explained, which is an extension of the current research work. In the final section, study of integrated antenna design is presented which is an important and challenging topic nowadays. Antenna designs with RF signal processing circuits is always beneficial. Instead of designing two different RF components (antenna, filter etc.), researchers have started building antennas which can incorporate passive and active circuit components (or their characteristics), like Capacitors, Diodes, etc., along it.

Appendices A elaborates the fundamental concepts related to Antenna Design and Numerical Modeling in Electromagnetics B. Maxwell's equations are well defined and the most important tool in any electromagnetic design. So as Maxwell's equations are explained in this appendix. To understand Maxwell's equations, one need to understand some other fundamental concepts also, those are explained in the initial part of the appendix. Appendix B is utilized to explain the numerical modeling

in electromagnetics. Before designing any antenna in any commercially or freely available simulation tool, one needs to understand the concept of numerical techniques, working in the background of the tool. Taking this into account, two mostly used, numerical techniques in electromagnetics are presented with their mathematical explanation. The Finite Difference Time Domain Method, FDTD and the Finite Integration Technique, FIT are the two. In this work FDTD based MATLAB code is written and utilized for antenna design and analysis. Results obtained in MATLAB are consistently validated with CST Studio Suite, a commercially available tool. CST works on FIT majorly. To begin, fundamentals of electromagnetics are provided in first section. All the concepts, required to understand mathematical definitions in FIT and FDTD, are provided in this initial section. FDTD implementation related parameters are explained in Chapter 3 and 4. But, to properly implement those parameters, content of this chapter is a must, to be understood, prior to implementation.

Chapter 2

Fractal Microstrip Antenna

Microstrip Antenna is a technology, which changed the path of antenna design, dramatically. It has attributes of low profile, low cost and lower fabrication time. These attributes are leading this innovation current scenario. Initially single or dual microstrip antenna design for sufficient, but nowadays communication standards have increased which makes a necessity for multiband antenna design. This is where; fractal antenna design comes in the picture.

2.1 Microstrip Antenna

A Microstrip antenna is basically a conductor printed on top of a layer of substrate with A backing ground plane as shown in figure 4.2. The length of the radiating conductor or patch is made approximately $\frac{\lambda_g}{2}$, so the patch starts to radiate. In chapter 5, in all the designs of the Microstrip antenna, the patch will be fed by a Microstrip transmission line, which usually has a 50Ω impedance. The antenna is usually fed at the radiating edge along the width W as it gives good polarization, however the disadvantages are the spurious radiation and the need for impedance matching [2]. This is because the typical edge resistance of a Microstrip antenna ranges from 150Ω to 300Ω [3].

The design of a Microstrip antenna begins by determining the substrate used for the

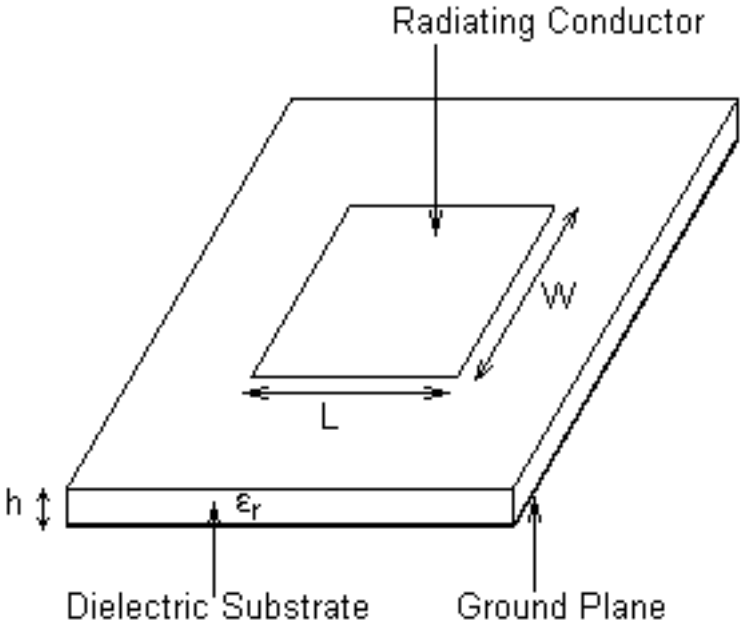

Figure 2.1: Microstrip Antenna

antenna and then the dimensions of the patch. Due to the fringing fields along the radiating edges of the antenna there is a line extension associated with the patch, which is given by the formula [4]:

$$\frac{\Delta L}{h} = 0.412 \left[\frac{\epsilon_{eff} + 0.3}{\epsilon_{eff} - 0.258}\right] \left[\frac{\frac{W}{h} + 0.264}{\frac{W}{h} + 0.813}\right] \tag{2.1}$$

The effective dielectric constant ϵ_{eff} due to the air dielectric boundary is given by [4]:

$$\epsilon_{eff} = \frac{\epsilon_r + 1}{2} + \frac{\epsilon_r - 1}{2} \left[1 + \frac{10h}{W}\right]^{\frac{1}{2}} \tag{2.2}$$

The resonant frequency can be estimated by using the formula [3]:

$$f_r = \frac{1}{2\sqrt{\mu_0 \epsilon_0}\,(L + 2\Delta L)\,\sqrt{\epsilon_{eff}}} \tag{2.3}$$

Here,

ϵ_{eff} = Relative dielectric constant

ϵ_0 = Permittivity of free space

μ_0 = Permeability of free space

ΔL = Line extension

By choosing the substrate, the width and length of the patch can be estimated. An initial approximation for the length can be made for a half wave Microstrip antenna radiated by the formula:

$$L = 0.48\lambda_g \tag{2.4}$$

Where,

$$\lambda_g = \frac{c}{f_r\sqrt{\epsilon_r}} \tag{2.5}$$

The width (W) is usually chosen such that it lies in the ratio, L < W > 2L for good radiation characteristics, if W is too large then higher order modes will move closer to the design frequency.

2.2 Fractal Antenna

French mathematician B.B. Mandelbrot, during 1970s, presented a theory of fractals [8, 9]. This was the beginning for antenna researchers to start thinking about it. His research was, on several naturally occurring irregular and fragmented geometries [8]. The word "Fractal" is derived from, Latin word, "fractus" (fangere as a verb) which means "To break". Some fractal geometries are shown in Figure 2.2. There

Figure 2.2: Fractal Geometries in Nature

are many fractal geometries like, Sierpinski Gasket, Carpet, Koch Curves, and Cantor fractal geometries etc. that are used for planar antenna design [7]-[32]. Most surveyed and explained geometry, in literature, is Sierpinski gasket geometry. So as initially Sierpinski geometry is studied. This geometry is a bit complex geometry and has limitations on producing large number of resonating bands. This provided motivation to work on cantor fractal geometry, which is simpler in comparison to all other fractal geometries, and provides more number of resonating bands over a wide range of frequencies.

2.2.1 Sierpinski Gasket antenna

This is one of the most explored and utilized geometry for multiband antenna design due to its small size [10]-[16]. This geometry is generally designed with decomposition of equilateral triangles by using mathematical transformations as shown in Figure 2.3 [10]. This geometry can be used for antenna design in three differ-

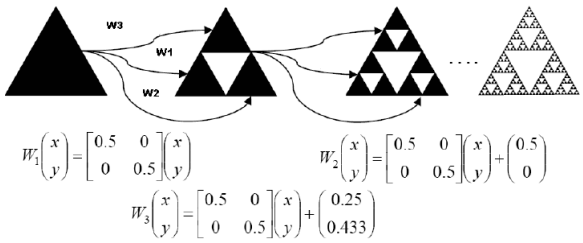

Figure 2.3: Sierpinski Gasket Geometry: Decomposition Approach

ent forms as Monopole, Dipole and Microstrip patch antenna as shown in Figure 2.4 [10, 11, 12]. The self-similar current distribution on these antennas causes its multi-band characteristics [13]. By perturbing the geometry the multi-band nature of these antennas can be controlled [14]. Variation of the flare angle of these geometries changes the band characteristics of the antenna [16]. The lower resonant frequencies of the antennas remain unperturbed by the increase in the iteration order in Decomposition approach. The lowest resonance corresponds to the largest

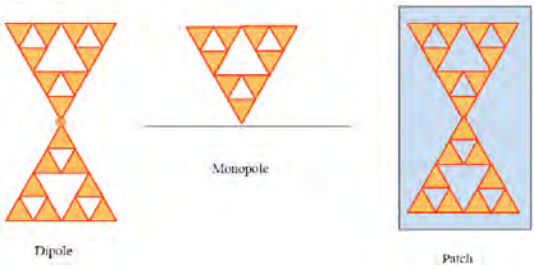

Figure 2.4: Sierpinski Gasket Antenna

triangle, which remain the same in all cases. A characteristic shift in resonance occurs, towards the lower side, as the angle is increased [13, 14]. Changing the Sierpinski gasket geometry by increasing fractal iteration does not alter the antenna characteristics significantly, especially at the lower resonant frequencies but at high frequencies, shifts in resonances are significant.

2.2.2 Cantor and Revised Cantor Geometries

Cantor based geometry is used for this research work for designing multiband antennas. Major reason for choosing this geometry is its simpler iterations in comparison to other geometries. It has rectangular strip structure. Cantor and Revised Cantor Geometries are iterative geometries. Iteration functions are also very simple, to calculate the iterative geometry points. An initiator is used as base of the structure. Initiator is then divided into segments according to Iteration Function System [42, 7, 29]. The process is repeated to obtain next iterations.

Cantor Geometry

An initiator of height H and width W is used to form a self similar object known as Cantor Set. Partitioning of the initiator (K0) provides three non overlapping segments with the removed middle segment. This procedure is repeatedly used for generation of consecutive iterations. Cantor fractal iterations are shown in Figure 2.5.

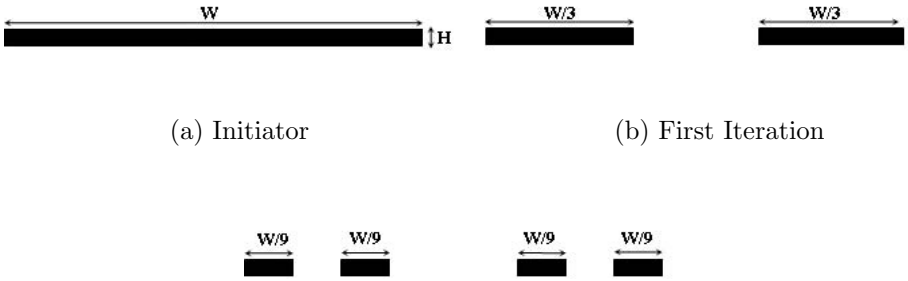

(a) Initiator

(b) First Iteration

(c) Second Iteration

Figure 2.5: Cantor Fractal Geometry

Iteration Function System (IFS), represented by self affine transformation, is used to describe it [42, 29]. The transformation of initiator into iterative layer is represented in matrix form as:

$$\begin{bmatrix} \overline{x} \\ \overline{y} \end{bmatrix} = w_i \begin{bmatrix} x \\ y \end{bmatrix} = \underbrace{\begin{bmatrix} a_i & b_i \\ c_i & d_i \end{bmatrix}}_{T} \begin{bmatrix} x \\ y \end{bmatrix} + \begin{bmatrix} e_i \\ f_i \end{bmatrix} \tag{2.6}$$

Here, $(\overline{x}, \overline{y})$ represents the coordinates of the transformed layer. (x, y) represents the coordinates of initiator (K0). a_i, b_i, c_i, d_i, e_i and f_i are the transformation coefficients. T is the transformation matrix. The IFS coefficients for Cantor set geometry are presented in Table 2.1.

Table 2.1: IFS TRANSFORMATION COEFFICIENTS FOR CANTOR SET GEOMETRY

w_i	a_i	b_i	c_i	d_i	e_i	f_i
1	0.3	0	0	1	0	0
2	0.3	0	0	1	0.6	0

The generation of Cantor set geometry on the basis of IFS, given in Table 2.1, is shown above. All the segments are of the same dimensions, generated in the

same iteration. A fractal antenna based on Cantor fractal technique has multiband characteristics due to self similar shape [42, 29].

Revised Cantor Geometry

Revised Cantor geometry is proposed in this work and is published, in [24]. Initially the initiator (K0) of height H and width W is transformed into the first layer of iteration. First layer represents initiator subdivided in three segments. Height and width of starting segment are H and $\frac{W}{4}$ respectively. Middle segment is removed. Last segment is of height H and width $\frac{W}{2}$. This process is then repeatedly applied on the initiator to obtain consecutive layers of the iterations. Cantor fractal iterations are shown in Figure 2.6. This geometry is represented by new IFS coefficients. IFS coefficients for this geometry are given in Table 2.2.

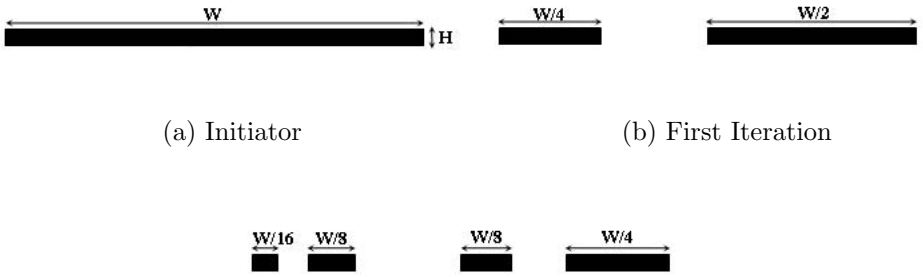

(a) Initiator

(b) First Iteration

(c) Second Iteration

Figure 2.6: Revised Cantor Fractal Geometry along W

Table 2.2: IFS TRANSFORMATION COEFFICIENTS FOR REVISED CANTOR SET GEOMETRY

w_i	a_i	b_i	c_i	d_i	e_i	f_i
1	0.25	0	0	1	0	0
2	0.5	0	0	1	0.5	0

Previous revision is done along the Width, W. Next revision is done with respect to height, H. First the initiator (K0 : Height of H, Width of W) is used as the base of the geometry. The initiator is then subdivided into three segments with the middle segment removed. Starting segment has height H and width $\frac{W}{4}$ while the last segment has height of 2H and length of $\frac{W}{2}$. The process is then repeated to obtain consecutive layers of iterations. Multifractal Revised Cantor iterations are shown in Figure 2.7.

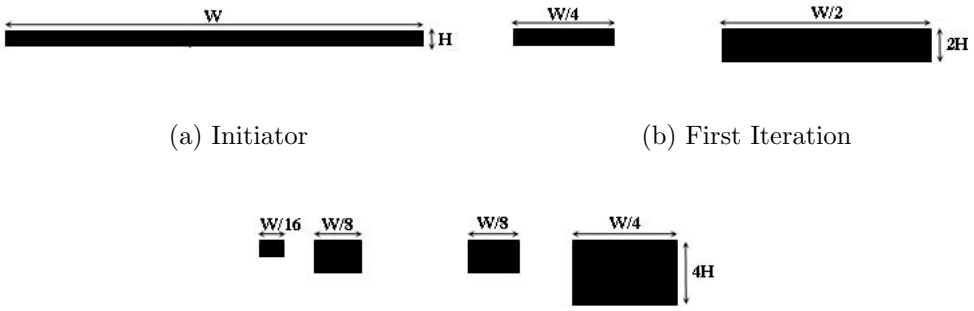

(a) Initiator

(b) First Iteration

(c) Second Iteration

Figure 2.7: Revised Cantor Fractal Geometry along W and L, both

Transformation is modified to represent this geometry. The transformation of initiator into iterative layer is represented in matrix form as:

$$\begin{bmatrix} \overline{x} \\ \overline{y} \end{bmatrix} = w_i \begin{bmatrix} x \\ y \end{bmatrix} = \underbrace{\begin{bmatrix} a_i & b_i \\ c_i & m_i * d_i \end{bmatrix}}_{T1} \begin{bmatrix} x \\ y \end{bmatrix} + \begin{bmatrix} e_i \\ f_i \end{bmatrix} \tag{2.7}$$

Here, $(\overline{x}, \overline{y})$ represents the coordinates of the transformed layer. (x, y) represents the coordinates of initiator (K0). a_i, b_i, c_i, d_i, e_i and f_i are the transformation coefficients. m_i is the modification factor. T1 is the transformation matrix. Modified IFS coefficients for this transformation are given in Table 2.3.

Table 2.3: NEW IFS TRANSFORMATION COEFFICIENTS FOR MULTIFRACTAL REVISED CANTOR SET GEOMETRY

w_i	a_i	b_i	c_i	d_i	e_i	f_i	m_i
1	0.25	0	0	1	0	0	1
2	0.5	0	0	1	0.5	0	2

Revised Cantor Geometry Based Antenna Design

The antenna iterations are constructed by putting consecutive multifractal iterative geometries on the base iteration. The fractal revised cantor iterations, used for antenna structure, are shown in Figure 2.8. Revised Cantor Geometry based antenna design is elaborated in Chapter 3

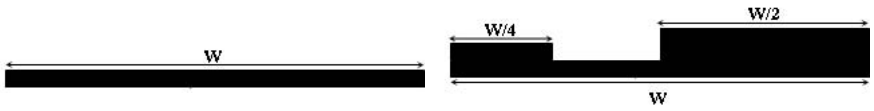

(a) Initiator (b) First Iteration

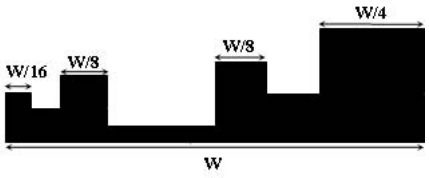

(c) Second Iteration

Figure 2.8: Multifractal Revised Cantor iterations for Antenna

2.3 Conclusion of the Chapter

Main goal of this work is to design antennas for multiband applications, so as Fractal geometries are explained. In accordance to that, antenna size and complexity are

an also major issue, which is why Microstrip antenna design is also explained in this chapter. These two concepts are utilized throughout this research work.

Chapter 3

Revised Cantor Geometry based Antenna

Revised cantor geometry and basic antenna design concept are presented in Section 2.2.2. In this chapter, this fractal geometry is utilized for antenna design. FDTD based MATLAB code and FIT based CST Studio Suite tool, are used for analysis of the antenna design. Return loss is determined and compared for both the techniques. FDTD and FIT techniques are elaborated in Sections B.1 and B.2.

3.1 Antenna Design

A fractal Microstrip antenna is developed on Teflon (Polyterafluoro-ethylene) substrate with ϵ_r of 2.2. The conducting radiating revised cantor geometry based structure is mounted on the substrate. This substrate has ground plane on its bottom. The ground plane has dimensions of 38.5 $\times$ 32 mm. Further research work on Ground Plane and Microstrip Feed is explained in Section 4.1.2. An initiator of 36 $\times$ 2.1 mm is used to form the complete geometry. The size of initiator is chosen on the basis of standard Microstrip line structure which has width of about 1.8 mm, in general [2, 4]. The proposed fractal antenna, in [24, 25], is derived structure of the second iteration of the cantor based antenna proposed by B. Manimegalai et

al. [7]. The revised cantor based fractal antennas, in [24, 25] produce more than 5 resonances in their second iteration itself, while, cantor based antenna, needs at least third iteration, for generating more than 4 resonances [7]. A Microstrip feed line is used for exciting the antenna. Microstrip feed is 1.8 mm thick. The proposed fractal structure is developed after a gap of 2.4 mm from the ground plane dimensions vertically. The total height of the antenna is 59.6 mm. All the dimensions are shown in the Fig. 3.1. The overall antenna structure is shown in Fig. 3.2.

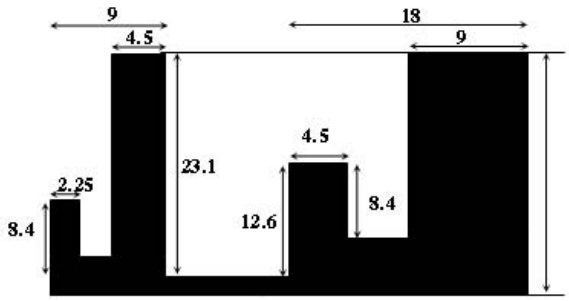

Figure 3.1: Multifractal Structure

3.2 Analysis using FDTD

The Return Loss is an important parameter in the designing and development of an antenna. Return loss shows the resonances of an antenna where the power is maximally transmitted or received. So it is necessary to analyze the reflection coefficient with fewer amounts of error and efficient approximation. This purpose is achieved by using numerical methods for modeling and simulation of an antenna. There are several numerical methods available nowadays. In most of the cases an antenna is modeled and simulated using one numerical method only. But the final reflection coefficient of the antenna is validated when it is fabricated and tested practically. Sometimes the reflection coefficient produced by simulation does not meet the reflection coefficient practically measured. Now the antenna cannot be fabricated again and again to fulfill the requirements. So, one solution for this problem is proposed

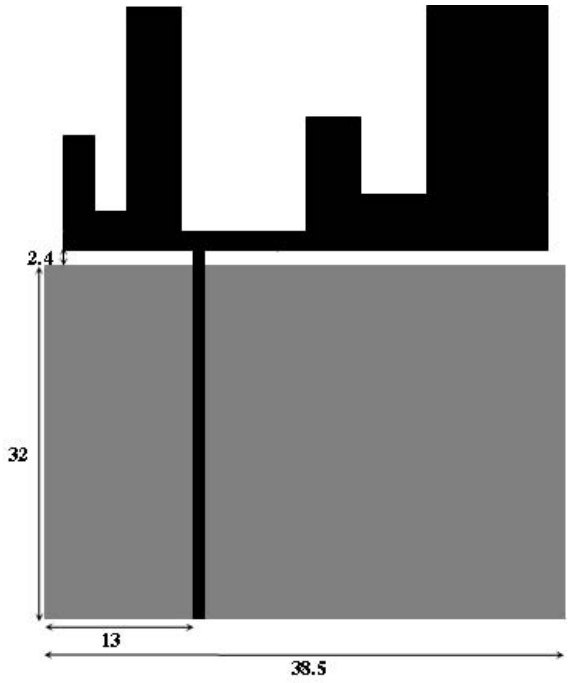

Figure 3.2: Antenna Structure

here. To validate the reflection coefficient produced by one numerical method, another numerical method can be used. This provides less probability of mismatch between the simulated and measured results. Thus to accomplish the task, two numerical methods namely the Finite Integration Technique (FIT) and the Finite Difference Time Domain (FDTD) method are used.

An antenna design, similar to the antenna shown in Figure 3.2 in previous section, is developed with different dimensions as shown in Figure 3.3. This antenna design is considering same dimensions for Substrate and Ground plane. Microstrip feed dimensions and position, along the width of substrate, is also same. A MATLAB Code based on 3D-FDTD approach is written and utilized for the design and the analysis [34, 35, 43]. Time step Δt of 3.3356 ps is used according to the Courant-Friedrichs-Lewy (CFL) condition. Grid cell of 0.262 mm $\times$ 0.4 mm $\times$ 0.4 mm is used. Antenna is excited by a gap signal source specified with a 50 Ω series source impedance to simulate a real signal generator, and to reduce the number of time

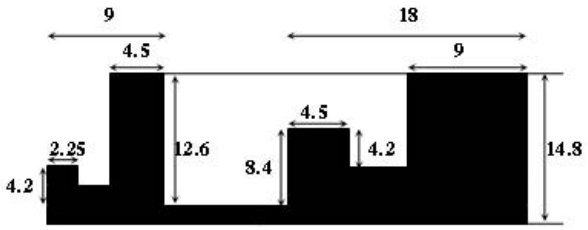

Figure 3.3: Multifractal Structure

steps, needed for convergence, as shown in Figure 3.4. Transient excitation for 7000 time steps, using a Gaussian derivative pulse, is utilized to calculate the wideband results. The simulated reflection coefficient in MATLAB is shown in Fig. 3.5.

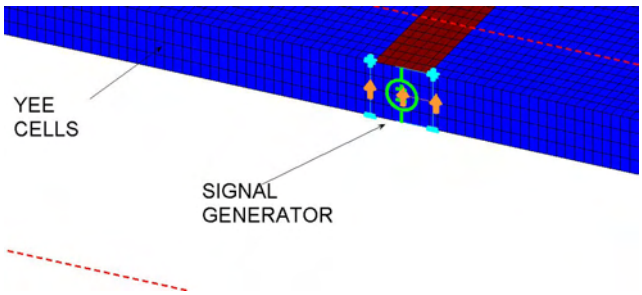

(a) Grid Cells

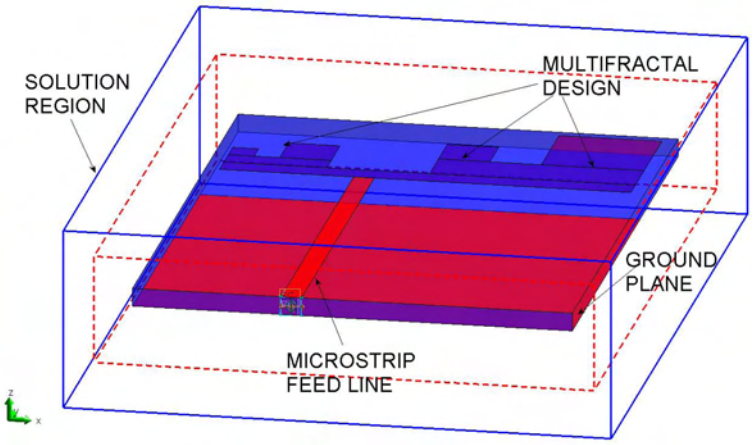

(b) Antenna Structure in MATLAB

Figure 3.4: Explicit View of Antenna in MATLAB

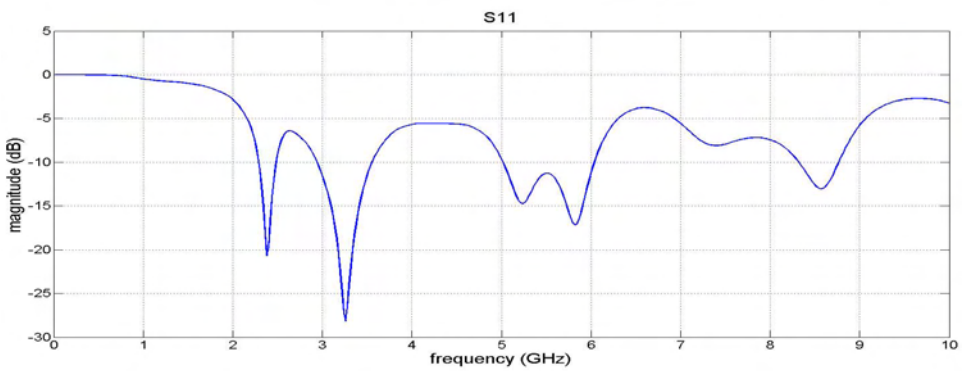

Figure 3.5: Reflection Coefficient in MATLAB

3.3 Return Loss Validation using FIT

A commercially available simulator known as Computer Simulation Technology (CST) Microwave Studio is used for the simulation. CST is basically working on FIT B.1. CST gives a windows graphical environment to simulate any antenna. Initially the antenna structure is modeled in CST then using hexahedral approach simulation is performed. The modeled antenna structure is shown in Figure 3.6.

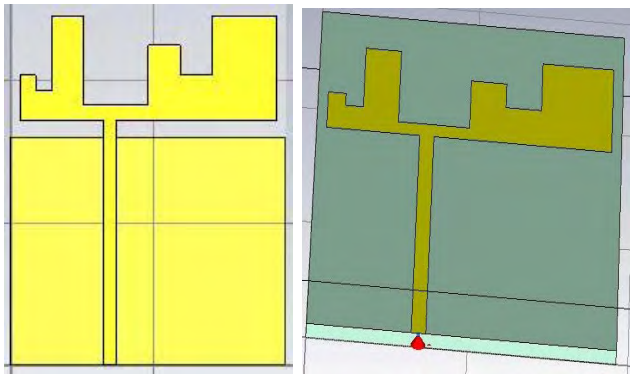

(a) Normal View (b) Perspective View

Figure 3.6: Antenna Structure by FIT

During FDTD analysis, Yee's meshing scheme is utilized, which is basically hexahedral cell type meshing scheme. To maintain similarity for comparison, hexahedral

Frequencies in GHz	S_{11}**(dB):FDTD**	S_{11}**(dB):FIT**
2.4	-20.69	-20.71
3.3	-28.15	-43.53
5.2	-14.73	-22.20
5.8	-17.06	-36.85
8.5	-13.03	-25.10

Table 3.1: Comparison of resonance Points on S_{11} Plot after FDTD and FIT Simulations; here frequencies are approximated

meshing is utilized in CST Studio also. Simulated reflection coefficient is shown in Figure 3.7. As it is quite explicit that both FDTD and FIT based analysis pro-

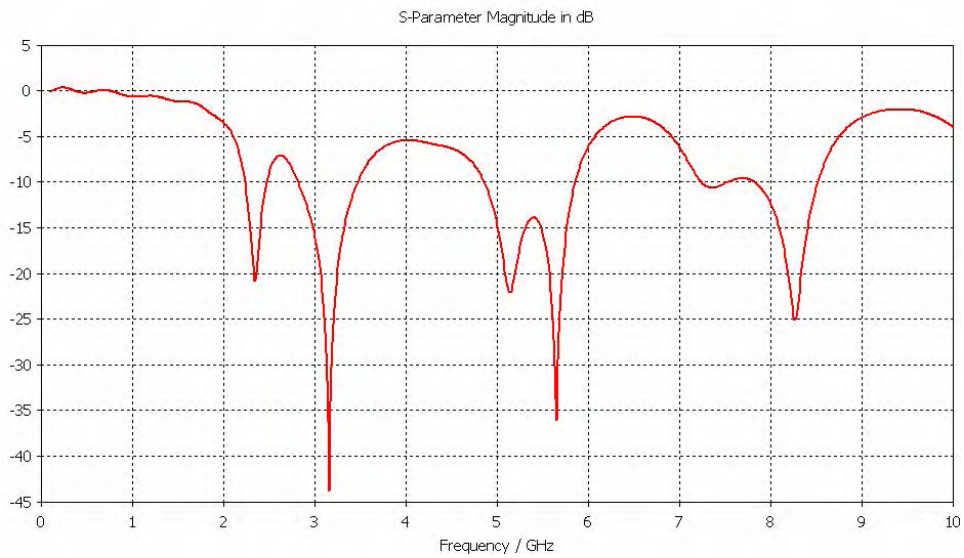

Figure 3.7: Reflection Coefficient in CST

duces similar results. It validates the reflection coefficient of the developed antenna. Comparison of the result with respect to the corresponding resonating frequencies is shown in Table 3.1

3.4 Conclusion of the Chapter

Revised cantor geometry is proposed due to the fact that it produces more number of resonances for its second iteration only. Objective of this work is not only, design-

ing a multiband antenna, but also, reduction in size and complexity. So as Revised cantor geometry provides a better choice because second iteration is less complex and lower is the size, in comparison to the third iteration of the cantor geometry based antenna design. This work is published in [25]. FDTD based code is also written in MATLAB. Reflection coefficient of revised cantor geometry based antenna, generated by this code, and is compared with a commercially available tool, CST Studio Suite, which works on the principle of FIT. This work in published in [33].

Chapter 4

Mobile/Tablet Antenna Design and Analysis

Antenna design for Mobile Application is an important research topic nowadays. Main reason for this being difficult but attractive is the increased number of required resonating bands and their combined effects on humans. The antenna design, presented in this chapter, is mainly focused for Smart Phones and Tablet PCs. Nowadays, single mobile or tablet needs to work on all the required communication bands. These bands are mainly LTE, GSM and WLAN. There are several mobile phones and tablets, which use multiple antennas to achieve this. When multiple antennas are put on a single phone, they have interferences and several other problems, like increased size, increased SAR, data lost conditions etc. So as researchers are now moving towards single antenna solutions, which can work on all the required bands [45]-[49]. There is literature, where a lot of research has been carried out towards these objectives. There are many fractal geometries which have been used for antenna designing as explained in Chapter 2. Self affinity has provided these geometries popularity in antenna design 2.2. In this work, revised cantor based geometry is used for proposed antenna design, which is detailed in Section 2.2.2. The main reason, behind choosing this geometry is that, it is simple to be fabricated and

resonates on many bands according to finger length variations.

Design and analysis is done using Finite difference Time Domain (FDTD) method 3.2. 3D FDTD based code is written in MATLAB. As a part of this work is presented in [33]. In the work done by Dhoot et al., the code is compared with a commercially available tool CST Studio suite [33]. In this work of [33], FDTD code is not compared with any measured result. In this chapter, comparison of this code is also presented, with measured reflection coefficient. FDTD method is the most appreciated numerical method in computational electromagnetics, worldwide. It's versatile and broad range of applications, make it more suitable in electromagnetics [34, 35, 43]. Effect of ground plane cannot be neglected. In [50]-[55], slotting and shortening of ground plane is analyzed. In the work of Chen et al., ground plane has been cut such that it increases the bandwidth of the mobile phone antenna [51]. This concept is utilized in this work too. Ground plane affects the shift in resonances. Length of Microstrip Feed is 2.4 mm lengthier, in comparison to Ground plane. This concept is used to make a resonance at 2.3 GHz, which is at center of the entire LTE band of Mobile communication, 1.7 GHz to 2.9 GHz. Specific Absorption Rate (SAR) calculations for a mobile phone or tablet is a prerequisite for telecommunication industry [56]-[61]. So as SAR calculations have been carried out in this work. These calculations are done with the help of a commercially available tool, CST Studio Suite [63]. In [64, 67], FDTD based SAR analysis is proposed to design handset for reduced absorption in human head and hand. In [65, 66], effects of distance of mobile from head is presented, which are considered in this work. In [44, 45, 46], SAR effect is elaborated, when mobile circuitry is involved and not involved. In this work, mobile circuitry is not been involved, so as SAR values are moderate. If mobile circuitry is included then SAR will be reduced lesser. Ground plane also affects the SAR. This is studied in [68], which is utilized in shortening ground, in this work. In [47, 48, 49], LTE antennas are proposed but they are of larger size and covering smaller bands. Antenna design, proposed in this work is compact, easy to fabricate (substrate is FR4, which is easily available), low cost and

low profile.

4.1 Design of the Proposed Antenna

There antenna design based on revised cantor geometry is explained in previous Chapter 3. This design is used for developing a multiband antenna for Mobile and Tablet PCs.

4.1.1 Ground Plane and Microstrip Feed

An algorithm is proposed as an extension to the work carried out in [24, 25]. This algorithm suggests relative design of feed and ground plane. Ground plane dimensions affect the resonances significantly [51, 54, 44]. The ground plane has been shortened for resonances in the required frequency range. A feed line is created (1.8 mm×34.4 mm), using Microstrip feed, for the antenna. Feed effects on the resonance are shown in [13]. Feed strip generates a resonance around 2.3 GHz, which is the center frequency of our required range. Algorithm is as follows:

1. Calculate $f_{calculated} = f_{required}$-35 MHz.

   Here, $f_{calculated}$ and $f_{required}$, are in GHz.

2. Calculate $\lambda = \frac{c}{f_calculated}$

3. Define h = $\frac{\lambda}{4}$.

4. Define Ground Height $\tilde{=}$ h

5. Define Feed Length $\tilde{=}$ h+1.4 mm.

This algorithm is based on the observations on feed length and ground size variations of the revised cantor geometry presented in [24, 25]. Several observations for different frequencies have been taken. One of the parametric observation graphs is shown in 4.1. For different subtracted frequencies also, different variations have been observed

to conclude on the added value of 1.4 in h. Modifying the finger lengths affects

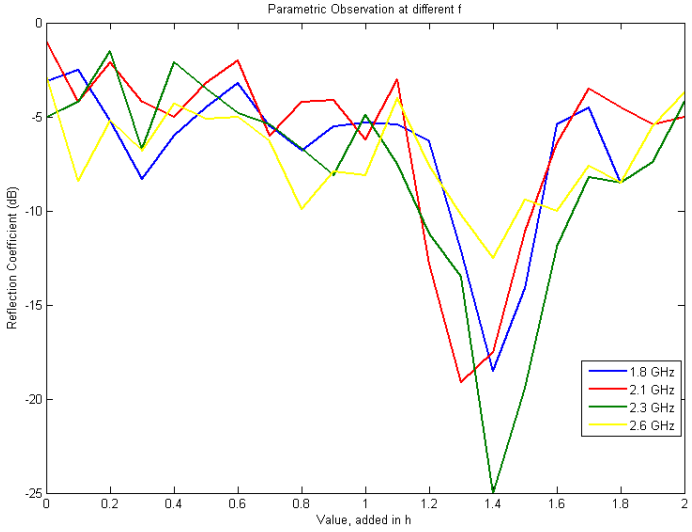

Figure 4.1: Parametric Observation

the resonances again, which needs to be tuned back. For initiating the geometry, design at center resonating frequency, is a better approach. Feed and ground plane, together, create a quarter wave monopole Microstrip antenna resonating at $f_{required}$. This algorithm is an approximation for only revised cantor geometry.

4.1.2 Modification of Finger Heights

Modifications in the fingers' lengths are used for optimizing the antenna resonances in the second iteration of the proposed fractal antenna and reconstructing the fractal antenna for multiband applications [24]. Fingers, flat rectangles, of antenna give an opportunity to tune the resonances easily. Several observations have been taken on finger lengths, in this work, to design the required antenna. The antenna structure is constructed on a substrate FR4 with ϵ_r=4.4. FR4 is a generally accepted low cost substrate material, which is used for antenna printed circuit board. This substrate is easily available in the market. The dimensions of substrate are 38.5

mm×(max(h1,h2,h3,h4)+iteration length+34.4) mm. Here, iteration length is the length of iterative geometry up to just bottom of the corresponding finger. For example, if h1 is maximum then h1+2.1+2.1+34.4 mm is the height of the substrate with iterative length of 4.2 (height of base+height of left partition of first iteration). The ground plane (38.5 mm×32.0 mm) is placed below the substrate. The conductor fractal geometry is placed just above the substrate. Microstrip line (1.8 mm×34.4 mm) is used for the feed of antenna. The base iteration is 36.0 mm×2.1 mm. Heights of the fingers are obtained from the fractal iterations. Other dimensions are derivable directly from the antenna structure shown in Figure 4.2. There

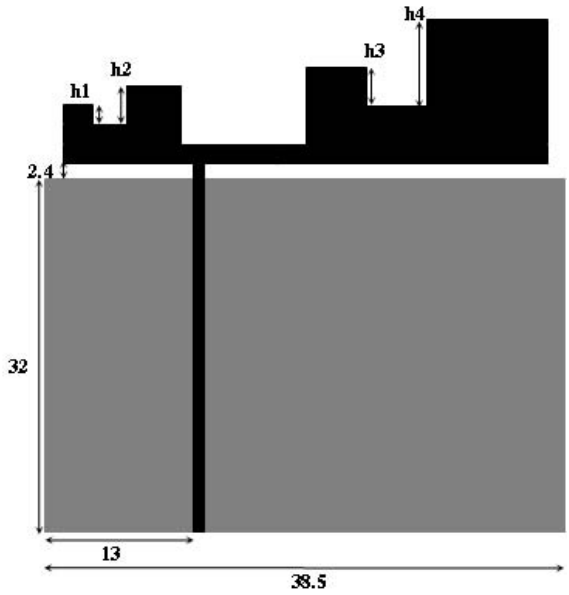

Figure 4.2: Second Iteration of Multifractal Antenna Structure: All Dimensions are in mm

are many parameters of antenna that affect the resonating frequencies or bands like the dimensions and relative dielectric constant of substrate, ground plane, fingers and many more. The fingers of fractal antenna have the major effect on the resonating bands. The effect of variation of the fingers is discussed in this work. Different fingers affect different or same frequency bands. Increase or decrease in the finger height affects the resonances. Four fingers are present in the structure proposed in

this work. Because it is only the second iteration, it has four fingers, but by analyzing higher order iterations, one can increase the number of fingers. The second iteration itself can be used to cover many frequency bands. Initially the effect of first finger (h1) on the reflection coefficient of the antenna is shown in Figure 4.3. As h1 is increased up to a height of 14.7 mm (7H), it increases the resonance in 2 GHz to 4.7 GHz band and decreases the resonance in 5.9 GHz to 6.8 GHz band. But as it is increased more up to 33.6 mm (16H), it decreases the resonances in both the bands. Thus h1 needs to be set around 7H to obtain good resonance in both the frequency bands. Now, the height of the second finger (h2) is varied and the

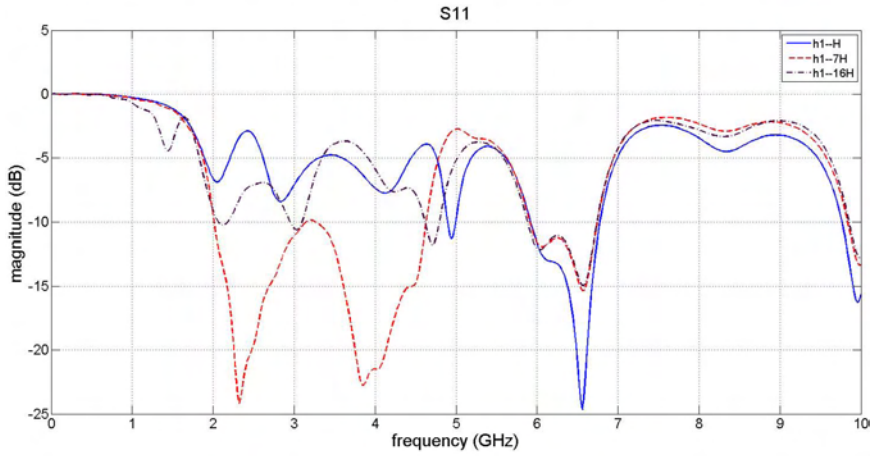

Figure 4.3: Return Loss variation with h1

simulated reflection coefficient is shown in Figure 4.4. As can be observed from the Figure that the increase in height of h2 up to 18.9 mm (9H) increases resonance in 2.0 GHz to 3.8 GHz band and does not affect the other resonances like in 5.9 GHz to 6.9 GHz band and 9.7 GHz to 10.0 GHz band. But the further increase in h2 up to 35.8 mm (17.05H) affects the lower band of 2.0 GHz to 3.8 GHz band. It reduces the resonance in significant manner. Still, the other two bands are not affected much with this further increase in the height of h2. These two phenomena have one observation in common that the increase in the difference between h1 and h2 (or mod(h1-h2)) should be around 6H-8H to maintain the resonance in 2.0 GHz to 4.5

GHz band. This is an important observation and is used in next section. Effect of

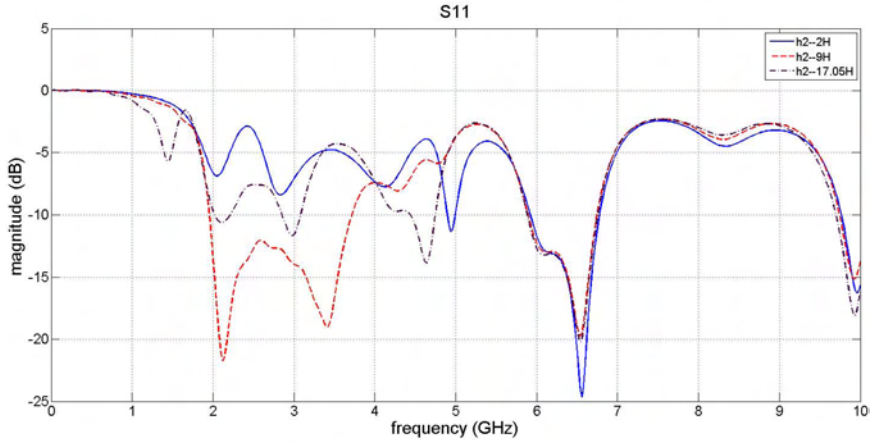

Figure 4.4: Return Loss variation with h2

the height of the third finger (h3) is shown in Figure 4.5. It exploits that increase in h3 up to 18.9 mm (9H) spreads the band near 6 GHz by around 200 MHz and shifts it towards left to 5.8 GHz. Other resonances are unaffected. Even after the further increase up to 33.6 mm (16H), no effect is observed on the bands except that there is one more resonance near the 1.8 GHz band. Similarly, the effect of the height of

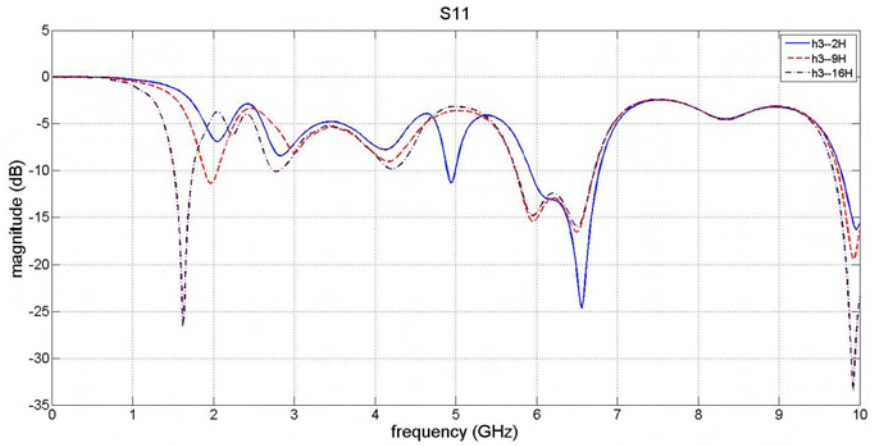

Figure 4.5: Return Loss variation with h3

fourth finger (h4) is shown in Figure 4.6. Similar to the effect of h3, increase in h4

up to 27.7 mm (13.2H) also spreads the band near 6 GHz. But it affects the lower band also at 1.8 GHz. Now, further increase up to 38.2 mm (18.2H) does not change the band near 6 GHz but provides two additional resonances at 1.5 GHz and 2.8 GHz. Again, one commonality is that the increase in the difference between h3 and h4 (or mod(h3-h4)) should be around 6H-8H to maintain the resonance in 5.8 GHz to 6.9 GHz band. This is also an important observation and is used in next section. Major conclusions on antenna fingers are shown in Table 4.1

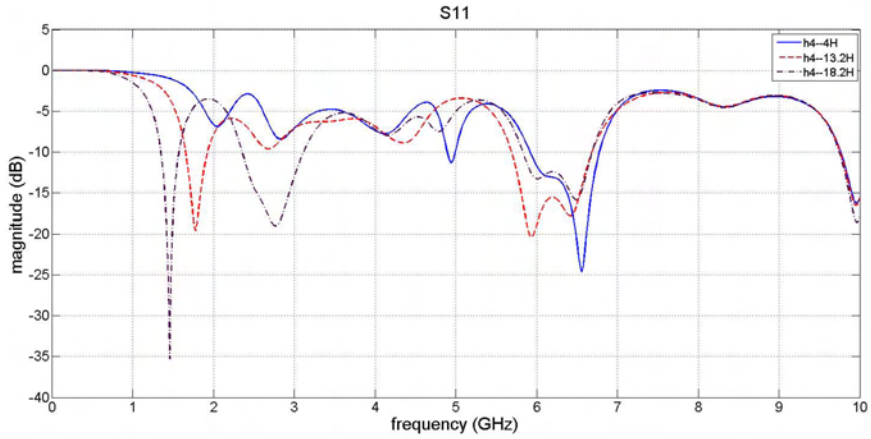

Figure 4.6: Return Loss variation with h4

Finger	Observational Conclusion on increasing height
h1	Improves S11 between 2.0-4.7 GHz, degrades S11 for 5.5-7.0 GHz
h2	Improves S11 between 1.5-3.8 GHz, doesnt affect other bands
h3	Improves S11 for 1.8 GHz band and broadens the 5.8 GHz band
h4	Improves S11 for 1.5-1.9 GHz band broadens the 5.8 GHz band

Table 4.1: Finger heights and their Observational Conclusions

4.1.3 Complete Antenna Design

LTE bands along with other bands is a challenging design [53, 54].On the basis of all the observations presented in the previous sections, resonances with respect to one frequency or at max two frequencies are optimized. For more optimization, CST is

utilized. Three different frequencies were used for optimization through CST, 1.8 GHz (GSM 1.7-1.9 GHz), 2.44 GHz (LTE 2.1-2.9 GHz, and Bluetooth) and 5.84 GHz (WLAN). These are center frequencies of the bands that are of importance. Accordingly, revised cantor geometry based fractal antenna design is proposed here, which is covering all resonating bands for mobile communication. Dimensions of the proposed antenna, are shown in Table 4.2. Antenna design is shown in Figure 4.7.

Sr. No.	Dimension	Value (mm)
1.	Substrate Thickness	1.6
2.	Substrate Length	60
3.	Substrate Width	38.5
4.	Base Width	2.1
5.	h1	8.4
6.	h2	21
7.	h3	8.4
8.	h4	18.9
9.	w1	2.25
10.	w2	4.5
11.	w3	4.5
12.	w4	9

Table 4.2: Dimensions of Proposed Antenna

4.2 FDTD Analysis

Finite difference time domain method based MATLAB code is written and used for the antenna design and analysis [34, 35, 43]. In the work presented by Dhoot et al., reflection coefficient validation is done in comparison with a commercially available tool CST Studio suite [33]. In this work comparison with measured results is shown in the next subsection. FDTD mesh element, Yee cell, size are decided according to antenna dimensions. Time step is decided using CFL condition. All parameters are shown in Table 4.3 Here, λ is calculated with respect to center frequency of the required band, i.e., in this work, 2.3 GHz. Cell dimensions are defined in such a manner, that simulation time is also less and results are also accurate. As can

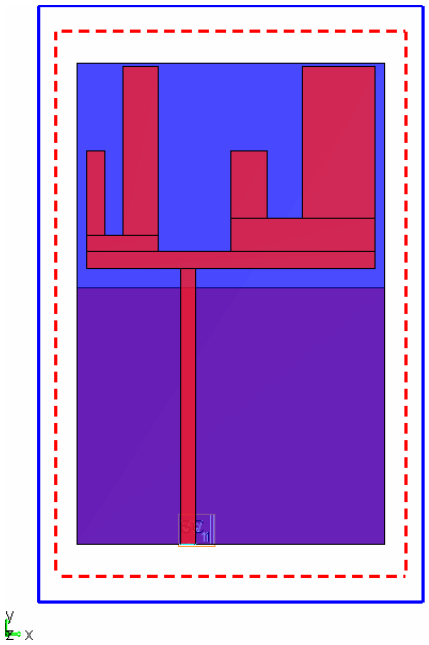

Figure 4.7: Multiband Antenna for Mobile and Tablet

Sr. No.	Parameter	Value
1.	Δx	$\frac{\lambda}{350}$
2.	Δy	$\frac{\lambda}{450}$
3.	Δz	$\frac{\lambda}{200}$
4.	Δt	2 ps

Table 4.3: FDTD implementation related parameters

be observed, proposed antenna has small expansion in Z-direction, so as broader mesh size is chosen. In X and Y directions, antenna geometry is defined. So as Finer mesh sizes are used along these directions. Time step is derived using CFL condition [34, 35]. Total time steps are considered as 6000. In previous work of authors [33], mesh size is not dependent on λ and manual values are used. This causes few problems, like random simulation time, random accuracy and sometimes meshes errors too. Authors would recommend that whenever mesh is chosen, it should be defined with respect to wavelength. It resolves these kinds of normal errors, which may affect the results, sometimes. If manual values are calculated with some appropriate calculations, these may work fine too. For larger geometries,

with curvilinear elements, manual/custom meshing may be required but for small geometries, like Microstrip antennas, it is generally not required.

4.3 Fabrication and Measurements

Antenna is fabricated using FR4 substrate. The fabricated antenna is attached to a SMA connector. Return loss is measured using Agilent's ENA. The fabricated antenna and measurement setup is shown in Figure 4.8.

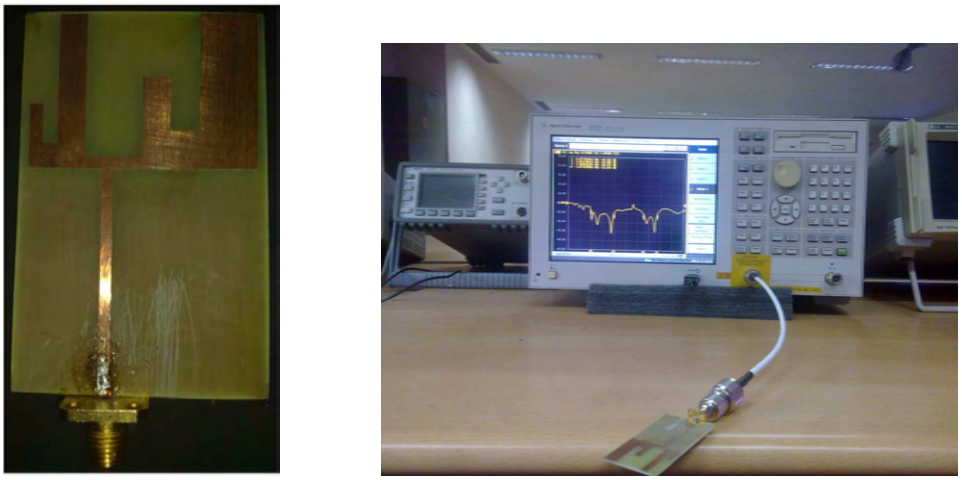

(a) Fabricated Antenna (b) Measurement on Agilent's ENA

Figure 4.8: Multiband Antenna

4.4 Reflection Coefficient Analysis

The comparison graph of reflection coefficient, observed by FDTD (in MATLAB), FIT (in CST) and Network Analyzer (Measured), is shown in Figure 4.9. It is explicit that the antenna is covering large bands of 1540 MHz (1.66 GHz-3.20 GHz), 1010 MHz (3.58 GHz-4.59 GHz), 1000 MHz (5.6 GHz to 6.6 GHz). This design covers LTE, DCS, PCS, UMTS and GSM in first band along with the ZigBee, Bluetooth

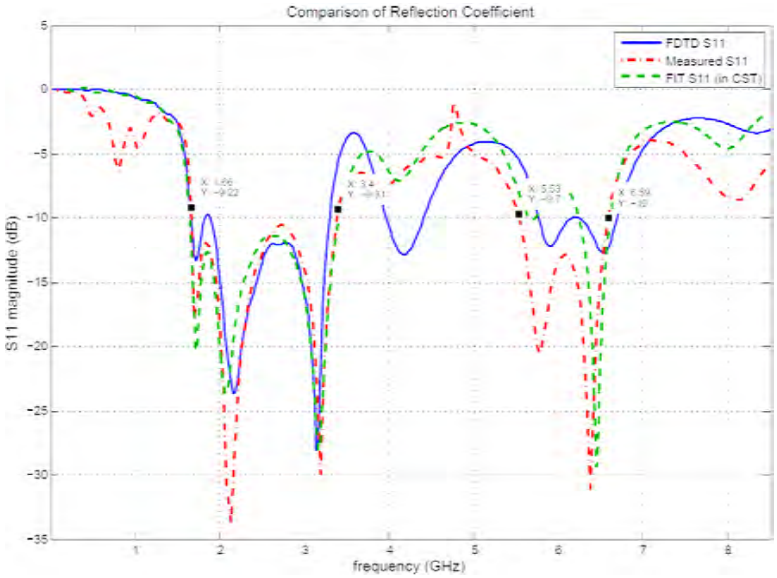

Figure 4.9: Reflection Coefficient

and WLAN 2.4 GHz applications. The second and third bands are covering most of the ultra wideband (UWB) range including the WLAN 5.8 GHz applications.

4.5 Radiation Pattern Analysis

Observed Radiation Patterns in MATLAB are shown in Figures 4.10 to 4.17. These radiation patterns are without the consideration of Human Head Model inclusion. Radiation Patters will change when the multiple dielectrics of Human Head model will interact with the antenna radiations.

4.6 Mobile/Tablet Structure Design

A generalized small Tablet (Mobile may also be modeled with similar dimensions) structure has been designed to observe Specific Absorption Rate (SAR), in CST. Mobile circuitry has not been involved. All the parameters, used in this analysis are

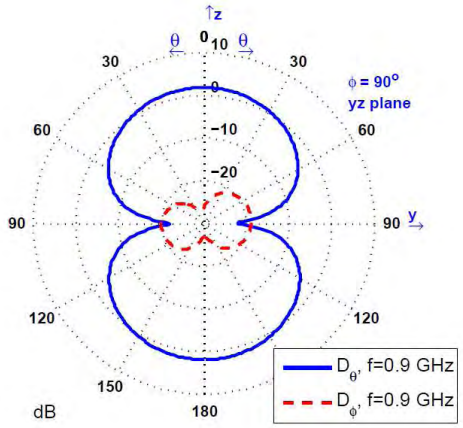

(a) $\theta = 90°$

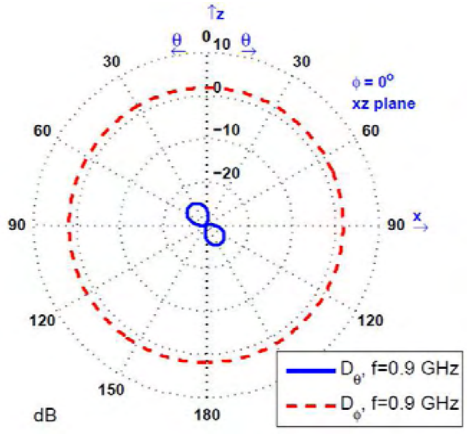

(b) $\phi = 0°$

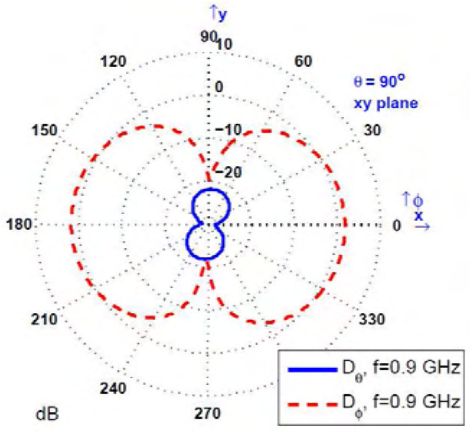

(c) $\phi = 90°$

Figure 4.10: Frequency = 0.9 GHz

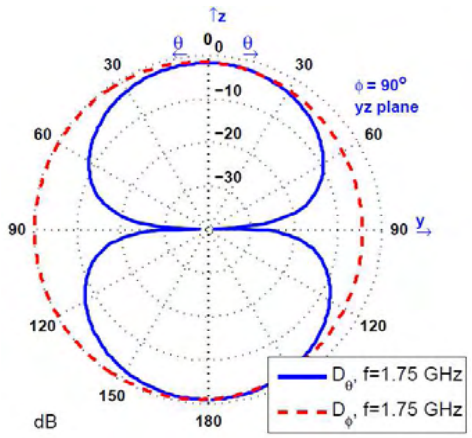

(a) $\theta = 90°$

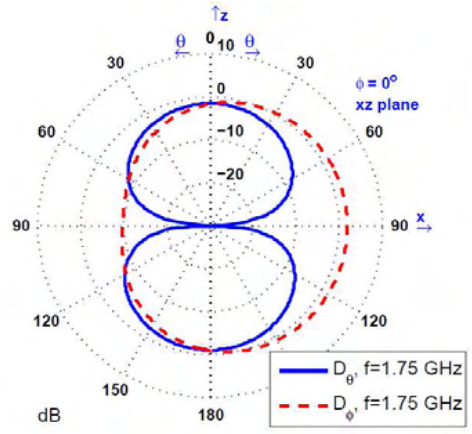

(b) $\phi = 0°$

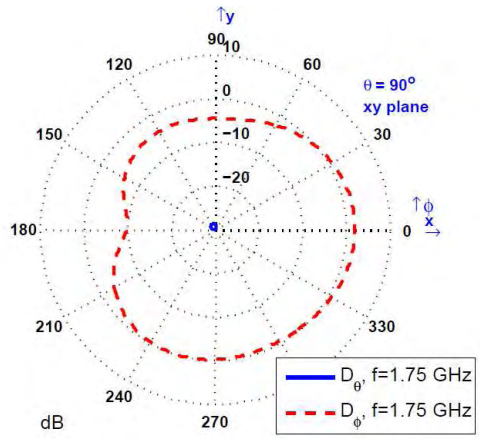

(c) $\phi = 90°$

Figure 4.11: Frequency = 1.75 GHz

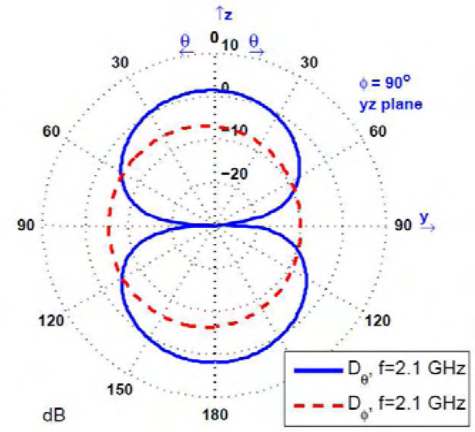

(a) $\theta = 90°$

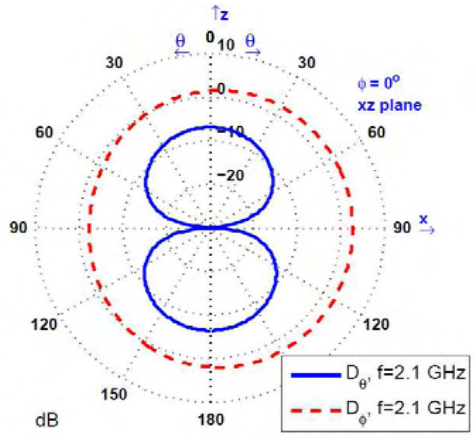

(b) $\phi = 0°$

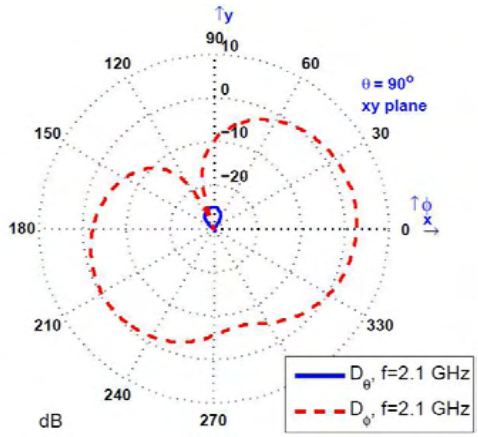

(c) $\phi = 90°$

Figure 4.12: Frequency = 2.1 GHz

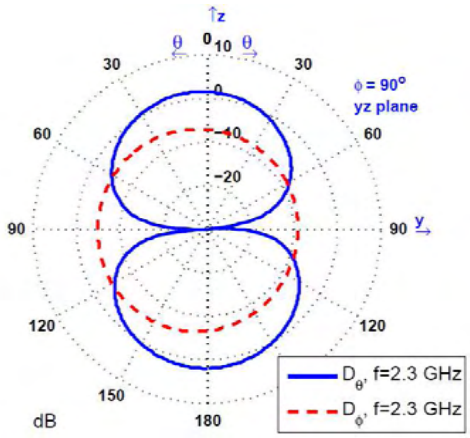

(a) $\theta = 90°$

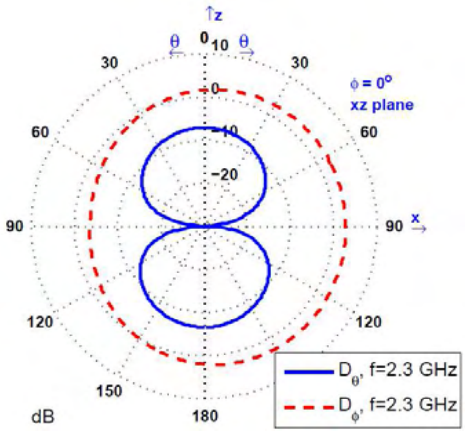

(b) $\phi = 0°$

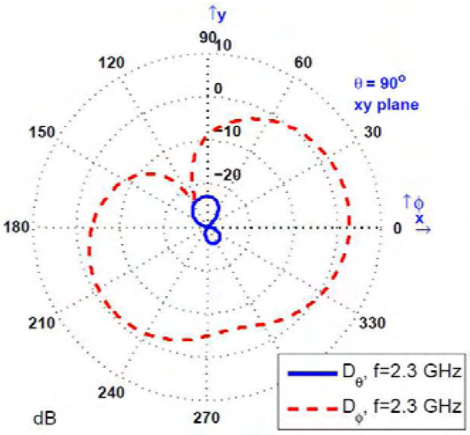

(c) $\phi = 90°$

Figure 4.13: Frequency = 2.3 GHz

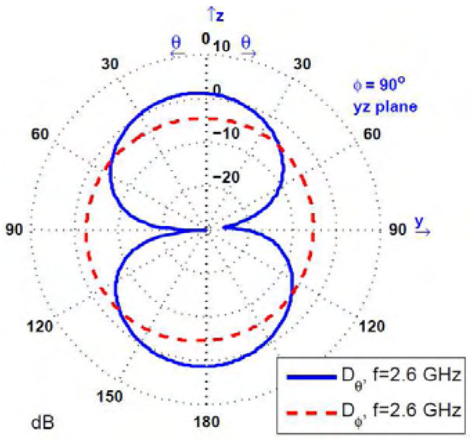

(a) $\theta = 90°$

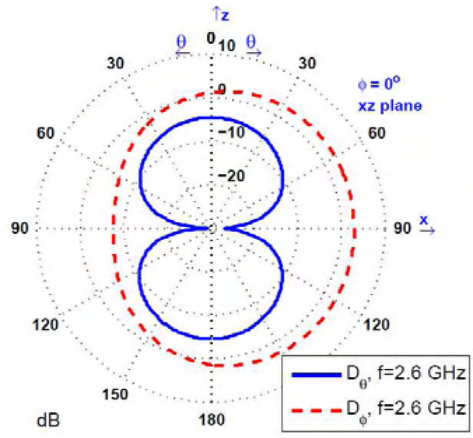

(b) $\phi = 0°$

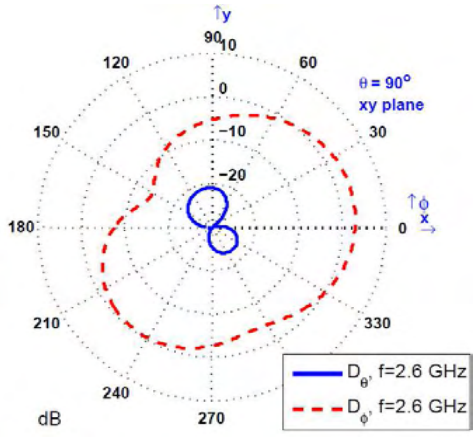

(c) $\phi = 90°$

Figure 4.14: Frequency = 2.6 GHz

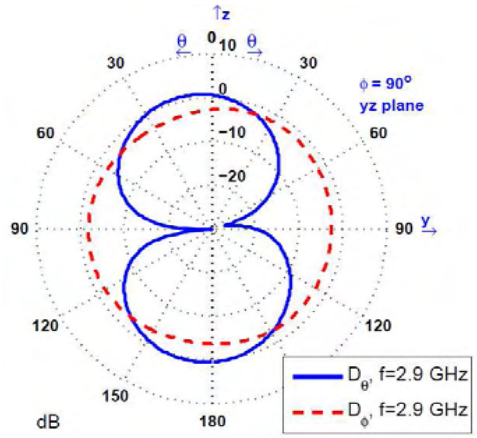

(a) $\theta = 90°$

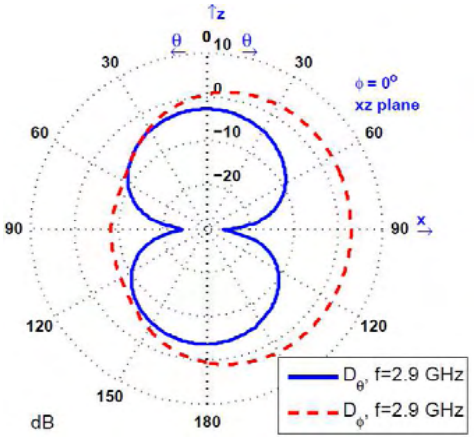

(b) $\phi = 0°$

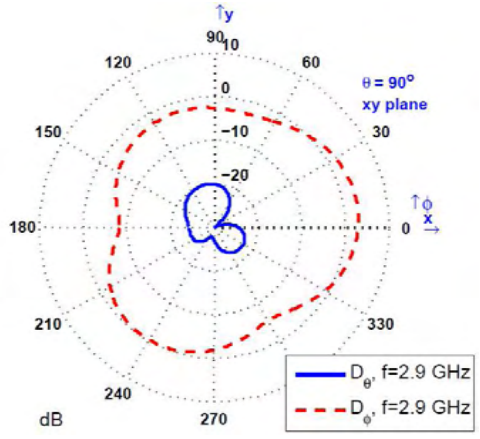

(c) $\phi = 90°$

Figure 4.15: Frequency = 2.9 GHz

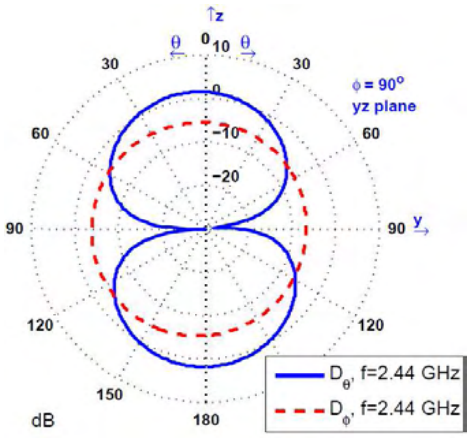

(a) $\theta = 90°$

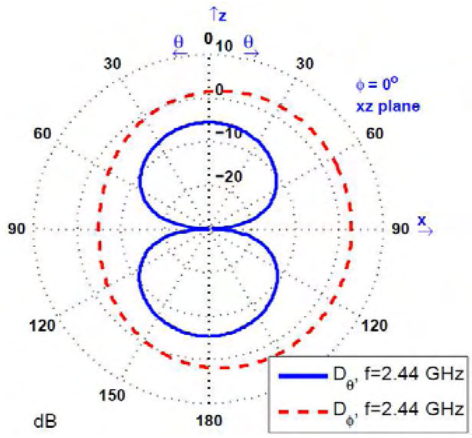

(b) $\phi = 0°$

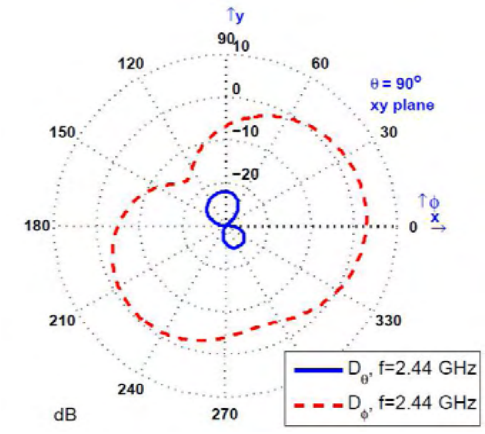

(c) $\phi = 90°$

Figure 4.16: Frequency = 2.44 GHz

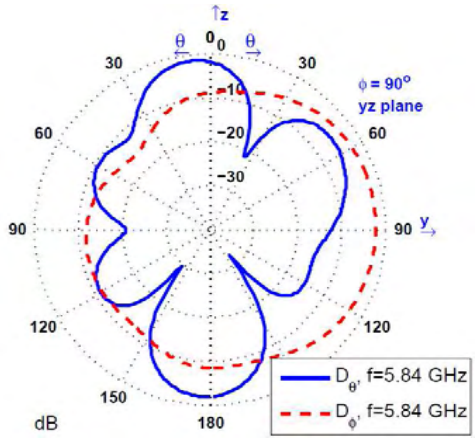

(a) $\theta = 90°$

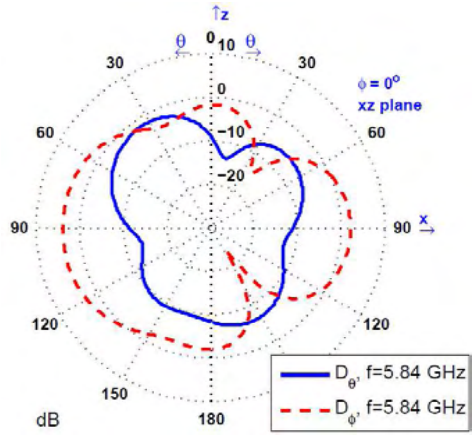

(b) $\phi = 0°$

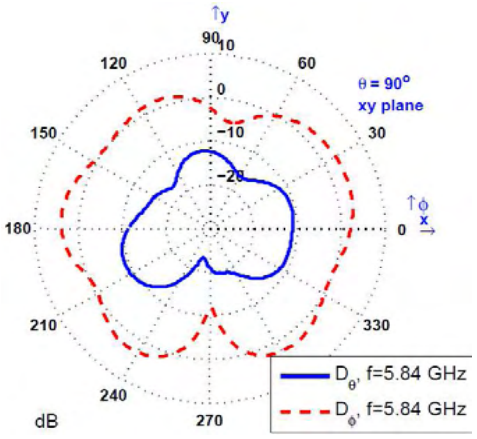

(c) $\phi = 90°$

Figure 4.17: Frequency = 5.84 GHz

listed in table 4.4. Mobile body dimensions are decided using general measurements

Sr. No.	Parameter	Value
1.	Mobile Body Length	121.5 mm
2.	Mobile Body Width	61.5 mm
3.	Mobile Body Depth	8 mm
5.	Mobile Body Material	Plastic
6.	Mobile Body Thickness	0.75 mm
7.	LCD Length	103 mm
8.	LCD Width	56 mm
9.	LCD Thickness	0.75
10.	LCD Material	LCD Film

Table 4.4: FDTD implementation related parameters

through observation of mostly used mobile and tablet products. The Mobile/Tablet structure is shown in Figure 4.18. Main reason is that, dimensions provided in this

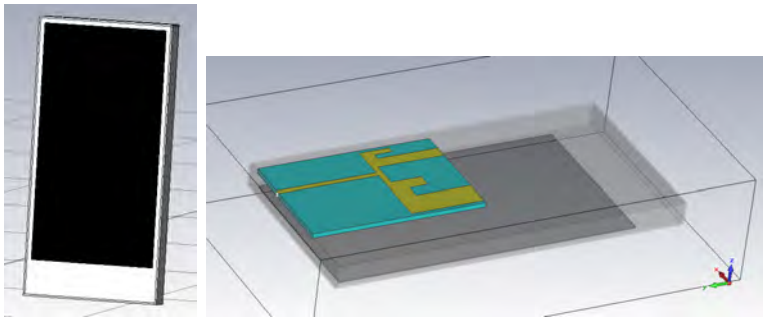

(a) Structure (b) Mounted Antenna on Back PCB

Figure 4.18: Mobile/Tablet Structure

work, are used for both the products, mobile, as well as, tablet. Mobile body is made up of plastic material defined in CST, which has dielectric constant of 2.5. LCD display is designed in such a way that it gives small space for additional buttons downwards the mobile. The reason for this is that some of the mobiles and tablets, even after touch screen, have a few buttons on downward side. LCD Film is used as LCD display material. LCD Film has dielectric constant of 4.78.

4.7 SAR Calculations

Specific Absorption Rate is an important parameter to verify the feasibility of any mobile or wireless communication system. SAR is a major parameter to be calculated before any mobile communication device antenna has been finalized. SAR increases temperature in the human body. For our consideration, tissue models are taken. This temperature rise causes health problems for humans. There are different standards like ANSI C95.1 standard, ICNIRP guidelines, European Council Recommendation etc., which provide necessary limits of SAR and effects of higher SAR in human body [113]-[117]. Federal Communications Commission (FCC), Australian Communications Authority (ACA) Standard and European ICNIRP Guidelines have given some limits for the SAR in human tissue [118]. These limits are shown in Table 4.5. Generally 10 g tissue is considered for Calculations but FCC and ACA emphasize on 1 g tissue also. In this work European standard EN 50361

Sr. No.	Standard	SAR (W/kg)
1.	European ICNIRP Guidelines	2.0
2.	Federal Communications Commission (FCC)	1.6
3.	Australian Communications Authority (ACA)	1.6

Table 4.5: SAR standards

is used for calculations of SAR. According to this standard, human phantom model has homogeneously filled tissue parameters [116]. In comparison to this standard, European standard EN 50357 is more rigid, because one needs to use all the different parameters for tissues of each part of body in complete human phantom model [113]. SAR is generally defined as follows:

$$SAR = \frac{\sigma E^2}{\rho} \tag{4.1}$$

Here, σ is conductivity, E is the magnitude of electric field strength and ρ is the tissue density.

4.7.1 SAR Calculations for Proposed Antenna

The SAR calculation is inspired from literature [55, 56, 57, 62]. For tissue, human head Voxel model is utilized which is provided by CST with the tool itself [24]. Dispersion for liquid, used in Voxel model, is applied according to CST standards only. Human head is modeled with Voxel model provided by CST as shown in Figure 4.19. Observed SAR values, for the proposed antenna design are tabulated

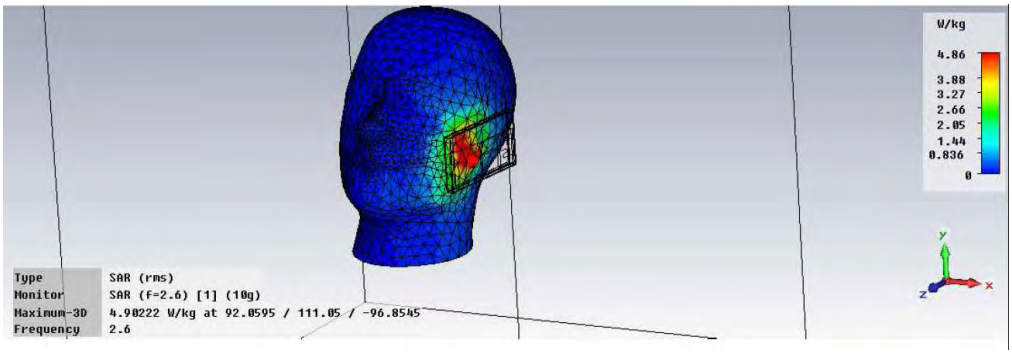

Figure 4.19: SAR Analysis in CST

in Table 4.6 The proposed antenna is providing Directivity between 1.5 dBi to 4.5

Sr. No.	Frequency (GHz)	SAR (W/kg) w.r.t. 10 g
1.	0.9	8.083
2.	1.7	4.930
3.	1.8	4.809
4.	1.9	4.817
5.	2.1	4.846
6.	2.3	4.868
7.	2.44	4.917
8.	2.6	4.902
9.	2.9	4.710

Table 4.6: SAR Values at Different Frequencies

dBi for different observed frequency range. This is good for mobile applications,

where mostly radiation is required to be approximately omnidirectional. Radiation efficiency is within the range of -0.009 dB to -0.221 dB. Radiation Patterns results are tabulated in Table 4.7.

Sr. No.	Frequency	Directivity	Rad. Eff.
	GHz	dBi	dB
1.	0.9	1.57	-0.221
2.	1.75	2.67	-0.198
3.	2.1	3.14	-0.009
4.	2.3	3.31	-0.033
5.	2.6	3.40	-0.016
6.	2.9	3.50	-0.013
7.	2.44	3.39	-0.012
8.	5.84	4.64	-0.049

Table 4.7: Radiation Pattern Results

4.7.2 Reducing SAR

There are many parameters, which affect the antenna performance with respect to SAR. After a lot of observations, it has been concluded that, SAR can be reduced by using Full PCB and Ground plane tuning. Observations are not only been taken on the Ground and Feed, there are observations on fingers also, to take reflection coefficient analysis into consideration.

Reflection Coefficient analysis

Whenever antenna is analyzed individually, it shows good Reflection coefficient, if proper design dimensions are used. But whenever the antenna is analyzed with Human Head Voxel Models (shown in next section), reflection coefficient shows some changes in comparison to the results obtained by considering individual antennas. To avoid any discrepancy, observations were taken for both analyses. There are different configurations created and observed for this analysis. More than 500 different configurations were observed. Main configurations are tabulated in Table 4.11 (This

table is shown in the end of this chapter, because of large size of it). Here H is the base height, which is 2.1 mm. This is described in 2.2.2 and shown in Figure 2.6. Main observations for individual antenna analysis are shown in three different figures, to reduce the complexity for observer. Conclusions are decided according to not only reflection coefficient but also the SAR values within the limits. Observations for antenna configurations within Handset are shown in Figures 4.20, 4.21 and 4.22. Here no human head model is considered to observe the reflection coefficient.

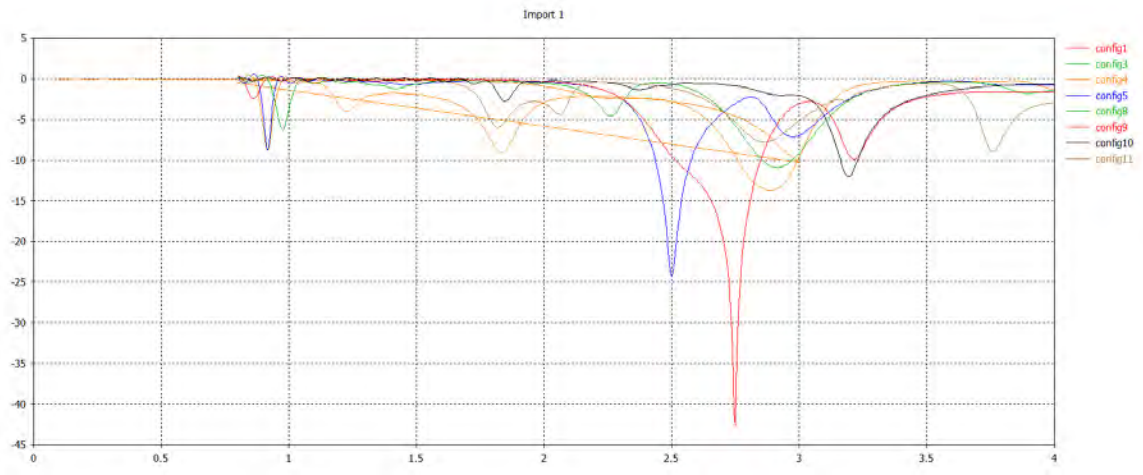

Figure 4.20: Reflection Coefficient comparison: configuration 1-11

After observing all the antenna configurations with handset without human head inclusion in the model, next analysis is done with considering human head model. All the observed reflection coefficients are compared with respective, without human head models. But putting all the comparative results here is not feasible. So as, similar to previous analysis, here also, three figures are shown to explain the observations for same configuration as previous analysis. Figures 4.23, 4.24 and 4.25 are showing the reflection coefficients observed for antennas with Human Head consideration in the model.

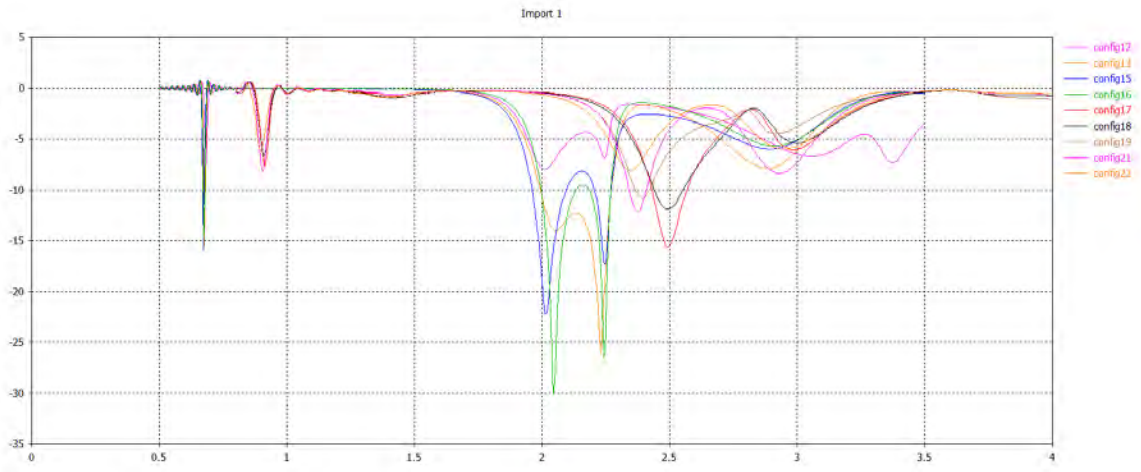

Figure 4.21: Reflection Coefficient comparison: configuration 12-22

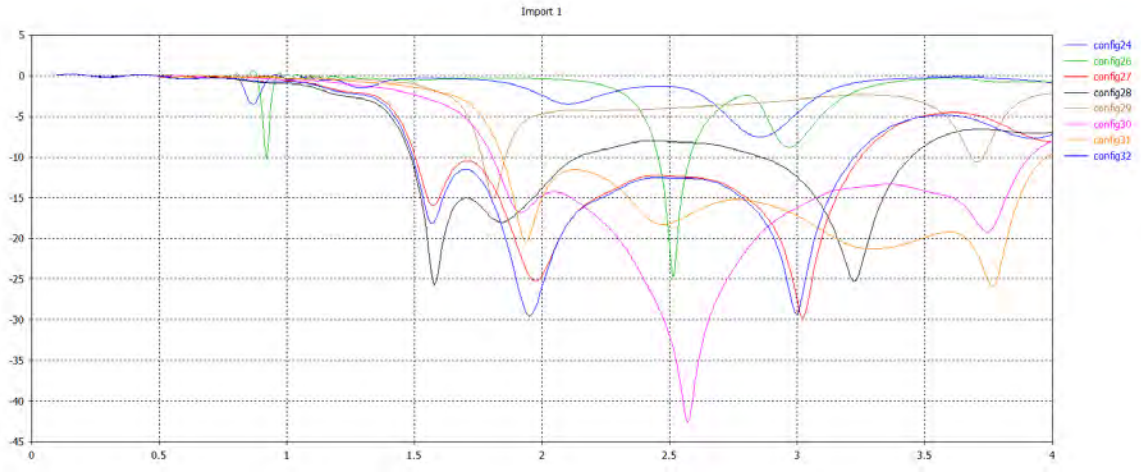

Figure 4.22: Reflection Coefficient comparison: configuration 24-32

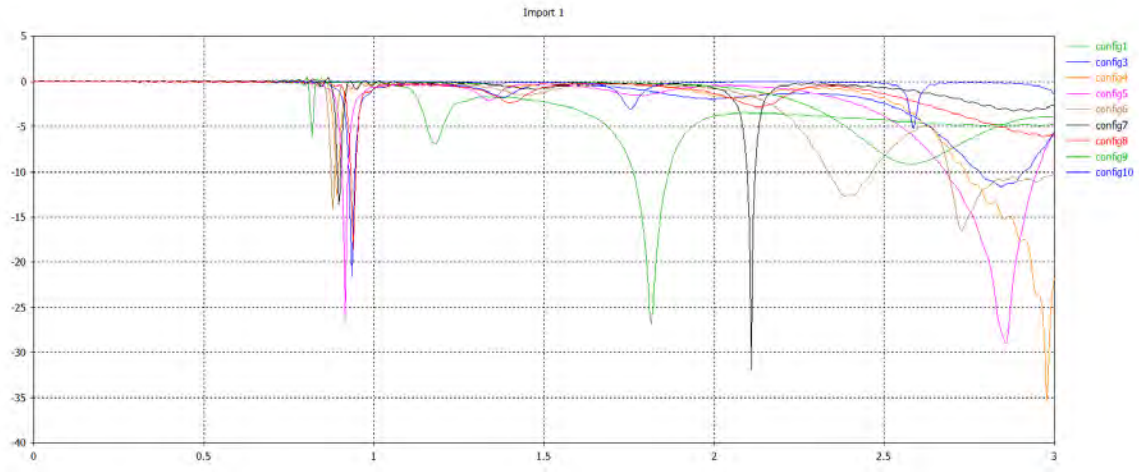

Figure 4.23: Reflection Coefficient comparison with human head consideration: configuration 1-10

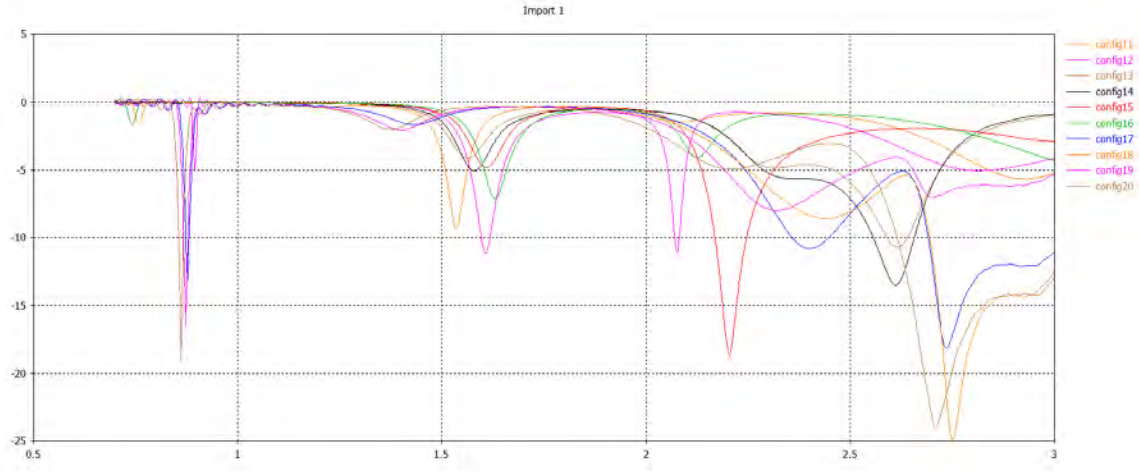

Figure 4.24: Reflection Coefficient comparison with human head consideration: configuration 11-20

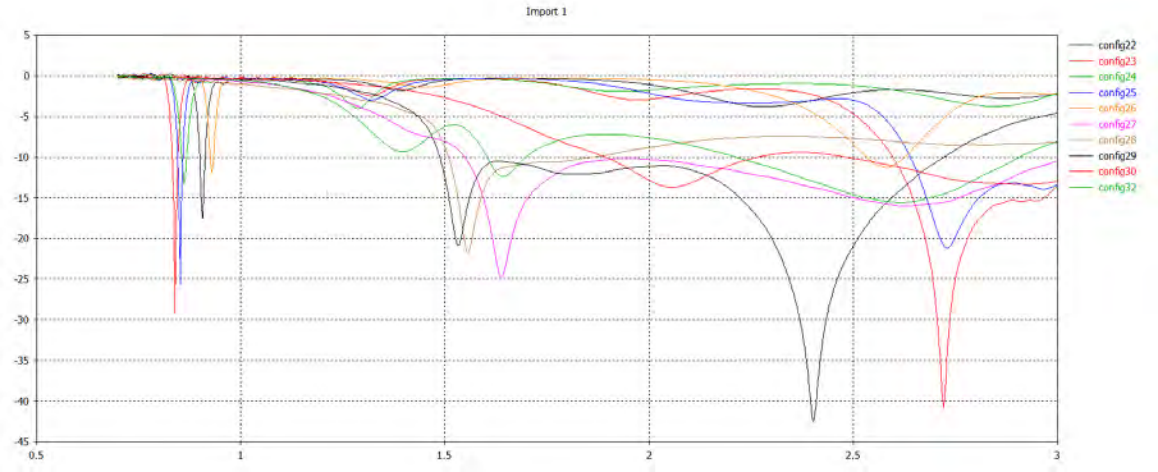

Figure 4.25: Reflection Coefficient comparison with human head consideration: configuration 21-32

Full PCB

Full PCB is designed to confine the radiations from the edges of the Antenna. These additional Fields are now restricted to interact with human body. So after observations, PCB size has been taken same as LCD film, which is a general case for mobile handset. The new model is shown in Figure 4.26 Reflection coefficient is also affected due to the Human head. This comparison can be observed in Figure 4.27. SAR for frequency 2.9 GHz is shown as an example in Figure 4.28. Observed SAR values for full PCB model are tabulated in Table 4.8

Sr. No.	Frequency (GHz)	SAR (W/kg) w.r.t. 10 g
1.	1.7	2.20
2.	1.8	1.97
3.	1.9	1.81
4.	2.1	1.7
5.	2.3	1.68
6.	2.44	1.60
7.	2.6	1.44
8.	2.9	0.98

Table 4.8: SAR Values for Full PCB Model at Different Frequencies

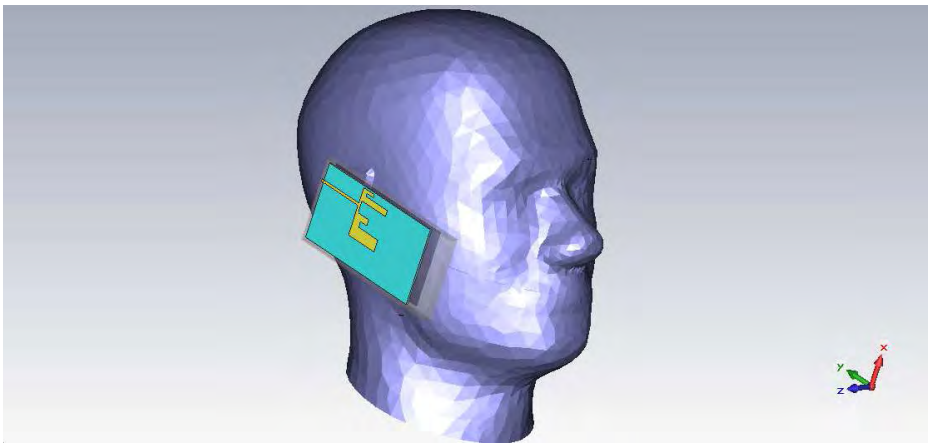

Figure 4.26: Mobile Handset with Full PCB

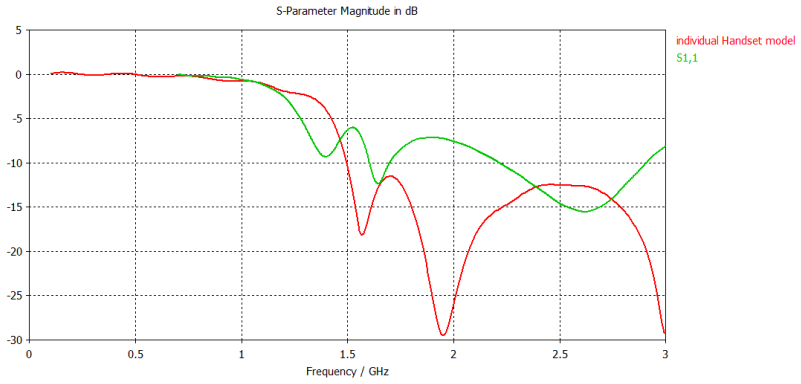

Figure 4.27: Full PCB: S11 comparison of simulation of individual Full PCB Handset and with Human Head

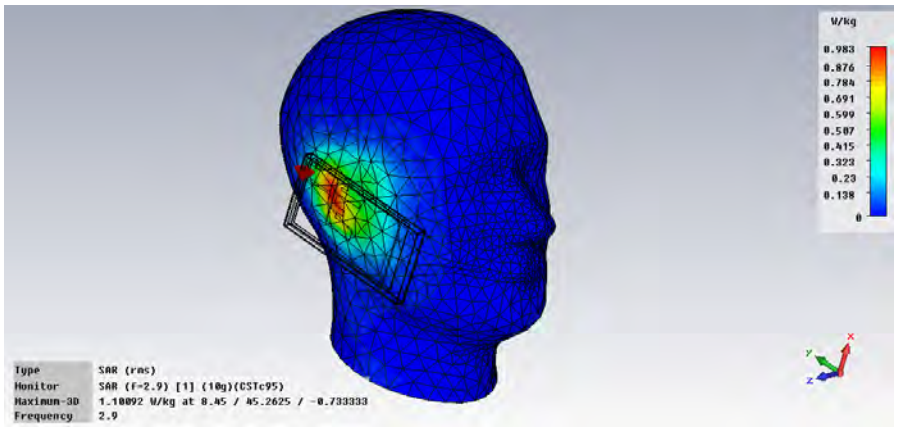

Figure 4.28: Full PCB: SAR at 2.9 GHz Full PCB Handset and with Human Head

Ground Tuning

In this work, some tuning of ground is done to achieve proper S11 and correspondingly lower SAR. As the ground and Feed length are together generating coupling and in turn, wide band reflection coefficient, so as Microstrip Feed length is also varied corresponding to the Ground. Ground reflects the back radiations towards head. Ground is now tuned to 34 mm and correspondingly Microstrip feed is 36.4 mm. Reflection coefficient is now a little bit reduced due to modifications in the model. The comparison of Reflection coefficient for models with individual Handset model and Handset with Human Head, is shown in Figure 4.29. SAR for frequency 2.9 GHz is shown as an example in Figure 4.30. Observed SAR values for ground tuned full PCB model are tabulated in Table 4.9 Finally observed radiation efficiency is also improved and Directivity is better than the previous results. These are tabulated in table 4.10 All the radiation patters are shown in following Figures 4.33 to 4.37.

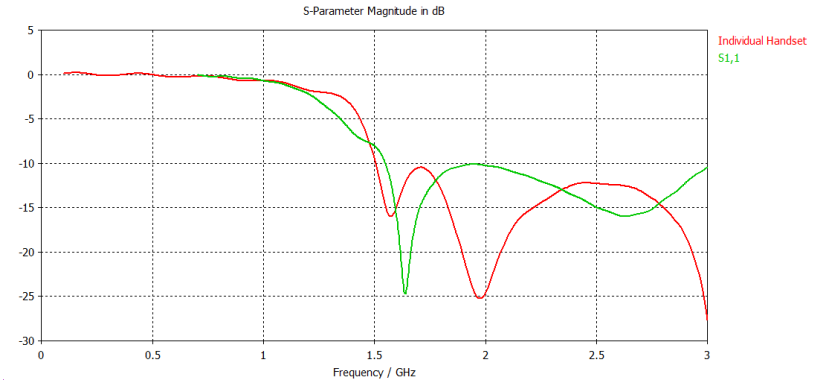

Figure 4.29: Full PCB and Ground Tuning: S11 comparison of simulation of individual Full PCB Handset and with Human Head

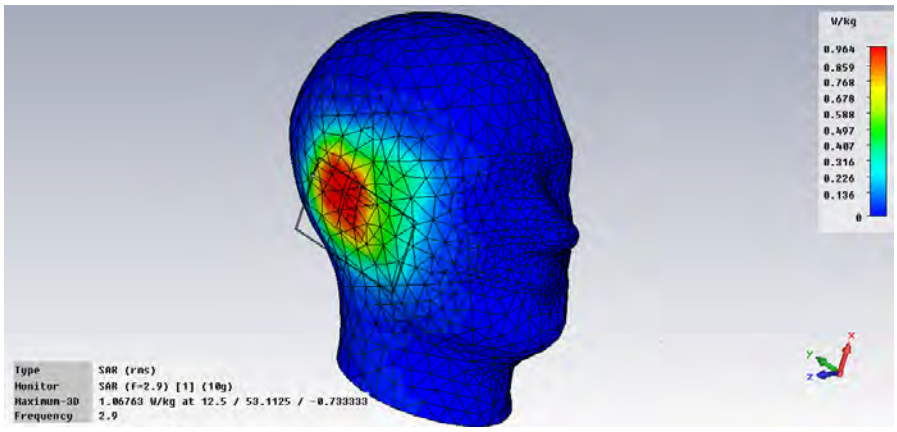

Figure 4.30: Full PCB and Ground Tuning: SAR at 2.9 GHz Full PCB Handset and with Human Head

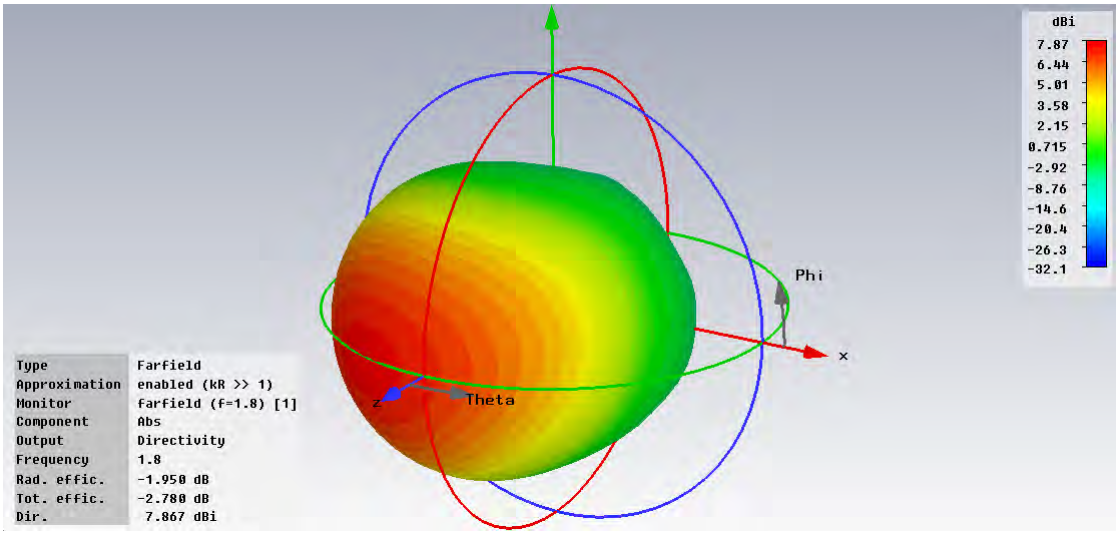

Figure 4.31: Radiation Pattern at 1.8 GHz

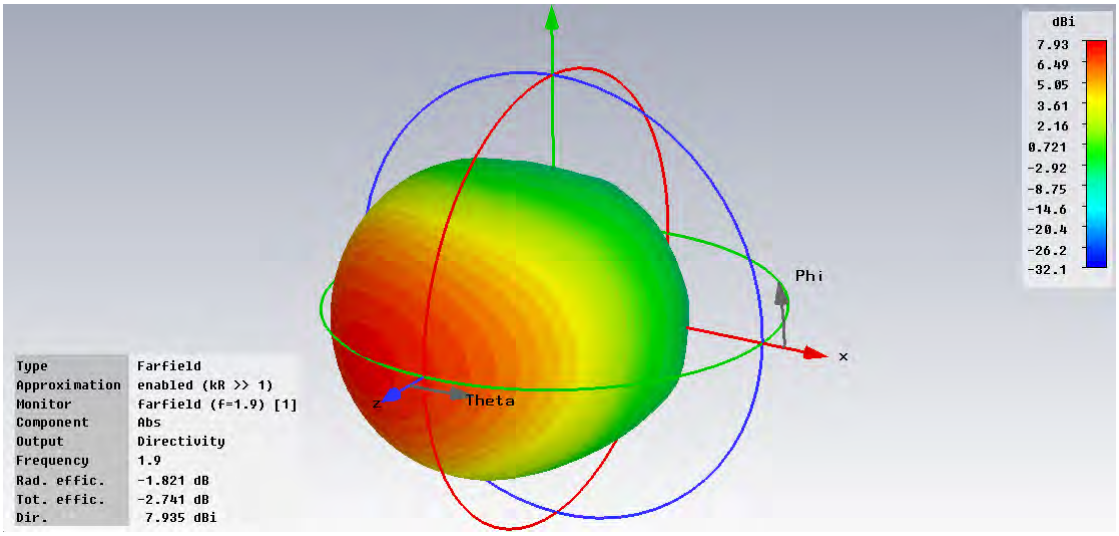

Figure 4.32: Radiation Pattern at 1.9 GHz

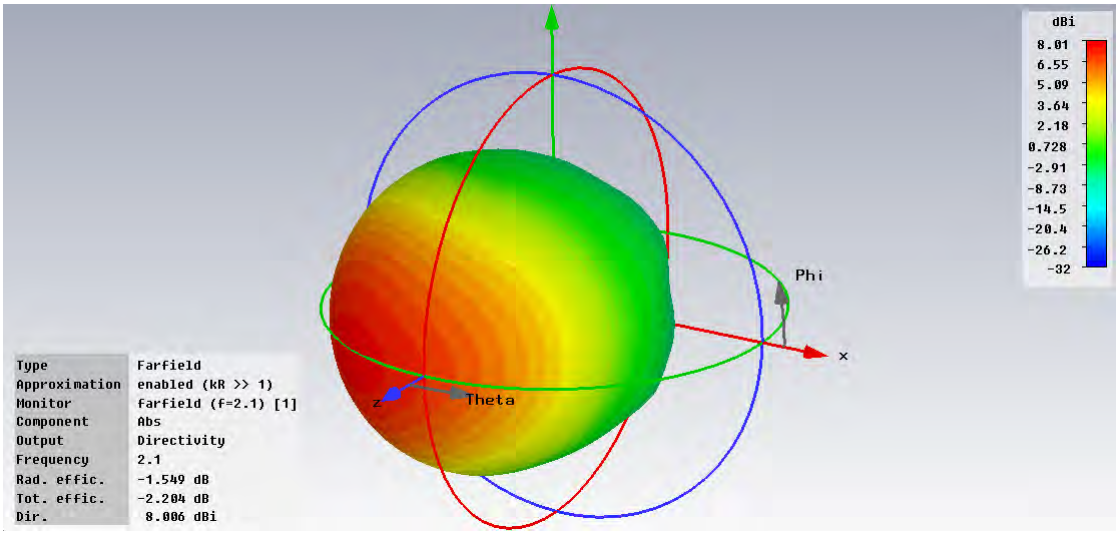

Figure 4.33: Radiation Pattern at 2.1 GHz

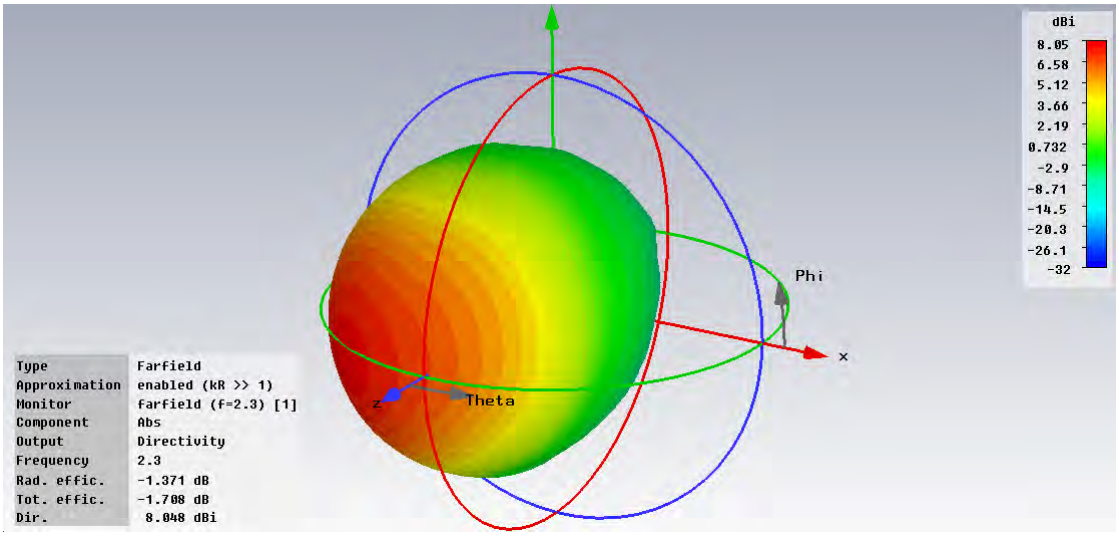

Figure 4.34: Radiation Pattern at 2.3 GHz

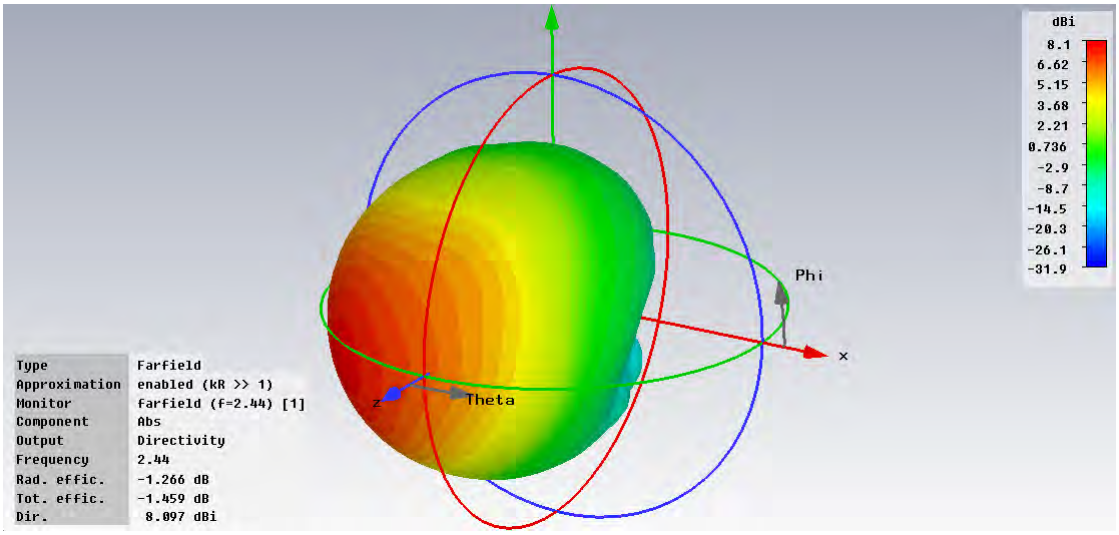

Figure 4.35: Radiation Pattern at 2.44 GHz

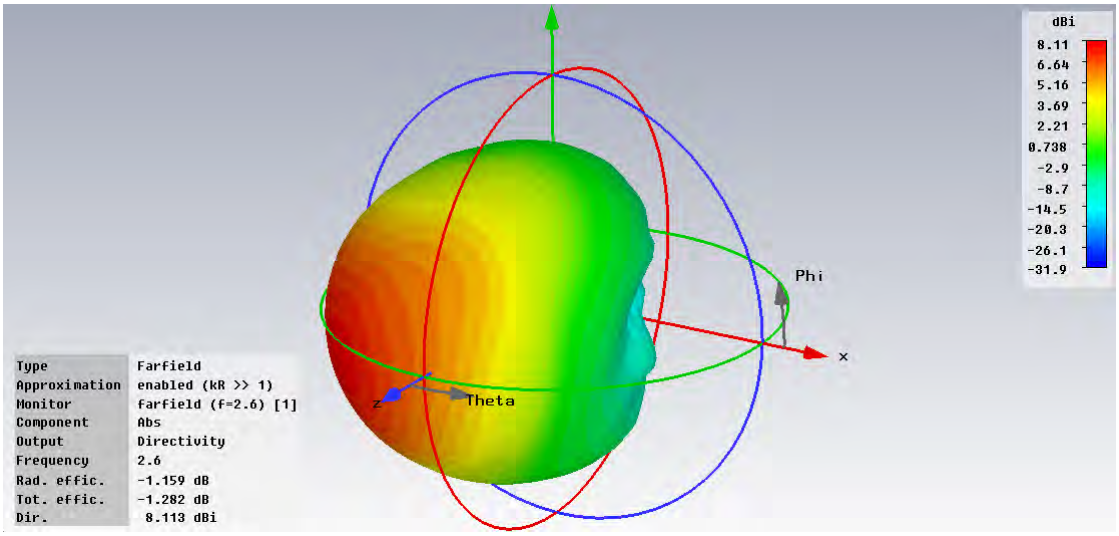

Figure 4.36: Radiation Pattern at 2.6 GHz

Sr. No.	Frequency (GHz)	SAR (W/kg) w.r.t. 10 g
1.	1.7	2.06
2.	1.8	1.77
3.	1.9	1.63
4.	2.1	1.59
5.	2.3	1.62
6.	2.44	1.55
7.	2.6	1.40
8.	2.9	0.96

Table 4.9: SAR Values for Ground tuned Full PCB Model at Different Frequencies

Sr. No.	Frequency	Directivity	Rad. Eff.
	GHz	dBi	dB
1.	1.8	7.87	-1.95
2.	1.9	7.94	-1.82
3.	2.1	8.00	-1.55
4.	2.3	8.05	-1.37
5.	2.6	8.11	-1.15
6.	2.9	8.17	-0.98
7.	2.44	8.09	-1.27

Table 4.10: Radiation Pattern Results after reduced SAR

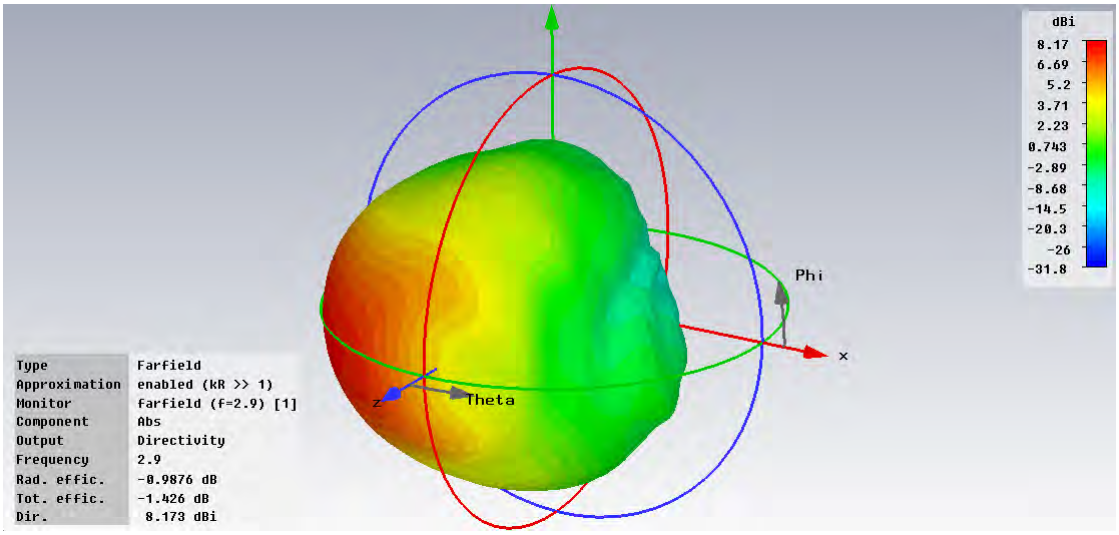

Figure 4.37: Radiation Pattern at 2.9 GHz

4.8 Conclusion of this Chapter

Antenna finger dimensions are optimized using observations in MATLAB and CST Studio Suite. This part of the work is published in [24]. Revised cantor geometry based low profile, compact LTE fractal antenna is proposed for Mobile/Tablet PC applications. The proposed antenna is appropriately covering several wireless applications, including LTE 1.7-1.8 GHz band, 2.3 GHz, 2.6 GHz and 2.9 GHz applications, WLAN 2.4 GHz and 5.8 GHz applications, GSM, UMTS, DCS, ZigBee, PCS, applications. Radiation Patterns are analyzed. Observations show almost omnidirectional behavior of the antenna, for all the observed frequencies with Directivity between 1.5 dBi to 4.5 dBi and Radiation Efficiency is within the range of -0.009 dB to -0.221 dB. Experimental results present accurate matching with theoretical results. SAR is less than 5 W/kg for 10 g tissue, without mobile circuitry and without Full PCB. The SAR can be reduced by using Full PCB and tuning the ground plane properly. Some compromise between S11 and SAR has to be considered. After applying reduction techniques, SAR is within 1.6 W/Kg for most of the frequencies, which is the general standard requirement. Directivity is now between 7.72 dBi to 8.17 dBi and Radiation Efficiency is within the range of -0.98 dB to -1.95 dB.

configuration	h1	h2	h3	h4	Ground	Feed
	(mm)	(mm)	(mm)	(mm)	(mm)	(mm)
1	H x 9	H x 3	H x 10	H x 3	5	7.4
2	H x 9	H x 3	H x 10	H x 5	5	7.4
3	H x 10	H x 5	H x 5	H x 17	15	7.4
4	H x 10	H x 5	H x 7	H x 14	15	7.4
5	H x 14	H x 5	H x 6	H x 9	28	30
6	H x 12	H x 5	H x 6	H x 9	13	4
7	H x 12	H x 9	H x 3	H x 9	32	34.4
8	H x 13	H x 4	H x 7	H x 12	10	14
9	H x 14	H x 5	H x 3	H x 8	8	4
10	H x 12	H x 7	H x 3	H x 9	8	4
11	H x 11	H x 5	H x 5	H x 17	8	12
12	H x 13	H x 5	H x 3	H x 16	5	5
13	H x 13	H x 5	H x 5	H x 19	5	7.4
14	H x 4	H x 3	H x 2	H x 1	5	
15	H x 4	H x 3	H x 2	H x 1	5	7.4
16	H x 7	H x 3	H x 3	H x 5	5	4
17	H x 15	H x 5	H x 6	H x 9	13	115.4
18	H x 16	H x 5	H x 6	H x 9	13	5
19	H x 16	H x 6	H x 6	H x 9	13	15.4
20	H x 16	H x 5	H x 6	H x 11	13	5
21	H x 14	H x 5	H x 6	H x 11	25	5
22	H x 16	H x 6	H x 6	H x 9	12	14.4
23	H x 17	H x 5	H x 6	H x 14	13	4
24	H x 19	H x 6	H x 6	H x 14	25	27.4
25	H x 19	H x 5	H x 6	H x 11	13	15.4
26	H x 13	H x 5	H x 6	H x 9	13	5
27	H x 9	H x 3	H x 10	H x 3	32	34.4
28	H x 9	H x 3	H x 10	H x 3	30	34.4
29	H x 6	H x 3	H x 6	H x 2	36	34.4
30	H x 6	H x 3	H x 6	H x 2	25	27.4
31	H x 6	H x 3	H x 6	H x 2	15	17.4
32	H x 9	H x 3	H x 10	H x 3	34	36.4

Table 4.11: Main configurations for observations, H = 2.1 mm

Chapter 5

Additional Research Work

5.1 Fractal Antenna on Substrates with High Dielectric Constant

Analysis of Revised Cantor geometry based fractal antenna, proposed in [25], with different dielectric constants, is also done. Objective of this analysis is to produce wide multiband antenna with lower reflection coefficient, i.e., as less as possible. Antenna Design is shown in Section 3.1 on Teflon substrate. Observations are taken for substrate with different dielectric constants which are shown in Table 5.1. Thisckness of substrates is considered same as the model considered in chapter 3, which is 1.6 mm. BST is Barium Strontium Titanate which is very high dielectric constant 50.

Sr. No.	Substrate	ϵ	Resonances in GHz
1.	RT-Duroid	2.2	1.72, 2.18, 3.14, 4.16, 5.86, 6.56, 9.94
2.	FR4	4.4	1.72, 2.18, 3.14, 4.16, 5.86, 6.56, 9.94
3.	Alumina	9.9	1.54, 1.94, 2.28, 3.18, 5.81, 6.45, 7.72, 9.92
4.	BST	50	1.12, 1.74, 3.58, 3.98, 4.76, 5.62, 5.94, 7.08, 7.78, 8.34, 8.98, 9.56

Table 5.1: Resonances for substrate with different dielectric constants

As can be observed, higher dielectric constant materials increase resonances.

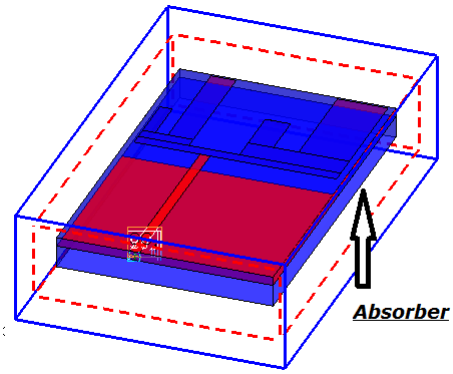

Figure 5.1: Fractal Antenna with Absorber below Ground Plane

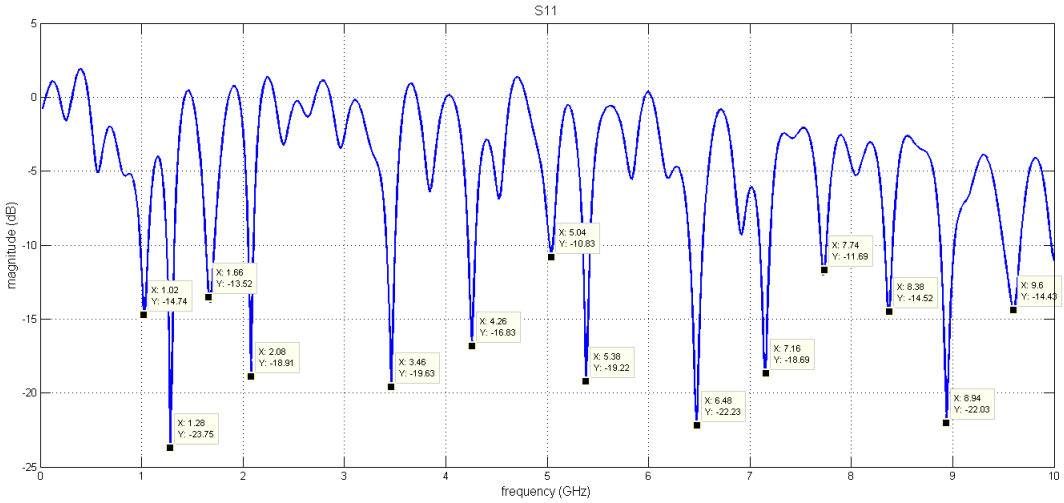

Figure 5.2: S11 of Fractal Antenna with Absorber below Ground Plane

These increased resonances develop interruptions in resonating fields of the antenna. The main reason is that, these substrates (High dielectric constant) produce surface currents [69]-[75]. These surface currents maybe reduced by using microwave absorbers below the ground plane as shown in Figure 5.1 Reflection Coefficient of proposed fractal antenna with absorber below the ground plane is shown in Figure 5.2. Observations have been taken for fractal antenna with an absorber below ground. Standard rubber absorber is used, with Permeability of 1.5. Dielectric constant is also varied. Thickness t of the absorber is taken as the variable parameter.

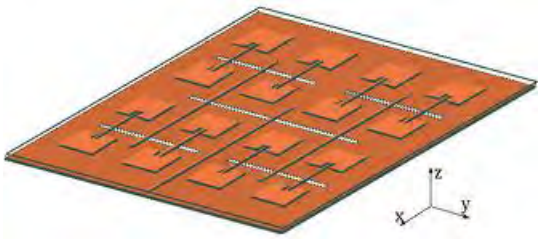

Figure 5.3: A Generalized Antenna Array

Main observations are tabulated in Table 5.2. Main conclusion that can be carried

Sr. No.	Substrate	ϵ	t	Resonances in GHz
1.	Glass Leaded	7.5	4	1.02, 1.28, 1.66, 2.08, 3.46, 4.26, 5.04, 5.38, 6.48, 7.16, 7.74, 8.38, 8.94, 9.6 (with higher bandwidth)
2.	Glass Leaded	7.5	13	0.98, 1.24, 1.66, 2.04, 3.42, 4.26, 5.4, 6.44, 6.9, 7.41, 7.7, 8.32, 8.94, 9.5 (with higher bandwidth)
3.	Phenolics (Silicate)	18	13	0.52, 0.88,1.14, 1.6, 1.88, 2.82, 3.28, 4, 4.4, 4.9, 5.2, 5.7, 6.36, 7.1, 7.68, 8.24, 8.9, 9.58

Table 5.2: Resonances variation with Absorber Thickness and Dielectric Constant

out from the analysis is that an absorber and Substrate with high dielectric constant can produce Multiband in wide range. Absorbers will minimize the effect of the surface currents produced additionally.

5.2 Fractal Antenna Array Design

Matrix or Array of similar or different antennas, arranged in a specific manner, to achieve larger Gain and better reflection coefficient, is known as antenna array. Enormous amount of literature is available for antenna array design [76]-[82]. Antenna array for fractal antenna design is a new challenging research topic nowadays. Major challenge is to maintain higher gain on all resonances produced by a multiband fractal antenna. A generalized antenna design is shown in Figure 5.3. Mainly

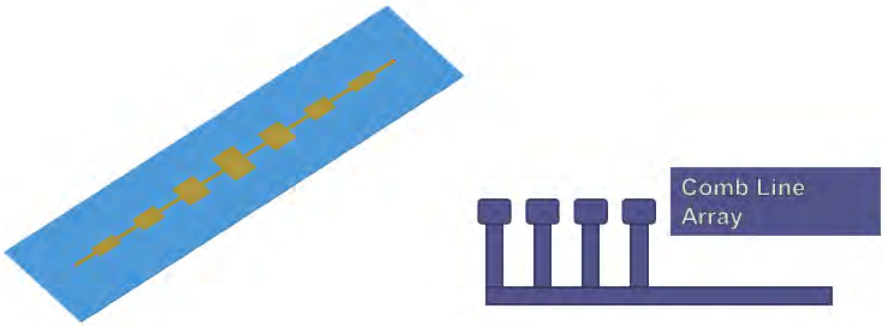

Figure 5.4: Series Fed Antenna Array

antenna arrays are classified as per their arrangement of elements. Following is the terminology used for types of antenna array:

1 Series Fed

2 Parallel (Corporate) Fed

3 Combination of Series and Parallel Feed

4 Phase Feed (This is used for generating polarization)

A series fed antenna array is designed in such a way that all array elements have feed line which feeds every element in linear pattern [75, 76]. An example is shown in Figure 5.4. Combline arrays are considered in series fed type of array only. In this kind of antenna array configuration, array elements are arranged as tooth of comb [76, 77, 79, 83]. Corporate or parallel fed antenna arrays are the most popular type of antenna array design. Every element is connected to a feed line, which then is connected to feed line of another parallel array element from Microstrip feed. This is an iterative process of connecting antenna array elements. Once all the elements are connected as parallel combinations, only one feed line is left which makes connection between source and the antenna array. A generalized Parallel fed antenna array is shown in Figure 5.5. Quarter Wave Transformers are utilized in this type, to connect different antenna stages to each other as shown in Figure 5.6. This figure

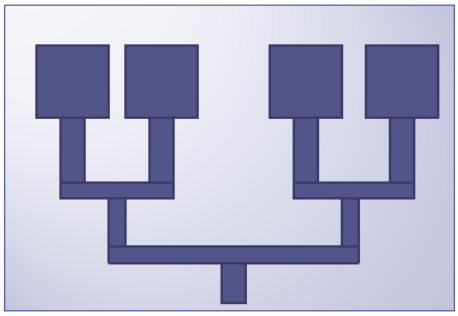

Figure 5.5: A Generalized Parallel Fed Antenna Array

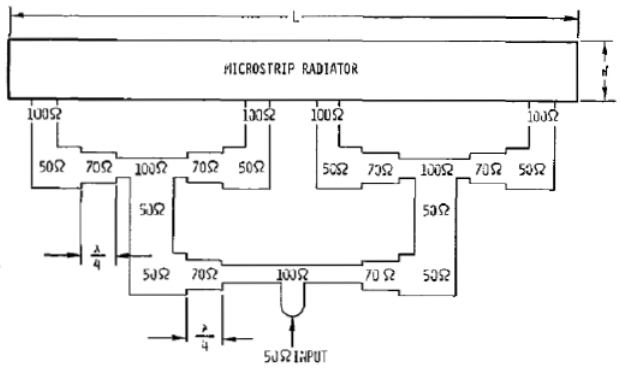

Figure 5.6: A Generalized Antenna Array

is reproduced from [75]. Using quarter wave transformer reduces the impedance mismatching problem in antenna array element connections. Quarter wave matching technique suggests to use a transmission line of length as quarter wavelength and impedance as square root of product of input and output line impedances [75, 80, 82]. Combination of the series fed and corporate fed antenna array arrangement is advantageous. It gives benefit of both the techniques. Gain is in general more in comparison to series fed antenna arrays. Disadvantages are also included like losses increase, complexity increases and mutual coupling also increases which affects the radiation characteristic of the overall antenna array configuration [79]-[84]. This type of configuration is shown in 5.7. Phased antenna arrays are just special cases of Parallel or corporate fed antenna array configuration, in which feed positions are slightly changed to increase or decrease current path lengths. These current path

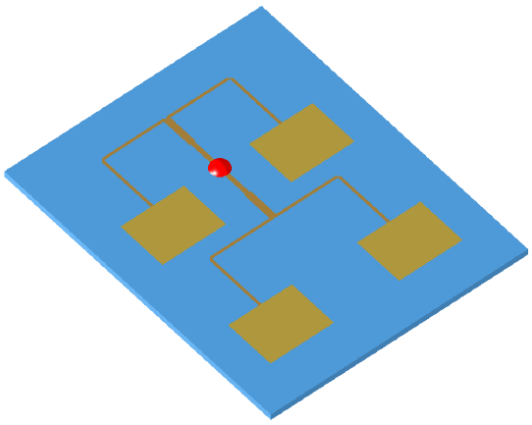

Figure 5.7: Combination of Series and Corporate Fed Antenna Array

lengths, in turn, affect the phase of the elements, connected to that section.
Series Fed is the most simple and easy to fabricate array design. So as Comb-Line Array design is chosen for revised cantor based fractal antenna array design, in which, Base element is considered as fractal antenna Proposed in [25]. There are two ways to generate Microstrip comb line array; one dimensional and two dimensional. Some Parameters are considered during the designing which are as follows:

1 m, Number of Rows in multidimensional Array

2 n, Number of antenna elements in one row

3 d(s), Spacing between two elements

4 md, Spacing between two rows

5.2.1 One Dimensional

In one dimensional array element number, n and spacing, d are the important parameters, which affect the antenna performance. Antenna array configuration in one dimension, is shown in Figure 5.8. According to observation on reflection coefficient,

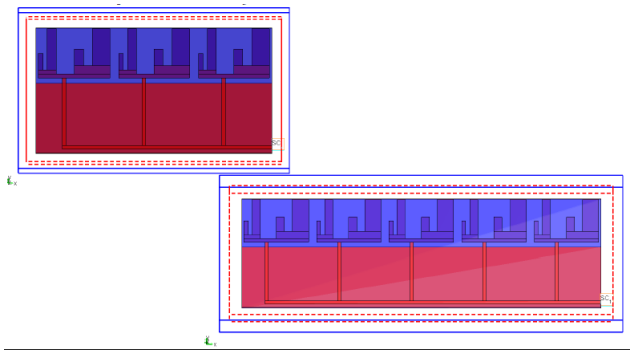

Figure 5.8: One Dimensional Antenna Array

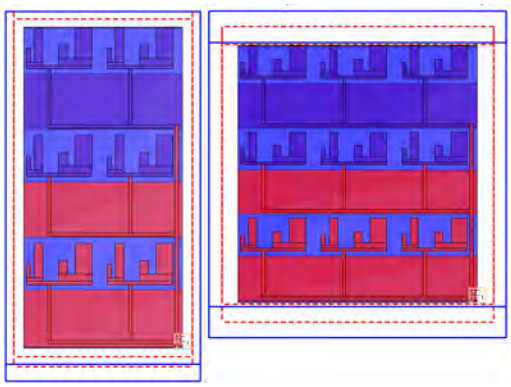

Figure 5.9: Two Dimensional Antenna Array

it is explicit that overall reflection coefficient is improved with increase in spacing d and number of elements, n.

5.2.2 Two Dimensional

In two dimensional antenna arrays, elements are connected in two dimensions. One of the designed two dimensional arrays, is shown in Figure 5.9. Now, in this case, spacing between two rows, md becomes an important parameter to be looked at. Increasing md increases Narrow Banding but reflection coefficient also improves. Narrow-banding is increased more when n is increased. Microstrip feeds are near patches in multidimensional arrays. So as they also affect the radiation.

5.3 Integrated Antenna Study

5.3.1 General Description

For a microwave engineer, an active antenna is an active microwave circuit in which the output or input port is free space instead of a conventional 50 Ω interface. For an antenna designer, Active antenna is an antenna that possesses built-in signal-and wave-processing capabilities such as mixing and amplification. In simple words an active antenna can provide certain circuit functions such as resonance, filtering, and duplexing, in addition to its original role as a radiating element.

5.3.2 Advantages

There are several advantages of AIAs. Some of these are as follows:

a. AIAs are attractive for millimeter-wave systems as following problems can be mitigated[85, 94]:

   (1) Transmission-line loss at higher frequencies

   (2) Limited source power

   (3) Reduced antenna efficiency

   (4) Lack of high-performance phase shifters

b. An AIA improves SNR of the receiver

c. these can be designed with higher realized gain and wider gain bandwidth than their passive counterparts

d. AIAs reduce the circuit area on a PCB

e. It can be easily integrated on MMIC

f. For Frequency doubling[95, 96]

5.3.3 Types of AIA

Many types of AIAs are designed till date. Some of them are following:

a. LNA integrated antenna[86]

b. Mixer integrated antenna[87, 88]

c. Oscillator active antenna[85, 89]

d. Active Integrated Antenna with Negative Resistance Transistor Oscillator[90]

e. Active Integrated Antenna including Nonlinear Model of FET Transistor[91]

f. High efficiency power amplifier antenna[92]

g. Beam-steering and switching antennas[93]

h. Power combining[93]

i. Retro-directive arrays[93]

j. AIA transceiver using Schottky diode mixer and inverted patch antenna[93]

k. Integrated active circulator antenna[93, 94]

l. Modulator / Demodulator integrated antenna[95]

m. Active Circulator Integrated Antenna[96]

5.3.4 Literature Survey

Previously published work

All the previously available work in the literature is explained in brief as follows. Chang et al. provide a review of the active integrated antenna (AIA) technologies. After a brief introduction on the definition and some historical remarks, the paper concentrates on the research effort on the past decades or so [85]. The AIAs are reviewed in its various functions. First, an oscillator-type AIA is presented, followed

by very interesting aspects of coupled oscillator arrays for phase control. Use of an AIA concept for efficient RF front end is described with examples on high-power amplifier AIAs. Next, a phase-conjugation based retro directive array is reviewed. Finally, AIA systems for receiving, transmitting, and duplexing are reviewed. In the work of Ismail et al., A patch antenna integrated, with two Low Noise Amplifiers (LNA) is implemented to act as an Image Reject Mixer (IRM) [86]. The low noise active antenna system transforms a received radio frequency signal into two signals, which are out-of phase to each other. The image signals can be cancelled by the IRM. The antenna, LNAs, mixers and local oscillator (LO) are integrated into a single Active Integrated Antenna (AIA) module. An external IF 90^o hybrid coupler is required in the IRM. The advantages of the LNA active antenna mixer system are low noise, image signal rejection, low cost and simple circuitry of front-end, and improved receiver sensitivity. In the work of Rahim et al., Active integrated antenna with image reject mixer (AIA with IRM) operating at license less frequency of 2.4 GHz and intermediate frequency (IF) of 50 MHz is proposed [87]. In this work, IRM is integrated with Microstrip patch antenna on the similar substrate to attain size, weight and cost reduction. The suitable substrate that serves as the common platform for all integral components is FR-4 with dielectric constant of 4.7 and thickness of 1.6mm. This AIA with IRM employs a different phase manipulation approach from the previous research in which the RF signal from the antenna is initially fed to 1800 rat race coupler instead of a 900 coupler. Practically, this system is able to achieve image suppression with an isolation of approximately 20 dB between image and desired frequency with 7 dBm LO drive at 2.35 GHz. The integral components of AIA with IRM consist of 2-elements Microstrip rectangular patch antenna, singly balanced schottky diode mixers, low pass filter, branch-line 900 hybrid coupler, lumped element 900 coupler and 1800 rat race coupler. Gupta et al., describe the behavior of a compact two-port integrated mixer active antenna element with low cross polarization, high two-port circuit isolation, and good mixer detection sensitivity [88]. Using this element as an elemental building block, a self-

tracking antenna array has been realized which uses an in-band carrier signal for self calibration. The array is relatively insensitive to absolute carrier power level and is capable of tracking incoming signals over $\pm 80^o$. By minor alteration of the antenna topology, a minimum complexity variant of a heterodyne retro directive array has been demonstrated over a $\pm 40^o$ retransmission angle. Finally, the use of the antenna in conjunction with an injection-locked voltage-controlled oscillator (VCO) is included in order to demonstrate $\pm 35^o$ phase-shifter less beam steering. A diamond-shaped Microstrip ring patch, as a radiator of an oscillator type active antenna, is proposed for easier impedance matching, smaller patch size, and circular polarization in the work of Yun [89]. The active antenna has been built and measured. The fabricated antenna including the active circuitry has a size about 65% of that using a regular-size square Microstrip antenna. Test results show potential possibilities for use as a transmitter of an RFID reader around 915 MHz. The design of an active integrated antenna with negative resistance transistor oscillator has been described in the work of Bonefaeie et al[90]. Simple but reasonably accurate analysis of oscillation start-up and steady state operating frequency prediction is presented. The active antenna prototype was manufactured and its operating frequency, EIRP and radiation patterns were measured. Two of these antennas were integrated in active arrays coupled in E- and H-planes. The inter-element distance in the arrays was optimized to obtain in phase operation and mutual injection locking. Very good power combining efficiency was measured and beam scanning capabilities were demonstrated for both arrays. In the work of Zhang et al., a non-linear circuit model of FET has been incorporated into the finite difference time domain (FDTD) method, when microwave active antennas are analyzed [91]. The FET operating in Class A mode is biased and its non-linear properties (second harmonics) are investigated. The algorithm and the simulation results are useful in the development of high power integrated active antennas modules. A broad band high-efficiency circularly polarized (CP) AIA is presented in the work of Quin et al[92]. A broad band CP active array at 2 GHz has been developed and

used in a RF front end system. Active integrated antennas (AIAs) provide a new paradigm for designing modern microwave and millimeter-wave architecture with desirable features such as compactness, light weight, low cost, low profile, minimum power consumption, and multiple functionality [93]. This work also reviews recent research and development related to this emerging technology with emphasis on its applications in high-efficiency radio-frequency (RF) front-end, millimeter-wave power combining, beam steering, and retro directive arrays, as well as wireless sensors. Optical controlling techniques for AIAs are also described. In the work of Cryan et al., an active circulator is integrated with a quarter wave short-circuited Microstrip patch antenna to produce a fully duplexed transceiver with transmit and receive operation at the same frequency and with the same polarization [94]. The active circulator antenna is shown to have 14-dBi transmit gain and 7.4-dBi receive gain with transmit-receive isolation of 26.9 dB at 3.745 GHz. This active antenna has potential uses in both short-range communication and radar systems. A letter by Manimegalai et al., presents a novel frequency doubling active antenna, based on a PHEMT device, with BPSK modulation capability [95]. A dedicated nonlinear transistor characterization reveals the existence of two biasing regions, where the second harmonic could be generated with maximum level and phase opposition. Taking advantage of this issue, a low frequency data signal applied to the gate terminal may be used to create a BPSK modulated signal, centered at twice the carrier frequency. An adequate integration of this modulator in a dual-frequency and dual-polarization slot coupled patch, results in a compact and high performance solution. In the work of Gupta et al., the design of an integrated Microstrip shorted antenna using hybrid active circulator is presented to produce a fully duplexed transceiver with transmit and receive operation at the same frequency and with the same polarization [96]. This design is compatible with the MMIC technology since ferrite circulator needed for duplexer is avoided by a hybrid active circulator based on phase cancellation technique. This integrated active circulator antenna has potential uses in both short-range communication systems and radar systems. Arrays of these

elements could overcome the power handling problems that limit the performance of current active circulators. In the work of Yee, Maxwells equations are replaced by a set of finite difference equations [97]. It is shown that if one chooses the field points appropriately, the set of finite difference equations is applicable for a boundary condition involving perfectly conducting surfaces. An example is given of the scattering of an electromagnetic pulse by a perfectly conducting cylinder. In the work of Reddy et al., an improved extended finite-difference time-domain formulation for the analysis of active linear and nonlinear microwave circuits is presented [98]. Here, we have selected the current source approach and have tried to update all the electric-field components on the active sheet. Central-difference approximation has been used for the discretization of the resultant set of state equations. The equivalent circuit of the device has been treated as a zero-dimensional circuit with respect to the wave propagation. The results based on this formulation show good agreement with analytically obtained data for circuits like amplifiers and oscillators. In the work of Sui et al., extension of the finite-difference time-domain (FDTD) method to include distributed electromagnetic systems with lumped elements (a hybrid system) and voltage and current sources is presented [99]. FDTD equations that include nonlinear elements like diodes and transistors are derived. Calculation of driving-point impedance is described. Comparison of FDTD calculated results with analytical results for several two-dimensional transmission-line configurations illustrate the accuracy of the method. FDTD results for a transistor model and a diode are compared with SPICE calculations. The extended FDTD method should prove useful in the design and analysis of complicated distributed systems with various active, passive, linear and nonlinear lumped electrical components. In the work of Tsui et al., a methodology is presented for the rigorous electromagnetic analysis of pulse transmission through first-level interconnects [100]. The methodology combines a full-wave, vectorial, time-dependent Maxwells equations solver with SPICE circuit models for the nonlinear drivers, to facilitate the accurate modeling of the electromagnetic phenomena occurring at the chip-to-package interface.

Comparisons of the results obtained using this method with others calculated using SPICE simulations are used to validate the method and demonstrate its application in the electromagnetic modeling of high-speed packaging structures. In the work done by May et al., most existing computer-aided circuit design tools are limited when digital clock speeds exceed several hundred MHz's [101]. These tools may not deal effectively with the physics of UHF and microwave electromagnetic wave energy transport along metal surfaces such as ground planes or in the air away from metal paths that are common at or above this frequency range. In this paper, we discuss full-wave modeling of electronic circuits in three dimensions using the finite-difference time-domain (FDTD) solution of Maxwells equations. Parameters such as strip line complex line impedance, propagation constant, capacitance per unit length and inductance per unit length can be easily computed as a function of frequency. We also discuss FD-TD Maxwells equations computational modeling of lumped-circuit loads and sources in 3-D, including resistors and resistive voltage sources, capacitors, inductors, diodes, and transistors. We believe that this approach will be useful in simulating the large-signal behavior of very high-speed nonlinear analog and digital devices in the context of the full-wave time-dependent electromagnetic field. In the work presented by Durney et al., Previous extension of the finite-difference time domain (FDTD) method to include lumped-circuit elements is further extended to model lumped-element circuits connected across multiple FDTD cells [102]. This formulation is needed to model many kinds of circuits, like those with a transistor or other active device connected across a transmission line with more than one dielectric. The FDTD analysis of a shielded suspended Microstrip transmission line excited by a current source in parallel with a resistance illustrates the usefulness of the formulation. In the work of Thomas et al., a general approach for including lumped circuit elements in a finite difference, time domain (FDTD) solution of Maxwells equations is presented [103]. The methodology allows the direct access to SPICE to model the lumped circuits, while the full 3-Dimensional solution to Maxwells equations provides the crosstalk and dispersive properties of the

microstrips and striplines in the circuit. In the work done by Kuo et al., the FDTD method is extended to analyze a microwave amplifier [104]. This amplifier includes matching circuits, DC bias circuits, and an active device. Equivalent current sources are used to model the active element. With the small signal model of the active element, the FDTD full-wave simulations show good agreement with measured results. In the work done by Toland et al., the FDTD algorithm is extended to perform a patches theoretical analysis of a two-element active antenna [105]. A description is given of the procedures that were used to produce a stable large signal simulation of the active, nonlinear circuit. Some results are given and a comparison is made with measured data. In the work presented by Thomas et al., Coupled FDTD-SPICE simulations are performed for an active antenna problem [106]. The results are comparable to previously published results using FDTD in conjunction with special integration techniques for the nonlinear elements. Some differences occur, and better agreement with experiment is batches served for our newer approach. The main advantages are that all of the SPICE device models are directly available for FDTD modeling and the efficient SPICE integration schemes can be used directly. No user intervention is required for either the device models or the integration schemes. In the work of Toland et al., the FDTD method is extended to include nonlinear active regions embedded in distributed circuits [107]. The procedures necessary to produce a stable algorithm are described, and a single device cavity oscillator is simulated with this method. A letter presented by Kuo et al., describes a voltage-source-based formulation of the extended finite-difference time-domain algorithm for the purpose of modeling microwave devices [108]. The device-wave interaction is fully characterized by replacing the lumped devices with equivalent voltage sources in the device region, which in turn generate electromagnetic fields according to Faradays law. This formulation is applied to the analysis of a typical microwave amplifier, which includes a three-terminal active MESFET device. Simulation results are in good agreement with measured data. In a work done by Djordjevic et al., Linear-lumped circuits containing capacitors and/or inductors are described by differential

equations [109]. In computer-aided circuit analysis, these equations are discretized in time, thus being reduced to approximate formulas involving samples of voltages and currents. It is shown that these relations can be interpreted as exact equations for networks containing transmission lines. Hence, some features of the approximate formulas gain a clear physical interpretation. In particular, convergence and energy balance properties of the formulas become obvious, confirming advantages of the trapezoidal rule over all other formulas. In the work done by Sheen et al., a direct three-dimensional finite-difference time-domain (FDTD) method is applied to the full-wave analysis of various Microstrip structures [110]. The method is shown to be an efficient tool for modeling complicated Microstrip circuit components as well as Microstrip antennas. From the time-domain results, the input impedance of a line-fed rectangular patch antenna and the frequency-dependent scattering parameters of a low-pass filter and a branch line coupler are calculated. These circuits are fabricated and the measurements are compared with the FDTD results and shown to be in good agreement. In the work of Haung et al., nonlinear analyses of MESFET oscillator in free-running and injection-locked states are studied based on the Volterra series method and stability analysis [111]. The approach shown is capable of quantitatively analyzing the injection locking performance of oscillator using three-terminal devices in the fundamental mode of operation. Both the transmission-type and reflection-type injection locked oscillators (ILO) are simulated and experimentally verified. In the work done by Zhao and Raisanen, a simple, efficient, and unified source excitation scheme for the finite-difference time-domain (FDTD) analysis of both waveguides and Microstrip circuits is developed and validated [112]. In this scheme, by moving the source plane several cells inside the terminal plane and adding the excitation wave as an extra term in the FDTD equation, the interaction between the excitation and reflected waves are totally separated in time domain. Hence, for both waveguide and Microstrip discontinuities, absorbing boundary conditions can be applied on the terminal plane directly. In particular, for Microstrip circuits, our scheme does not induce any source distortions when a simplified field distribution

is used as the excitation. Consequently, the terminal plane can be moved very close to the discontinuity and thus significant computational savings are achieved. In addition, for Microstrip systems, the validity and efficiency of the Mei's simplified field distribution are evaluated and confirmed for the first time.

5.4 Conclusion of the Chapter

Design and analysis of Revised Cantor Geometry based Fractal Antenna, on substrate with high dielectric constant, is explained in this chapter. In addition to that fractal antenna array designing is presented as an extension of the current work. Finally, study of integrated antenna is presented.

Chapter 6

Conclusion

In this research work, revised cantor geometry is proposed for antenna design, which produces more than 5 resonances in second iteration only. The three dimensional Finite Difference Time Domain (3D-FDTD) Method is used for analyzing the reflection coefficient of the antenna. A code is written based on FDTD in MATLAB. Reflection Coefficient is validated in comparison with FIT based CST Studio suite. A revised cantor geometry based multiband antenna is proposed. This antenna is designed using fractal technique. The proposed antenna is covering frequency bands in several wireless applications. It covers GSM, PCS, DCS, UMTS, ZigBee, WLAN 2.4 GHz and 5.8 GHz applications and several Ultra Wideband (UWB) applications. The effect on the reflection coefficient with the variation in length of the fingers of the antenna is presented with all the designs simulated in MATLAB. Based on the observations of length variation of fingers, two low profile multiband antenna designs, with various applications, are presented.

In summary, major novelties of this work are as follows:

a. Proposed Revised Cantor Geometry

b. Antenna Return Loss Validation of FDTD based MATLAB code in comparison to commercially available tools

c. Observational analysis of Antenna Fingers and conclusions based on heights

of the fingers

d. Proposed Ground-Feed Algorithm

e. Proposed Multiband Fractal Antenna design

f. Measurement of proposed antenna and perfect matching of measurement results with analyzed results

g. Specific Absorption Rate (SAR) analysis

h. Proposed SAR reduction techniques

Chapter 7

Future Work

SAR calculations can be done with Mobile circuitry. Fabrication of the antenna can be done with Mobile/Tablet prototype. Measurement of SAR can be done.

Appendix A

Basic Electromagnetics

Analysis of radiation can be achieved by analyzing electromagnetic behavior of the Microstrip structures. Thus, a brief and important discussion on basic electromagnetics is presented here [1]. This provides basic understanding of electromagnetic parameters which are used in the later chapters.

A.1 Del, Gradient, Divergence and Curl

The Del operator is represented as

$$\vec{\nabla} = \frac{\partial}{\partial x}\hat{i} + \frac{\partial}{\partial y}\hat{j} + \frac{\partial}{\partial z}\hat{k} \tag{A.1}$$

Here, $\vec{\nabla}$ shows that it is a vector quantity. It represents the three dimensional partial spatial differentiation vectors. This operator has noticeable significance in the field of electromagnetics.

A.1.1 The Gradient Operator

When Del operator is applied on any scalar field, it is called as Gradient. Let T be any scalar field and apply Del operator on it as follows

$$\vec{\nabla}T = \left(\frac{\partial}{\partial x}\hat{i} + \frac{\partial}{\partial y}\hat{j} + \frac{\partial}{\partial z}\hat{k}\right)T \tag{A.2}$$

Or equivalently,

$$\vec{\nabla}T = \left(\frac{\partial T}{\partial x}\hat{i} + \frac{\partial T}{\partial y}\hat{j} + \frac{\partial T}{\partial z}\hat{k}\right) \tag{A.3}$$

Here, $\vec{\nabla}T$ represents the Gradient of scalar field T. though it is applied on scalar field but it produces a vector. Thus ∇T is a vector quantity whose direction is in the maximum rate of change of the scalar field T.

A.1.2 The Divergence Operator

When the Del operator is applied with a dot product on a vector field, it is known as Divergence operator. Suppose $\vec{V}$ is a vector field given as

$$\vec{V} = V_x\hat{i} + V_y\hat{j} + V_z\hat{k} \tag{A.4}$$

And dot product of $\vec{V}$ is done with Del operator as follows

$$\vec{\nabla}\cdot\vec{V} = \left(\frac{\partial T}{\partial x}\hat{i} + \frac{\partial T}{\partial y}\hat{j} + \frac{\partial T}{\partial z}\hat{k}\right)\cdot\left(V_x\hat{i} + V_y\hat{j} + V_z\hat{k}\right) \tag{A.5}$$

Here, $\nabla\cdot\vec{V}$ represents the Divergence of vector field $\vec{V}$. The divergence shows the net outward flow of the vector field from a volume. It is explicitly interpreted in the figure 3.1.

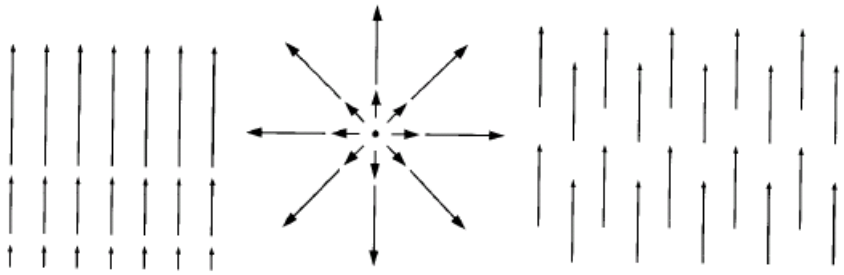

(a) Positive (b) Positive (c) Zero

Figure A.1: The Divergence

A.1.3 The Curl Operator

When the vector cross product of Del operator is applied on a vector field, it is known as Curl operator. Let $\vec{V}$ be a vector field and apply cross product with Del operator, on it as follows

$$\vec{\nabla} \times \vec{V} = \begin{vmatrix} \hat{i} & \hat{j} & \hat{k} \\ \frac{\partial}{\partial x} & \frac{\partial}{\partial y} & \frac{\partial}{\partial z} \\ A_x & A_y & A_z \end{vmatrix} \tag{A.6}$$

Here, $\vec{\nabla} \times \vec{V}$ is known as the curl of vector field $\vec{V}$. The curl of a vector, as its name

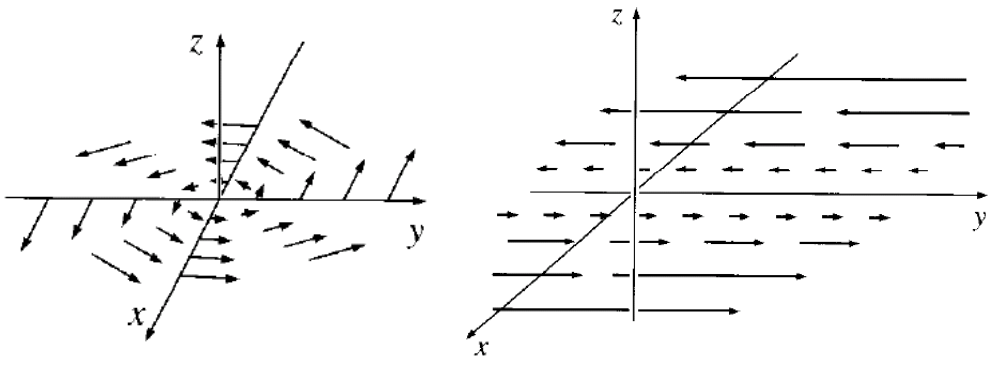

(a) Positive (b) Positive

Figure A.2: The Curl

suggests, shows how much a vector curls around the point in question. Curl can be more easily interpreted by the figure 3.2, which shows the rotation of a vector field. Direction of the curl is obtained by right hand thumb rule.

A.2 Maxwell's Equations

Maxwell's equations are well known in electromagnetics. These equations are used to determine the electromagnetic behavior of any matter or any object[1]. Maxwell's equations are individually known as Faraday's law, Ampere's law, Gauss's electric and magnetic laws. These equations are represented in both time domain and frequency domain. Here, only time domain integral and differential equations are presented.

Integral Form

Maxwell's equations in integral form[5, 6], are given as

a. Faraday's Law

$$\int_{\partial A} \vec{E} \cdot \vec{ds} = \int_{A} \frac{\partial \vec{B}}{\partial t} \cdot \vec{dA} \tag{A.7}$$

Where, A denotes any open surface, ∂A is its boundary (a closed curve), $\vec{dA}$ and $\vec{ds}$ are the vectorial area and line element, respectively.

b. Ampere's Law

$$\int_{\partial A} \vec{H} \cdot \vec{ds} = \int_{A} \left(\frac{\partial \vec{D}}{\partial t} + \vec{J} \right) \cdot \vec{dA} \tag{A.8}$$

Where, A denotes any open surface, ∂A is its boundary (a closed curve), $\vec{dA}$ and $\vec{ds}$ are the vectorial area and line element, respectively.

c. Gauss's Law of Electricity

$$\int_{\partial V} \vec{D} \cdot \vec{dA} = \int_{V} \rho dv \tag{A.9}$$

Where, V denotes any open volume, ∂V is its boundary (a closed surface), dv and $d\vec{A}$ are the small volume and vectorial area element, respectively.

d. Gauss's Law of Magnetism

$$\int_{\partial V} \vec{B} \cdot d\vec{A} = 0 \tag{A.10}$$

Where, V denotes any open volume, ∂V is its boundary (a closed surface), dv and $d\vec{A}$ are the small volume and vectorial area element, respectively.

These equations are directly discretized in FIT.

Differential Form

These equations emphasize the divergence and curl of electric field, E (or electric field displacement D) and magnetic field, H (or magnetic flux density B)[7].

Normal Form

The Maxwell's equations in differential form are given as

a. Ampere's law

$$\nabla \times \vec{H} = \frac{\partial \vec{D}}{\partial t} + \vec{J} \tag{A.11}$$

b. Faraday's law

$$\nabla \times \vec{E} = -\frac{\partial \vec{B}}{\partial t} + \vec{M} \tag{A.12}$$

c. Gauss's electric law

$$\nabla \cdot \vec{D} = \rho_e \tag{A.13}$$

d. Gauss's magnetic law

$$\nabla \cdot \vec{B} = \rho_m \tag{A.14}$$

In this form, these equations reinforce that electric field can be produced either by charges, ρ or by the changing magnetic fields, $\frac{\partial B}{\partial t}$, and magnetic field can be produced by either current, J or the changing electric field, $\frac{\partial E}{\partial t}$.
Here, E is electric field strength, D is electric field displacement, H is magnetic field strength, B is magnetic flux density, J is electric current density, M is magnetic current density, ρ_e is electric charge density, ρ_m is magnetic charge density and ∇ is the spatial del operator.

Special Form of Differential Form

To have the impact of material parameters in the FDTD approach, constitutive relations of electromagnetics are used. The constitutive relations are those which give relationship between various electromagnetic parameters in accordance with the material parameters. The constitutive relations are given as

$$\vec{D} = \epsilon \vec{E} \tag{A.15}$$

Here, D is electric field displacement, ϵ is material permittivity and E is electric field strength.

$$\vec{B} = \mu \vec{H} \tag{A.16}$$

Here, B is magnetic flux density, μ is material permeability and H is magnetic field strength.

$$\vec{J} = \vec{J}_c + \vec{J}_i \tag{A.17}$$

Here, J is electric current density, J_c is conduction electric current density, J_i is impressed electric current density.

$$\vec{J}_c = \sigma^e \vec{E} \tag{A.18}$$

Here, σ^e is electric conductivity of the material.

$$\vec{M} = \vec{M}_c + \vec{M}_i \tag{A.19}$$

Here, M is magnetic current density, M_c is conduction magnetic current density, M_i is impressed magnetic current density.

$$\vec{M}_c = \sigma^m \vec{H} \tag{A.20}$$

Here, σ^m is magnetic conductivity of the material.

By using these constitutive relations in the Maxwell's equations in differential form, the modified Maxwell's equations are obtained.

a. Ampere's law

$$\nabla \times \vec{H} = \epsilon \frac{\partial \vec{E}}{\partial t} + \sigma^e \vec{E} + \vec{J}_i \tag{A.21}$$

b. Faraday's law

$$\nabla \times \vec{E} = -\mu \frac{\partial \vec{H}}{\partial t} + \sigma^m \vec{E} + \vec{M}_i \tag{A.22}$$

c. Gauss's electric law

$$\nabla \cdot \vec{E} = \frac{\rho_e}{\epsilon} \tag{A.23}$$

d. Gauss's magnetic law

$$\nabla \cdot \vec{H} = \frac{\rho_m}{\mu} \tag{A.24}$$

These equations are directly discretized in FDTD method.

Appendix B

Numerical Techniques for Antenna Design

Computational Electromagnetics is a vast domain of mathematics in computers. For computer based simulation of high frequency structures, there are many numerical methods developed, like Finite Integration Technique (FIT), Finite Difference Time Domain Method (FDTD), Method of Moments (MoM) and Finite Element Method (FEM). Two of these techniques mainly, FIT and FDTD, are explained in detail, in this chapter.

B.1 Finite Integration Technique

The finite integration technique also known as, FIT, was developed by Thomas A. Weiland in 1977. It is a numerical discretization approach used for solving Maxwell's equations in their integral form [5, 6]. In other words, it establishes a discrete reformulation of Maxwell's equations in their integral form, suitable for computers. It allows simulation of real-world electromagnetic field problems with complex geometries. The final updating matrix equations of the discretized fields are used for efficient numerical simulations. In addition, the basic algebraic properties of this discrete electromagnetic field theory allow to analytically and to algebraically prove

conservation properties with respect to energy and charge of the discrete formulation and gives an explanation of the stability properties of numerical formulations in the time domain. The Maxwell's equations in their integral form are given as (recall from chapter 3)

a. Faraday's Law

$$\int_{\partial A} \vec{E} \cdot \vec{ds} = \int_{A} \frac{\partial \vec{B}}{\partial t} \cdot \vec{dA} \tag{B.1}$$

Where, A denotes any open surface, ∂A is its boundary (a closed curve), $\vec{dA}$ and $\vec{ds}$ are the vectorial area and line element, respectively.

b. Ampere's Law

$$\int_{\partial A} \vec{H} \cdot \vec{ds} = \int_{A} \left(\frac{\partial \vec{D}}{\partial t} + \vec{J} \right) \cdot \vec{dA} \tag{B.2}$$

Where, A denotes any open surface, ∂A is its boundary (a closed curve), $\vec{dA}$ and $\vec{ds}$ are the vectorial area and line element, respectively.

c. Gauss's Law of Electricity

$$\int_{\partial V} \vec{D} \cdot \vec{dA} = \int_{V} \rho dv \tag{B.3}$$

Where, V denotes any open volume, ∂V is its boundary (a closed surface), dv and $\vec{dA}$ are the small volume and vectorial area element, respectively.

d. Gauss's Law of Magnetism

$$\int_{\partial V} \vec{B} \cdot \vec{dA} = 0 \tag{B.4}$$

Where, V denotes any open volume, ∂V is its boundary (a closed surface), dv and $\vec{dA}$ are the small volume and vectorial area element, respectively.

FIT usually represents an open boundary problem to a simply connected and bounded space region $\Omega \in \Re^3$. The decomposition of the computational domain Ω

into a (locally) finite number of simplified cells V_i is done such as tetra or hexahedra, under the premise that all cells have to fit exactly to each other. The intersection of two different cells is either empty or it must be a two-dimensional polygon, a one-dimensional edge shared by both cells or a point.

Consider the hexahedral approach in which Ω is considered to be brick shaped. The decomposition is given with a with a tensor product grid for Cartesian coordinates such that we get a cell complex G as

$$G = \left\{ V_{i,j,k} \in \Re^3 | V_{i,j,k} = [x_i, x_{i+1}] \otimes [y_j, y_{j+1}] \otimes [z_k, z_{k+1}] \right\} \tag{B.5}$$

Here, i = 1,2,. . . , N_x, j = 1,2,. . . , N_y, k = 1,2,. . . , N_z. The total number of mesh points is $N_p = (N_x + 1)\times(N_y + 1)\times(N_z + 1)$, for $N_x \times N_y \times N_z$ mesh cells.

The grid discretization is done as shown in the figure 5.1. The whole geometry is divided into small volumes, which are called as Yee cells.

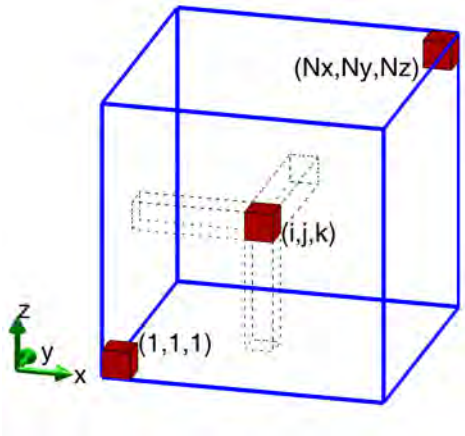

Figure B.1: Grid Discretization

Now, consider the Maxwell's first equation also known as faraday's law, which is given as

$$\int_{\partial A} \vec{E} \cdot \vec{ds} = \int_A \frac{\partial \vec{B}}{\partial t} \cdot \vec{dA} \tag{B.6}$$

Where, A denotes any open surface, ∂A is its boundary (a closed curve), $d\vec{A}$ and $\vec{ds}$ are the vectorial area and line element, respectively.

It can be observed that left side of the equation is showing the rotation of the electric field over boundary edges of an open surface ∂A. This can be expressed in terms of electromotive force, which causes the electric field, as is explicit in the figure 5.2.

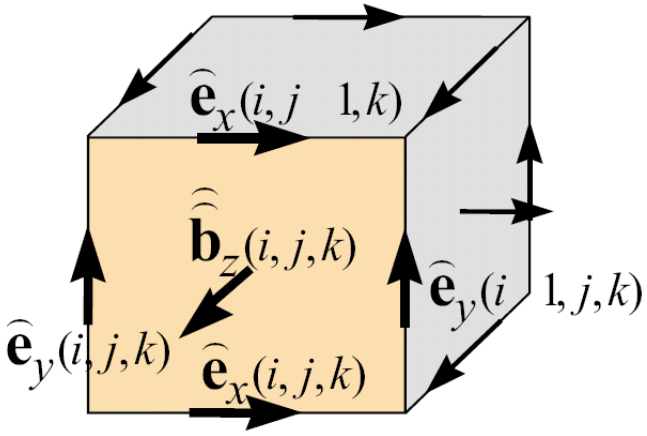

Figure B.2: Electromotive Force

Thus faraday's law can be equivalently represented for a facet $A(i, j, k)$ of V_n as the ordinary differential equation as

$$\widehat{e}_x(i, j, k) + \widehat{e}_y(i + 1, j, k) - \widehat{e}_x(i, j + 1, k) - \widehat{e}_y(i, j, k) = -\frac{d}{dt}\widehat{\widehat{b}}_z(i, j, k) \tag{B.7}$$

Where the scalar value $\widehat{e}_x(i, j, k)$ can be given as

$$\widehat{e}_x(i, j, k) = \int_{(x_i, y_j, z_k)}^{(x_{i+1}, y_j, z_k)} \vec{E} \cdot \vec{ds} \tag{B.8}$$

$e_x(i, j, k)$ is the emf along one edge of the surface $A(i, j, k)$ representing the exact value of the integral over the electric field along this edge. The scalar value $b_z(i, j, k)$ is given as

$$\widehat{\widehat{b}}_z(i,j,k) = \int_{A_z(i,j,k)} \vec{B} \cdot d\vec{A} \tag{B.9}$$

This is magnetic flux i.e., the integral value over the magnetic flux density through the cell facet $A_z(i,j,k)$. It has to be noted that the orientation of the cell edges will have influence on the signs within equations given before. The integral formulation of Faraday's law is valid for each single facet $A(i,j,k)$ of G and the discrete approach naturally extends to larger facet areas $A = \bigcup A(i,j,k)$ due to the relation

$$\sum \oint_A (i,j,k) = \oint_A \tag{B.10}$$

The same result will hold for surface integrals also. Now, for vector representation, assume a lexicographical ordering of the electric voltages $e(i,j,k)$ and of the magnetic facet fluxes $b(i,j,k)$ over the whole cell complex G and their assembly into column vectors.

$$\widehat{e} = (\widehat{e}_{x,n}|\widehat{e}_{y,n}|\widehat{e}_{z,n})^T_{n=1,\ldots,N_p} \in \Re^{3N_p} \tag{B.11}$$

$$\widehat{\widehat{b}} = \left(\widehat{\widehat{b}}_{x,n}|\widehat{\widehat{b}}_{y,n}|\widehat{\widehat{b}}_{z,n}\right)^T_{n=1,\ldots,N_p} \in \Re^{3N_p} \tag{B.12}$$

The integral equations of all grid cell surfaces of the complex G can be collected in a matrix form as

$$\underbrace{\begin{bmatrix} & \ldots & \ldots & \ldots & & \\ 1 & \ldots & 1 & \ldots & -1 \ldots & -1 \\ & \ldots & \ldots & \ldots & & \end{bmatrix}}_{C} \underbrace{\begin{bmatrix} \widehat{e}_{n_1} \\ \vdots \\ \widehat{e}_{n_2} \\ \vdots \\ \widehat{e}_{n_3} \\ \vdots \\ \widehat{e}_{n_4} \end{bmatrix}}_{\widehat{e}} = -\frac{d}{dt} \underbrace{\begin{bmatrix} \vdots \\ \widehat{\widehat{b}}_n \\ \vdots \end{bmatrix}}_{\widehat{\widehat{b}}} \tag{B.13}$$

C represents the discrete curl-operator on the grid G. Now, consider the Gauss's magnetic law in integral form

$$\int_{\partial V} \vec{B} \cdot d\vec{A} = 0 \tag{B.14}$$

Where, V denotes any open volume, ∂V is its boundary (a closed surface), dv and $d\vec{A}$ are the small volume and vectorial area element, respectively. Considered for a cell $V_{i,j,k}$ as shown in figure 5.3.

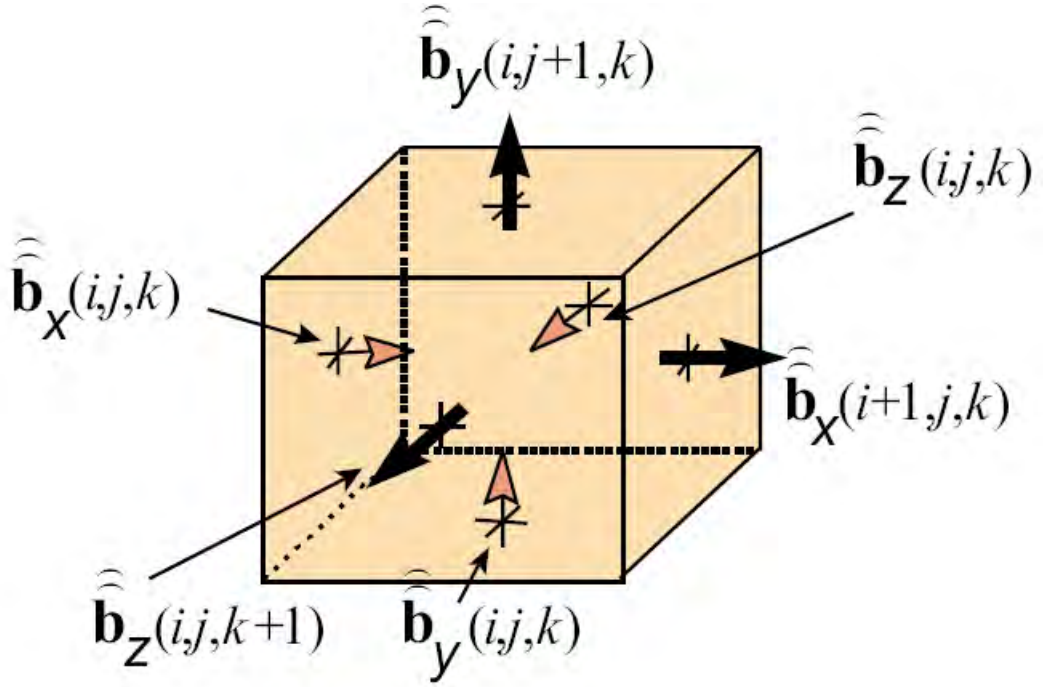

Figure B.3: Magnetic Flux Flow from a Cell $V_{i,j,k}$

Nonexistence of magnetic charges is assumed here. For the given brick volume, surface integral can be discretized as

$$-\hat{\hat{b}}_x(i,j,k)+\hat{\hat{b}}_x(i+1,j,k)-\hat{\hat{b}}_y(i,j,k)+\hat{\hat{b}}_y(i,j+1,k)-\hat{\hat{b}}_z(i,j,k)+\hat{\hat{b}}_z(i,j,k+1)=0 \tag{B.15}$$

Again this relation for a single cell can be expanded to the whole cell complex G, to obtain the matrix form.

$$\underbrace{\begin{bmatrix} & & \cdots & \cdots & & & \\ -1 & 1 & -1 & 1 & -1 & 1 & . \\ & & \cdots & \cdots & & & \end{bmatrix}}_{S} \underbrace{\begin{bmatrix} \vdots \\ \hat{\hat{b}}_{m_1} \\ \hat{\hat{b}}_{m_2} \\ \hat{\hat{b}}_{m_3} \\ \hat{\hat{b}}_{m_4} \\ \hat{\hat{b}}_{m_5} \\ \hat{\hat{b}}_{m_6} \\ \vdots \end{bmatrix}}_{\hat{\hat{b}}} = 0 \tag{B.16}$$

S represents the discrete divergence operator on the grid G. $S \in \Re^{N_p X 3N_p}$ only depends on the grid topology same as discrete curl operator C.
For the Cartesian tensor product grid G the dual grid $\widetilde{G}$ is defined by taking the foci of the cells of G as grid points for the mesh cells of $\widetilde{G}$. Then, take the cell barycenters as boundary vertices for definition of the dual grid cells of $\widetilde{G}$. It produces one to one relationship between both grids G and $\widetilde{G}$. It also produces one to one relationship between the cell edges of G cutting through the cell surfaces of $\widetilde{G}$ and vice versa.

Now, another two laws of Maxwell which are, Ampere's law and Gauss's electricity law given as

$$\int_{\partial A} \vec{H} \cdot \vec{ds} = \int_{A} \left(\frac{\partial \vec{D}}{\partial t} + \vec{J} \right) \cdot \vec{dA} \tag{B.17}$$

and

$$\int_{\partial V} \vec{D} \cdot \vec{dA} = \int_{V} \rho dv \tag{B.18}$$

can be discretized by using similar approach as used for Faraday's law and Gauss's magnetic law. Consider the following discretization approach as shown in figure 5.5.

Discretization can be performed for an arbitrary facet of a dual grid $\widetilde{G}$ cells in complete analogy to Faradays law by summing up the magnetic grid voltages. Gauss

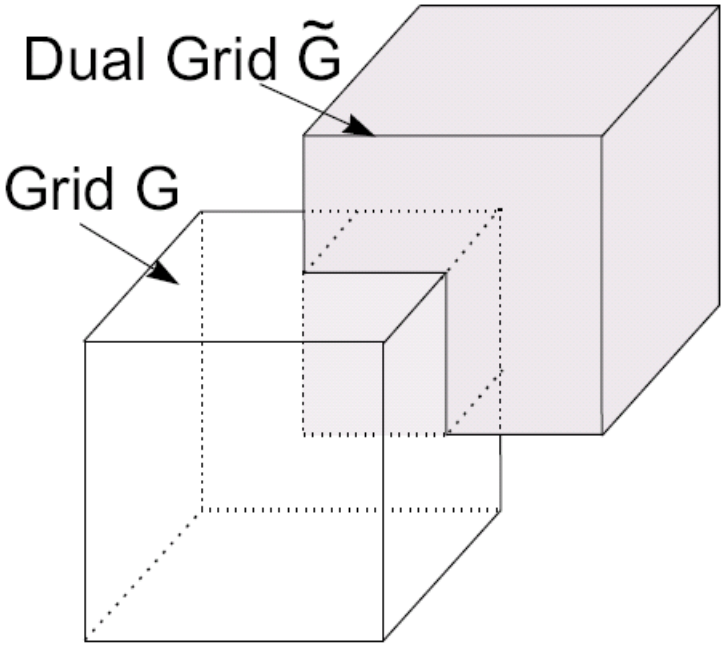

Figure B.4: Dual Grids, G and $\widetilde{G}$

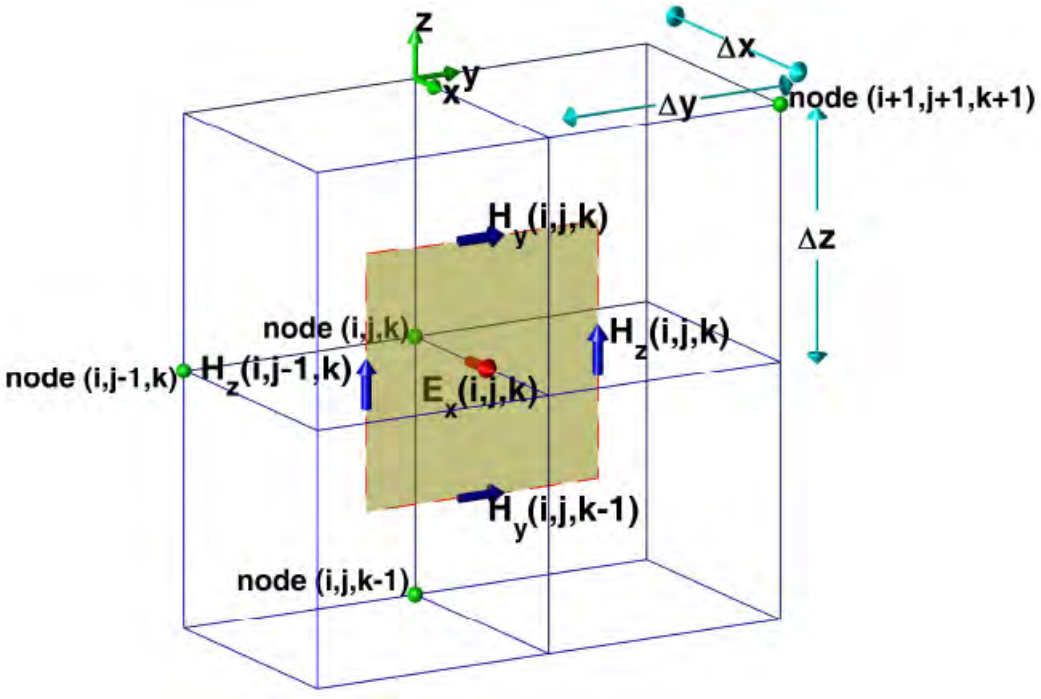

Figure B.5: Discretization for $\widetilde{G}$

law in integral form can also be discretized for the dual grid $\widetilde{G}$ cells same as Gauss's magnetic law. Both these discretization for the dual grid cell complex will result in matrix equations featuring the topological grid operators $\widetilde{C}$ for the dual discrete curl and $\widetilde{S}$ for the dual discrete divergence.

For the dual grid cell complex pair, the complete set of discrete matrix equations, the so-called Maxwell-Grid-Equations (MGE) are now given as

$$C\widehat{e} = -\frac{d}{dt}\widehat{\widehat{b}} \tag{B.19}$$

$$\widetilde{C}\widehat{h} = \frac{d}{dt}\widehat{\widehat{d}} + \widehat{\widehat{j}} \tag{B.20}$$

$$S\widehat{\widehat{b}} = 0 \tag{B.21}$$

$$\widetilde{S}\widehat{\widehat{d}} = q \tag{B.22}$$

So the final transformation can be seen as

$$\int_{\partial A} \vec{E} \cdot \vec{ds} = \int_{A} \frac{\partial \vec{B}}{\partial t} \cdot \vec{dA} \Leftrightarrow C\widehat{e} = -\frac{d}{dt}\widehat{\widehat{b}} \tag{B.23}$$

$$\int_{\partial A} \vec{H} \cdot \vec{ds} = \int_{A} \left(\frac{\partial \vec{D}}{\partial t} + \vec{J} \right) \cdot \vec{dA} \Leftrightarrow \widetilde{C}\widehat{h} = \frac{d}{dt}\widehat{\widehat{d}} + \widehat{\widehat{j}} \tag{B.24}$$

$$\int_{\partial V} \vec{D} \cdot \vec{dA} = \int_{V} \rho dv \Leftrightarrow S\widehat{\widehat{b}} = 0 \tag{B.25}$$

$$\int_{\partial V} \vec{B} \cdot \vec{dA} = 0 \Leftrightarrow \widetilde{S}\widehat{\widehat{d}} = q \tag{B.26}$$

The algebraic structure of the discrete material relations is independent of the method for the local field approximation and results in

$$\vec{D} = \epsilon\vec{E} + \vec{P} \Leftrightarrow \widehat{\widehat{d}} = M_\epsilon \widehat{e} + \widehat{\widehat{p}} \tag{B.27}$$

$$\vec{B} = \mu\vec{H} + \vec{M} \Leftrightarrow \widehat{\widehat{b}} = M_\mu \widehat{h} + \widehat{\widehat{m}} \tag{B.28}$$

$$\vec{J} = \sigma\vec{E} \Leftrightarrow \widehat{\widehat{j}} = M_\sigma \widehat{e} \tag{B.29}$$

$M_\epsilon$is the permittivity matrix, M_σ is the matrix of conductivities and M_μ is the matrix of permeability. $\widehat{\widehat{p}}$ and $\widehat{\widehat{m}}$ arise from permanent electric and magnetic polarizations respectively.

Time domain discretization of Maxwell's equations is done by using Finite Difference Time Domain (FDTD) approach and final updating matrix equations are obtained [7].

B.2 Finite Difference Time Domain

Finite difference time domain method, which is also known as FDTD, is a numerical method used for discretizing and solving Maxwell's equations in differential form. Kane Yee represented this method in 1966. It provides approximations for differential equations as finite differences [7]. It can handle composite geometries consisting of different kind of materials like dielectrics, frequency dependent nonlinear and anisotropic materials. It has various applications in elctromagnetics, among which major are implementation, design and simulation of Microstrip active structures like amplifiers and Microstrip passive structures like antenna as well [7].

It uses some of the basic difference equations for determining derivative of a function.

Forward difference formula is given as

$$f'(x) = \frac{f(x + \Delta x) - f(x)}{\Delta x} \tag{B.30}$$

and the first order central difference formula is given as

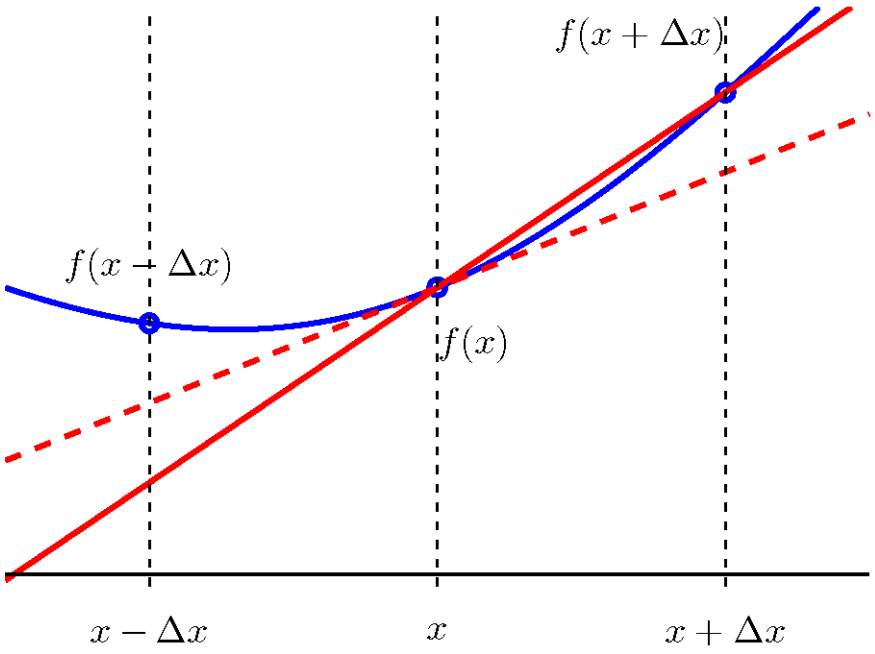

Figure B.6: Forward Difference

$$f'(x) = \frac{f(x + \Delta x) - f(x - \Delta x)}{2\Delta x}. \tag{B.31}$$

Yee represented a set of finite difference equations for the time dependent Maxwells Curl equations. These equations use the Forward Difference Method for determining the derivative of a function. Both, electric and magnetic fields, are sampled at discrete positions in time and space. Three dimensional geometry is divided into cells to form a grid structure. Grid discretization is done as shown in figure 5.8.

Electric field components are placed at the centers of edges of the Yee cells and oriented parallel to the respective edges. Magnetic field components are placed at

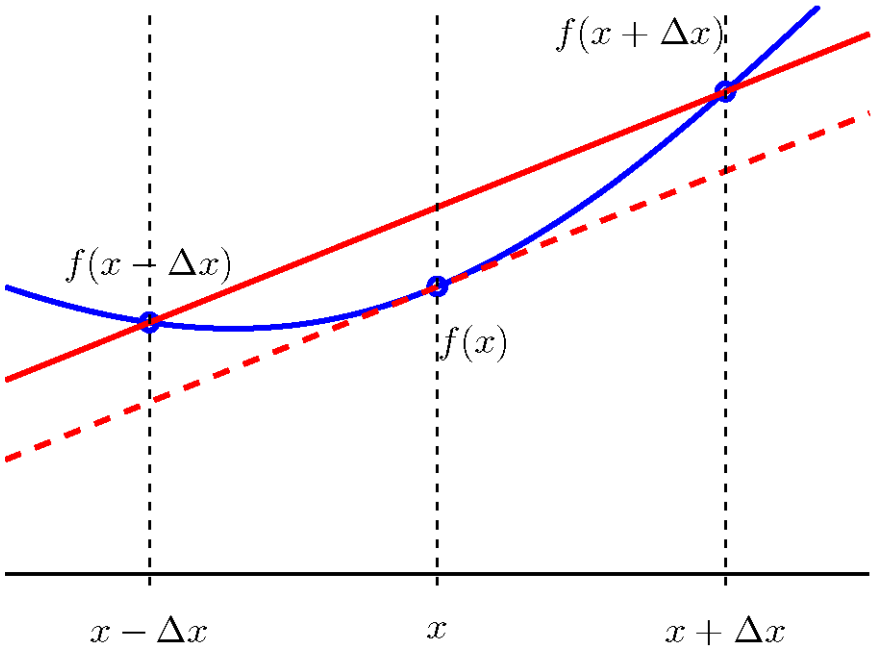

Figure B.7: Central Difference

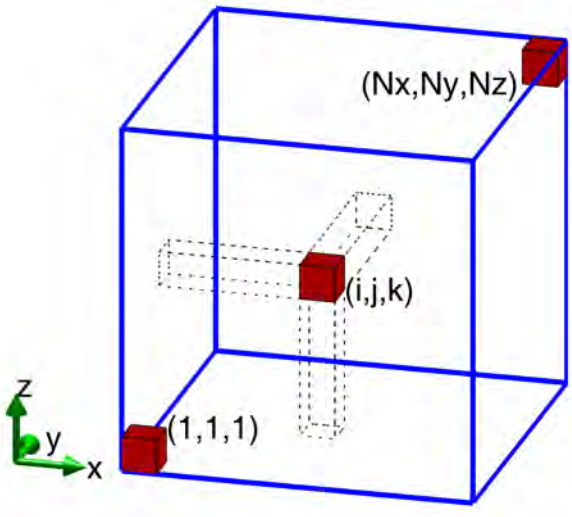

Figure B.8: Grid Discretization

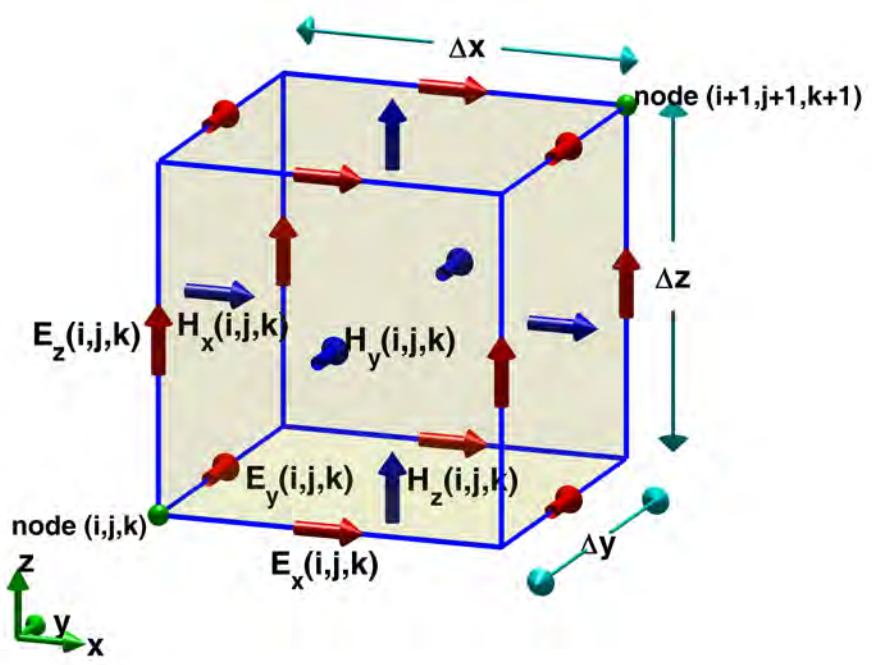

Figure B.9: Field Positions

the centers of the faces of the Yee cells and are oriented normal to the respective faces. The field positions according to the figure 5.9, are given as follows with respect to (1,1,1),

$$E_x(i,j,k) = ((i-0.5)\Delta x, (j-1)\Delta y, (k-1)\Delta z) \tag{B.32}$$

$$E_y(i,j,k) = ((i-1)\Delta x, (j-0.5)\Delta y, (k-1)\Delta z) \tag{B.33}$$

$$E_z(i,j,k) = ((i-1)\Delta x, (j-1)\Delta y, (k-0.5)\Delta z) \tag{B.34}$$

$$H_x(i,j,k) = ((i-1)\Delta x, (j-0.5)\Delta y, (k-0.5)\Delta z) \tag{B.35}$$

$$H_y(i,j,k) = ((i-0.5)\Delta x, (j-1)\Delta y, (k-0.5)\Delta z) \tag{B.36}$$

$$H_z(i,j,k) = ((i-0.5)\Delta x, (j-0.5)\Delta y, (k-1)\Delta z). \tag{B.37}$$

Material parameters are also considered accordingly. As presented in [7, 13], the electric fields are sampled at 0, Δt, 2Δt, 3Δt,..., nΔt, time positions (Integer time

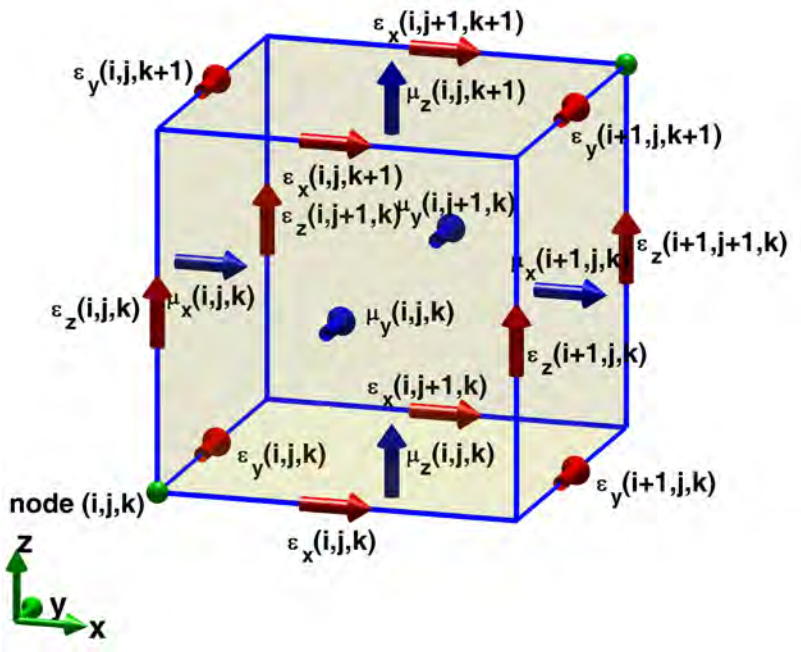

Figure B.10: Material Parameter Positions

steps) and the magnetic fields are sampled at (1/2)Δt, (1+1/2) Δt,..., (n+1/2)Δt, time positions according to the dual grid approach (Half integer time steps) and are offset from each other by (Δt/2). Time discretization is given by superscript while spatial discretization is given brackets attached with the respective components. Now, consider the Maxwell's curl equations as

$$\frac{\partial \vec{E}}{\partial t} = \frac{1}{\epsilon}\left[\nabla \times \vec{H} - \sigma^e \vec{E} - \vec{J}_i\right] \tag{B.38}$$

$$\frac{\partial \vec{H}}{\partial t} = \frac{1}{\mu}\left[-\nabla \times \vec{E} - \sigma^m \vec{H} - \vec{M}_i\right] \tag{B.39}$$

By using matrix form of the curl of a vector field, the curl of magnetic field H can be given as

$$\nabla \times \vec{H} = \hat{i}\left(\frac{\partial H_z}{\partial y} - \frac{\partial H_y}{\partial z}\right) - \hat{j}\left(\frac{\partial H_z}{\partial x} - \frac{\partial H_x}{\partial z}\right) + \hat{k}\left(\frac{\partial H_y}{\partial x} - \frac{\partial H_x}{\partial y}\right) \tag{B.40}$$

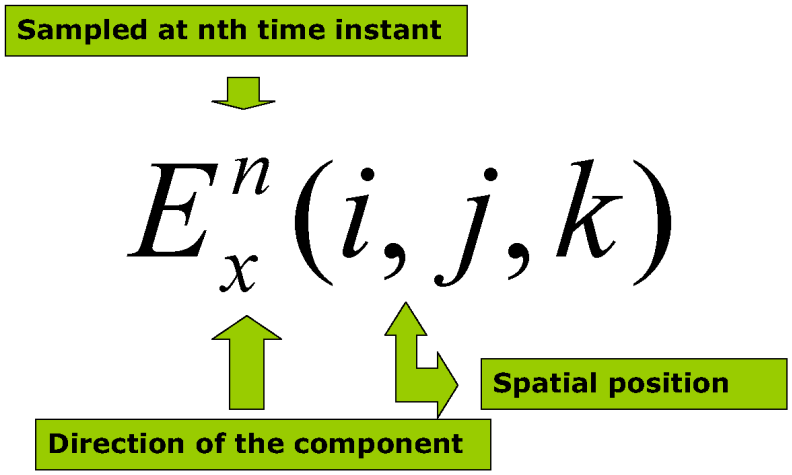

Figure B.11: Discretization Approach

and curl of electric field E can be given as

$$\nabla \times \vec{E} = \hat{i}\left(\frac{\partial E_z}{\partial y} - \frac{\partial E_y}{\partial z}\right) - \hat{j}\left(\frac{\partial E_z}{\partial x} - \frac{\partial E_x}{\partial z}\right) + \hat{k}\left(\frac{\partial E_y}{\partial x} - \frac{\partial E_x}{\partial y}\right) \tag{B.41}$$

By using these two equations, Maxwell's curl equations can be equivalently represented as follows, where the rate of change of the components of electric and magnetic fields in various directions, with respect to time is presented.

$$\frac{\partial \vec{E_x}}{\partial t} = \frac{1}{\epsilon_x}\left[\left(\frac{\partial H_z}{\partial y} - \frac{\partial H_y}{\partial z}\right) - \sigma_x^e \vec{E_x} - \vec{J_{ix}}\right] \tag{B.42}$$

$$\frac{\partial \vec{E_y}}{\partial t} = \frac{1}{\epsilon_y}\left[\left(\frac{\partial H_x}{\partial z} - \frac{\partial H_z}{\partial x}\right) - \sigma_y^e \vec{E_y} - \vec{J_{iy}}\right] \tag{B.43}$$

$$\frac{\partial \vec{E_z}}{\partial t} = \frac{1}{\epsilon_z}\left[\left(\frac{\partial H_y}{\partial x} - \frac{\partial H_x}{\partial y}\right) - \sigma_z^e \vec{E_z} - \vec{J_{iz}}\right] \tag{B.44}$$

$$\frac{\partial \vec{H_x}}{\partial t} = \frac{1}{\mu_x}\left[-\left(\frac{\partial E_z}{\partial y} - \frac{\partial E_y}{\partial z}\right) - \sigma_x^m \vec{H_x} - \vec{M_{ix}}\right] \tag{B.45}$$

$$\frac{\partial \vec{H_y}}{\partial t} = \frac{1}{\mu_y}\left[-\left(\frac{\partial E_x}{\partial z} - \frac{\partial E_z}{\partial x}\right) - \sigma_y^m \vec{H_y} - \vec{M_{iy}}\right] \tag{B.46}$$

$$\frac{\partial \vec{H}_z}{\partial t} = \frac{1}{\mu_z}\left[-\left(\frac{\partial E_y}{\partial x} - \frac{\partial E_x}{\partial y}\right) - \sigma_z^m \vec{H}_z - \vec{M}_{iz}\right] \tag{B.47}$$

Two necessary assumptions are taken into account as follows

a. Center point for x component of the Electric field is at (i, j, k) position.

b. Time instant $\left(n+\frac{1}{2}\right)\Delta$t being the center point in time.

Now, consider the following equation

$$\frac{\partial \vec{E}_x}{\partial t} = \frac{1}{\epsilon_x}\left[\left(\frac{\partial H_z}{\partial y} - \frac{\partial H_y}{\partial z}\right) - \sigma_x^e \vec{E}_x - \vec{J_{ix}}\right] \tag{B.48}$$

This equation can be represented in the following form by applying the discretization approach as discussed before.

$$\begin{aligned}\frac{E_x^{n+1}(i,j,k) - E_x^n(i,j,k)}{\Delta t} =& \frac{1}{\epsilon_x(i,j,k)}\frac{H_z^{n+\frac{1}{2}}(i,j,k) - H_z^{n+\frac{1}{2}}(i,j-1,k)}{\Delta y} \\ &- \frac{1}{\epsilon_x(i,j,k)}\frac{H_y^{n+\frac{1}{2}}(i,j,k) - H_y^{n+\frac{1}{2}}(i,j,k-1)}{\Delta z} \\ &- \frac{\sigma_x^e}{\epsilon_x(i,j,k)}E^{n+\frac{1}{2}}(i,j,k) \\ &- \frac{1}{\epsilon_x(i,j,k)}J_{ix}^{n+\frac{1}{2}}(i,j,k)\end{aligned} \tag{B.49}$$

Here, as is clear that electric field is sampled at only integer time instants so as the electric field component at $\left(n+\frac{1}{2}\right)^{th}$ time needs to be replaced by something appropriate. Thus an approximation is done as

$$E_x^{n+\frac{1}{2}}(i,j,k) = \frac{E_x^{n+1}(i,j,k) + E_x^n(i,j,k)}{2} \tag{B.50}$$

Here, component of electric field at $\left(n+\frac{1}{2}\right)^{th}$ time instant is represented as the average of electric field components at n^{th} and $(n+1)^{th}$ time instants. After some manipulations, following equation is obtained

$$\begin{aligned}\frac{2\epsilon_x(i,j,k)+\Delta t\sigma_x^e(i,j,k)}{2\epsilon_x(i,j,k)}E_x^{n+1}(i,j,k) =& \frac{2\epsilon_x(i,j,k)-\Delta t\sigma_x^e(i,j,k)}{2\epsilon_x(i,j,k)}E_x^n(i,j,k)\\ &- \frac{2\Delta t}{\epsilon_x(i,j,k)\Delta y}\left(H_z^{n+\frac{1}{2}}(i,j,k)-H_z^{n+\frac{1}{2}}(i,j-1,k)\right)\\ &- \frac{2\Delta t}{\epsilon_x(i,j,k)\Delta z}\left(H_y^{n+\frac{1}{2}}(i,j,k)-H_y^{n+\frac{1}{2}}(i,j,k-1)\right)\\ &- \frac{2\Delta t}{\epsilon_x(i,j,k)}J_{ix}^{n+\frac{1}{2}}(i,j,k)\end{aligned} \tag{B.51}$$

Final updating equation for the x-component of electric field can be written as

$$\begin{aligned}E_x^{n+1}(i,j,k) =& \frac{2\epsilon_x(i,j,k)-\Delta t\sigma_x^e(i,j,k)}{2\epsilon_x(i,j,k)+\Delta t\sigma_x^e(i,j,k)}E_x^n(i,j,k)\\ &- \frac{2\Delta t}{\left(2\epsilon_x(i,j,k)+\Delta t\sigma_x^e(i,j,k)\right)\Delta y}\left(H_z^{n+\frac{1}{2}}(i,j,k)-H_z^{n+\frac{1}{2}}(i,j-1,k)\right)\\ &- \frac{2\Delta t}{\left(2\epsilon_x(i,j,k)+\Delta t\sigma_x^e(i,j,k)\right)\Delta z}\left(H_y^{n+\frac{1}{2}}(i,j,k)-H_y^{n+\frac{1}{2}}(i,j,k-1)\right)\\ &- \frac{2\Delta t}{2\epsilon_x(i,j,k)+\Delta t\sigma_x^e(i,j,k)}J_{ix}^{n+\frac{1}{2}}(i,j,k)\end{aligned} \tag{B.52}$$

Now consider the magnetic field component in x-direction changing with respect to time

$$\frac{\partial\vec{H}_x}{\partial t}=\frac{1}{\mu_x}\left[\left(\frac{\partial E_y}{\partial z}-\frac{\partial E_z}{\partial y}\right)-\sigma_x^m\vec{H}_x-\vec{M}_{ix}\right] \tag{B.53}$$

This equation can also be represented in the following form by applying the

discretization approach as discussed before.

$$\begin{aligned}\frac{H_x^{n+\frac{1}{2}}(i,j,k) - H_x^{n-\frac{1}{2}}(i,j,k)}{\Delta t} =& \frac{1}{\mu_x(i,j,k)} \frac{E_y^n(i,j,k+1) - E_y^n(i,j,k)}{\Delta z} \\ &- \frac{1}{\mu_x(i,j,k)} \frac{E_z^n(i,j+1,k) - E_z^n(i,j,k)}{\Delta y} \\ &- \frac{\sigma_x^m}{\mu_x(i,j,k)} H_x^n(i,j,k) \\ &- \frac{1}{\mu_x(i,j,k)} M_{ix}^n(i,j,k)\end{aligned} \tag{B.54}$$

Here, as is clear that magnetic field is sampled at only half integer time instants so as the magnetic field component at n^{th} time needs to be replaced by something appropriate. Thus an approximation is done as

$$H_x^n(i,j,k) = \frac{H_x^{n+\frac{1}{2}}(i,j,k) + H_x^{n-\frac{1}{2}}(i,j,k)}{2} \tag{B.55}$$

After some manipulations, final updating equation for the x-component of magnetic field can be written as

$$\begin{aligned}H_x^{n+\frac{1}{2}}(i,j,k) =& \frac{2\mu_x(i,j,k) - \Delta t \sigma_x^m(i,j,k)}{2\mu_x(i,j,k) + \Delta t \sigma_x^m(i,j,k)} H_x^{n-\frac{1}{2}}(i,j,k) \\ &- \frac{2\Delta t}{\left(2\mu_x(i,j,k) + \Delta t \sigma_x^m(i,j,k)\right)\Delta z} \left(E_y^n(i,j,k+1) - E_y^n(i,j,k)\right) \\ &- \frac{2\Delta t}{\left(2\mu_x(i,j,k) + \Delta t \sigma_x^m(i,j,k)\right)\Delta y} \left(E_z^n(i,j+1,k) - E_z^n(i,j,k)\right) \\ &- \frac{2\Delta t}{2\mu_x(i,j,k) + \Delta t \sigma_x^m(i,j,k)} M_{ix}^n(i,j,k)\end{aligned} \tag{B.56}$$

Thus by using similar discretization approach, all the updating equations of both electric and magnetic field can be derived. To make these equations simpler to understand and to use in computer programming of FDTD method, coefficient matrix approach is used to represent all the updating equations. Coefficient matrix

representation of updating equations is given as,

a. X-component of Electric Field

$$\begin{aligned} E_x^{n+1}(i,j,k) =& C_{exe}(i,j,k) \times E_x^n(i,j,k) \\ & C_{exhy}(i,j,k) \times \left(H_z^{n+\frac{1}{2}}(i,j,k) - H_z^{n+\frac{1}{2}}(i,j-1,k) \right) \\ & C_{exhz}(i,j,k) \times \left(H_y^{n+\frac{1}{2}}(i,j,k) - H_y^{n+\frac{1}{2}}(i,j,k-1) \right) \\ & C_{exj}(i,j,k) \times J_{ix}^{n+\frac{1}{2}}(i,j,k) \end{aligned} \tag{B.57}$$

Where,

$$C_{exe}(i,j,k) = \frac{2\epsilon_x(i,j,k) - \Delta t \sigma_x^e(i,j,k)}{2\epsilon_x(i,j,k) + \Delta t \sigma_x^e(i,j,k)} \tag{B.58}$$

$$C_{exhy}(i,j,k) = \frac{2\Delta t}{\left(2\epsilon_x(i,j,k) + \Delta t \sigma_x^e(i,j,k)\right) \Delta y} \tag{B.59}$$

$$C_{exhz}(i,j,k) = \frac{2\Delta t}{\left(2\epsilon_x(i,j,k) + \Delta t \sigma_x^e(i,j,k)\right) \Delta z} \tag{B.60}$$

$$C_{exj}(i,j,k) = \frac{2\Delta t}{2\epsilon_x(i,j,k) + \Delta t \sigma_x^e(i,j,k)} \tag{B.61}$$

b. Y-component of Electric Field

$$\begin{aligned} E_y^{n+1}(i,j,k) =& C_{eye}(i,j,k) \times E_y^n(i,j,k) \\ & C_{eyhx}(i,j,k) \times \left(H_x^{n+\frac{1}{2}}(i,j,k) - H_x^{n+\frac{1}{2}}(i,j,k-1) \right) \\ & C_{eyhz}(i,j,k) \times \left(H_z^{n+\frac{1}{2}}(i,j,k) - H_z^{n+\frac{1}{2}}(i-1,j,k) \right) \\ & C_{eyj}(i,j,k) \times J_{iy}^{n+\frac{1}{2}}(i,j,k) \end{aligned} \tag{B.62}$$

Where,

$$C_{eye}(i,j,k) = \frac{2\epsilon_y(i,j,k) - \Delta t\sigma_y^e(i,j,k)}{2\epsilon_y(i,j,k) + \Delta t\sigma_y^e(i,j,k)} \tag{B.63}$$

$$C_{eyhx}(i,j,k) = \frac{2\Delta t}{\left(2\epsilon_y(i,j,k) + \Delta t\sigma_y^e(i,j,k)\right)\Delta z} \tag{B.64}$$

$$C_{eyhz}(i,j,k) = \frac{2\Delta t}{\left(2\epsilon_y(i,j,k) + \Delta t\sigma_y^e(i,j,k)\right)\Delta x} \tag{B.65}$$

$$C_{eyj}(i,j,k) = \frac{2\Delta t}{2\epsilon_y(i,j,k) + \Delta t\sigma_y^e(i,j,k)} \tag{B.66}$$

c. Z-component of Electric Field

$$\begin{aligned} E_z^{n+1}(i,j,k) =& C_{eze}(i,j,k) \times E_z^n(i,j,k) \\ & C_{ezhy}(i,j,k) \times \left(H_y^{n+\frac{1}{2}}(i,j,k) - H_y^{n+\frac{1}{2}}(i-1,j,k)\right) \\ & C_{ezhx}(i,j,k) \times \left(H_x^{n+\frac{1}{2}}(i,j,k) - H_x^{n+\frac{1}{2}}(i,j-1,k)\right) \\ & C_{ezj}(i,j,k) \times J_{iz}^{n+\frac{1}{2}}(i,j,k) \end{aligned} \tag{B.67}$$

Where,

$$C_{eze}(i,j,k) = \frac{2\epsilon_z(i,j,k) - \Delta t\sigma_z^e(i,j,k)}{2\epsilon_z(i,j,k) + \Delta t\sigma_z^e(i,j,k)} \tag{B.68}$$

$$C_{ezhy}(i,j,k) = \frac{2\Delta t}{\left(2\epsilon_z(i,j,k) + \Delta t\sigma_z^e(i,j,k)\right)\Delta x} \tag{B.69}$$

$$C_{ezhx}(i,j,k) = \frac{2\Delta t}{\left(2\epsilon_z(i,j,k) + \Delta t\sigma_z^e(i,j,k)\right)\Delta y} \tag{B.70}$$

$$C_{ezj}(i,j,k) = \frac{2\Delta t}{2\epsilon_z(i,j,k) + \Delta t\sigma_z^e(i,j,k)} \tag{B.71}$$

d. X-component of magnetic field

$$\begin{aligned} H_x^{n+\frac{1}{2}}(i,j,k) =& C_{hxh}(i,j,k) \times H_x^{n-\frac{1}{2}}(i,j,k) \\ & C_{hxhy}(i,j,k) \times \left(E_y^n(i,j,k+1) - E_y^n(i,j,k)\right) \\ & C_{hxhz}(i,j,k) \times \left(E_z^n(i,j+1,k) - E_z^n(i,j,k)\right) \\ & C_{hxm}(i,j,k) M_{ix}^n(i,j,k) \end{aligned} \tag{B.72}$$

Where,

$$C_{hxh}(i,j,k) = \frac{2\mu_x(i,j,k) - \Delta t \sigma_x^m(i,j,k)}{2\mu_x(i,j,k) + \Delta t \sigma_x^m(i,j,k)} \tag{B.73}$$

$$C_{hxhy}(i,j,k) = \frac{2\Delta t}{\left(2\mu_x(i,j,k) + \Delta t \sigma_x^m(i,j,k)\right)\Delta z} \tag{B.74}$$

$$C_{hxhz}(i,j,k) = \frac{2\Delta t}{\left(2\mu_x(i,j,k) + \Delta t \sigma_x^m(i,j,k)\right)\Delta y} \tag{B.75}$$

$$C_{hxm}(i,j,k) = \frac{2\Delta t}{2\mu_x(i,j,k) + \Delta t \sigma_x^m(i,j,k)} \tag{B.76}$$

e. Y-component of magnetic field

$$\begin{aligned} H_y^{n+\frac{1}{2}}(i,j,k) =& C_{hyh}(i,j,k) \times H_y^{n-\frac{1}{2}}(i,j,k) \\ & C_{hyhz}(i,j,k) \times \left(E_z^n(i+1,j,k) - E_z^n(i,j,k)\right) \\ & C_{hyhx}(i,j,k) \times \left(E_x^n(i,j,k+1) - E_x^n(i,j,k)\right) \\ & C_{hym}(i,j,k) \times M_{iy}^n(i,j,k) \end{aligned} \tag{B.77}$$

Where,

$$C_{hyh}(i,j,k) = \frac{2\mu_y(i,j,k) - \Delta t \sigma_y^m(i,j,k)}{2\mu_y(i,j,k) + \Delta t \sigma_y^m(i,j,k)} \tag{B.78}$$

$$C_{hyhz}(i,j,k) = \frac{2\Delta t}{\left(2\mu_y(i,j,k) + \Delta t\sigma_y^m(i,j,k)\right)\Delta x} \tag{B.79}$$

$$C_{hyhx}(i,j,k) = \frac{2\Delta t}{\left(2\mu_y(i,j,k) + \Delta t\sigma_y^m(i,j,k)\right)\Delta z} \tag{B.80}$$

$$C_{hym}(i,j,k) = \frac{2\Delta t}{2\mu_y(i,j,k) + \Delta t\sigma_y^m(i,j,k)} \tag{B.81}$$

f. Z-component of magnetic field

$$\begin{aligned} H_z^{n+\frac{1}{2}}(i,j,k) =& C_{hzh}(i,j,k) \times H_z^{n-\frac{1}{2}}(i,j,k) \\ & C_{hzhx}(i,j,k) \times (E_x^n(i,j+1,k) - E_x^n(i,j,k)) \\ & C_{hzhy}(i,j,k) \times \left(E_y^n(i+1,j,k) - E_y^n(i,j,k)\right) \\ & C_{hzm}(i,j,k) \times M_{iz}^n(i,j,k) \end{aligned} \tag{B.82}$$

Where,

$$C_{hzh}(i,j,k) = \frac{2\mu_z(i,j,k) - \Delta t\sigma_z^m(i,j,k)}{2\mu_z(i,j,k) + \Delta t\sigma_z^m(i,j,k)} \tag{B.83}$$

$$C_{hzhx}(i,j,k) = \frac{2\Delta t}{(2\mu_z(i,j,k) + \Delta t\sigma_z^m(i,j,k))\Delta y} \tag{B.84}$$

$$C_{hzhy}(i,j,k) = \frac{2\Delta t}{(2\mu_z(i,j,k) + \Delta t\sigma_z^m(i,j,k))\Delta x} \tag{B.85}$$

$$C_{hzm}(i,j,k) = \frac{2\Delta t}{2\mu_z(i,j,k) + \Delta t\sigma_z^m(i,j,k)} \tag{B.86}$$

Thus, Gausss Equations can be directly discretized in the similar manner. Now, having derived FDTD updating equations, a Time Marching Algorithm is used to

set up the problem space including the objects, material types, sources and lumped elements [7]. The algorithm is shown in the figure 5.12. Time marching algorithm starts with setting up the problem space, defining geometry, defining sources, lumped elements, ports and setting all the material parameters. Then the computation of all the field coefficients is done. After determining field coefficients, the magnetic field components are updated at half integer time instants. Now, the electric field coefficients are updated at integer time instants and the boundary conditions are applied. After incrementing the time step to n+1 from n, the loop iteration is checked whether it is last iteration or loop needs to be run again. If it is the last iteration then the loop is stopped and the output is observed.

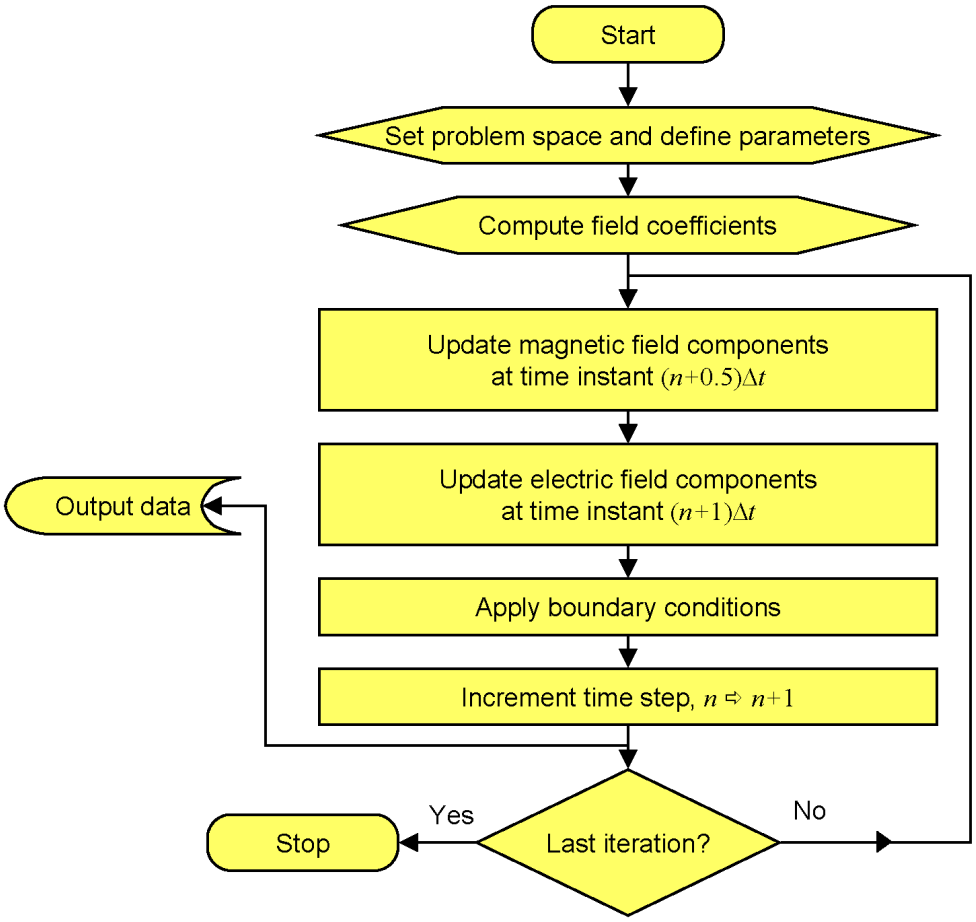

Figure B.12: Time Marching Algorithm

List of Publications during Thesis

In this research work, following research publications have been carried out. There are 3 International conference papers and 2 Journal papers.

1 **International Conference Papers**

a. V. Dhoot and S. Gupta, "Full Wave Analysis of a Novel Multifractal Multiband Antenna using 3D-FDTD Approach", *International Conference on Communications and Signal Processing*, Calicut, Kerala State, India, Pg. No. 261-265, Feb. 2011.

b. V. Dhoot and S. Gupta, "Return Loss Validation of a Novel Cantor based Antenna using FIT and FDTD", *International Conference on Communications and Signal Processing*, Calicut, Kerala State, India, Pg. No. 374-378, Feb. 2011.

c. V. Dhoot and S. Gupta, "A Novel Revised Cantor Geometry based Multifractal Multiband Monopole Antenna using 3D-FDTD Approach", *Antenna Test and Measurement Society Conference*, ATMS, 2012.

2 **Published Journal Papers**

d. V. Dhoot and S. Gupta, "Design and Analysis of a Novel Multifractal Multiband Antenna using 3D-FDTD Method", *International Journal of Applied Engineering Research*, Vol. 9, No. 20, 2014.

e. V. Dhoot and S. Gupta, "Multiband Fractal Antenna for Mobile & Tablet PCs covering LTE, UMTS, GSM and WLAN Applications", *International Journal of Microwave and Optical Technology*, Vol. 10, No. 2, March 2015.

REFERENCES

[1] D. J. Griffiths, Introduction to electrodynamics, *Third Edition. Prentice Hall Inc.*, ISBN 0-13-805326-X, pp. 13-20, 321-331, 1999.

[2] D. M. Pozar and D. H. Schaubert, Microstrip Antennas, *United States of America, IEEE Press*, ISBN 0-7803-1078-0, 1995.

[3] C. A. Balanis, Antenna Theory Analysis and Design, *Second Edition. John Wiley & Sons*, ISBN 0-471-59268, pp. 734-745, 1997.

[4] P. Bhartia, Millimeter-Wave Microstrip and Printed Circuit Antennas, *Mass. Artech House*, ISBN 0-8900-6333-8, 1991.

[5] T. Weiland, "A discretization method for the solution of Maxwell's equations for six-component fields", *Internation Journal of Electronics and Communication (AEU)*, vol. 31, no. 3, pp. 116-120, 1977.

[6] T. Weiland, "Time domain electromagnetic field computation with finite difference methods", *Int J. Num. Mod.*, vol. 9, no. 4, pp. 259-319, 1996.

[7] B. Manimegalai, S. Raju and V. Abhaikumar, "A Multifractal Cantor Antenna for Multiband Wireless Applications", *IEEE Antennas and Wireless Propagation Letters*, vol. 8, pp. 359-362, 2009.

[8] B. B. Madelbrot, The Fractal Geometry of Nature, *New York: W.H. Freeman*, ISBN-13: 978-0-71671-186-5, 1983.

[9] H. O. Peitgen, H. Jurgens, and D. Saupe, Chaos and Fractals: New Frontiers of Science, *New York: Springer-Verlag*, ISBN-13: 978-0-38720-229-7, 1992.

[10] C. Puente, J. Romeu, R. Bartoleme and R. Pous, "Fractal multiband antenna based on Sierpinski gasket", *Electron. Lett.*, vol. 32, no. 1, pp. 1-2, 1996.

[11] C. Puente-Baliarda, J. Romeu, R. Pous and A. Cardama, "On the behavior of the Sierpinski multiband fractal antenna," *IEEE Trans. Ant. Propagat.*, vol. 46, no. 4, pp. 517- 524, 1998.

[12] J. Yeo and R. Mittra, "Modified Sierpinski gasket patch antnna for multi-band applications," *IEEE AP-S Inter. Conf. 2001*, vol. 3, pp. 134-147, 2001.

[13] M. Navarro, J. M. Gonzalez, C. Puente, J. Romeu and A. Aguasca, "Self-similar surface current distribution on fractal Sierpinski antenna verified with infra-red thermograms," *IEEE-APS International Conf.*, pp. 1566-1569, 1999.

[14] C. Puente, J. Romeu, R. Bartoleme and R. Pous, "Perturbation of the Sierpinski antenna to allocate operating bands," *Electron. Lett.*, vol. 32, no. 24, pp. 2186-2187, 1996.

[15] C. T. P. Song, P. S. Hall, H. Ghafouri-Shiraz and D. Wake, "Sierpinski monopole antenna with controlled band spacing and input impedance," *Electron. Lett.*, vol. 35, no. 13, pp. 1036-1037, 1999.

[16] C. Puente, M. Navarro, J. Romeu and R. Pous, "Variations on the fractal Sierpinski antenna flare angle," *IEEE-APS International Conf.*, pp. 2340-2343, 1998.

[17] G. J. Walker and J. R. James, "Fractal volume antennas," *Electron. Lett.*, vol. 34, no. 16, pp. 1536-1537, 1998.

[18] N. Cohen, "Fractal antenna applications in wireless telecommunications," *IEEE Professional Program Proc. of Electronics Industries Forum of New England, 1997*, pp. 43-49, 1997.

[19] C. Puente-Baliarda, J. Romeu, R. Pous, J. Ramis and A. Hijazo, "Small but long Koch fractal monopole," *IEEE Electron. Lett.*, vol. 34, no. 1, pp. 9-10, 1998.

[20] C. P. Baliarda, J. Romeu and A. Cardama, "The Koch monopole: A small fractal antenna," *IEEE Trans. Ant. Propagat.*, vol. 48, no. 11, pp. 1773-1781, 2000.

[21] J. P. Glanvittorio and Y. Rahmaat-Samii, "Fractal element antennas: A compilations of configurations with novel characteristics," *IEEE AP-S Inter. Symp. 2000*, pp. 1688-1691, 2000.

[22] D. H. Werner, P. L. Werner and K. H. Church, "Genetically engineered multiband fractal antennas," *Electron. Lett.*, vol. 37, no. 19, pp. 1150-1151, 2001.

[23] X. Liang and M. Y. W. Chia, "Multiband characteristics of two fractal antennas," *Microw. & Opt. Technol. Lett.*, vol. 23, no. 4, pp. 242-245, 1999.

[24] V. Dhoot and S. Gupta, "A Novel Revised Cantor Geometry based Multifractal Multiband Monopole Antenna using 3D-FDTD Approach," *Antenna Test & Measurement Society*, pp. 15-19 Feb. 2012.

[25] V. Dhoot and S. Gupta, "Full wave analysis of a novel multifractal multiband antenna using 3D-FDTD approach," *IEEE International Conference on Communications and Signal Processing (ICCSP), 2011*, pp.261-265, 10-12 Feb. 2011.

[26] R. T. Stevens, Fractal Programming in C, *Redwood City, CA: M&T Books*, 1989.

[27] D. H. Werner, A. Rubio Bretones and B.R. Long, "Radiation characteristics of thinwire ternary fractal trees," *IEEE Electron. Lett.*, vol. 35, no. 8, pp. 609-610, 1999.

[28] J. P. Glanvittorio and Y. Rahmaat-Samii, "Fractal element antennas: A compilations of configurations with novel characteristics," *IEEE AP-S Inter. Symp. 2000*, pp. 1688-1691, 2000.

[29] K. J. Vinoy, K. A. Jose, V. K. Varadan and V. V. Varadan, "Hilbert curve fractal antenna: a small resonant antenna for VHF/UHF applications," *Microwave & Optical Technology Letters*, vol. 29, no. 4, pp. 215-219, 2001.

[30] J. M. Gibney and W. S. T. Rowe, "An investigation into the Practicality Of Using a stage four Hilbert Curve Fractal Antenna for electronic warfare applications," *Asia-Pacific Microwave Conference Proceedings (APMC), 2011*, pp.817-820, 5-8 Dec. 2011

[31] Zhu. Jinhui, A. Hoorfar and N. Engheta, "Bandwidth, cross-polarization, and feed-point characteristics of matched Hilbert antennas," *IEEE Antennas and Wireless Propagation Letters*, vol.2, no.1, pp.2-5, 2003.

[32] J. Pourahmadazar, C. Ghobadi and J. Nourinia, "Novel Modified Pythagorean Tree Fractal Monopole Antennas for UWB Applications," *IEEE Antennas and Wireless Propagation Letters*, vol.10, no. 1, pp.484-487, 2011.

[33] V. Dhoot and S. Gupta, "Return loss validation of a novel cantor based antenna using FIT and FDTD," *IEEE International Conference on Communications and Signal Processing (ICCSP), 2011*, pp.374-378, 10-12, Feb. 2011.

[34] A. Taflove, Computational Electrodynamics: The Finite-Difference Time-Domain Method, *Artech House Norwood*, ISBN: 978-1-58053-832-9, 1995.

[35] K. S. Kunz and R. J. Luebbers, The Finite Difference Time Domain Method for Electromagnetics, *CRC Press Boca Raton,*, ISBN: 978-0-84938-657-2, 1993.

[36] G. Chambers, "Propagation in Waveguide filled Longitudinally with two or more Dielectrics", *Br. J. Appl. Phys.*, vol. 4, pp. 39-45, Feb. 1953

[37] J. M. Catala-Civera,, A. J. Canos, F. L. Penaranda-Foix, E. de los Reyes Davo, "Acurate Determination of the Complex Permittivity of material with Transmission Reflection Measurement in Partially filled Rectangular Waveguide", *IEEE Trans. Microw. Theory Tech.*, vol. 51, no. 1 pp. 16-24, 2003.

[38] C. A. Balanis, Advanced Engineering Electromagnetics, *John Wiley & Sons, New Jersey, NJ*, 2nd Edition, ISBN 978-0-470-58948-9, 2012.

[39] R. F. Harrington, Time-Harmonic Electromagnetic Fields, *John Wiley & Sons and IEEE Press, New York, NY*, ISBN 13: 978-0-07026-745-9, 2001.

[40] R. E. Collin, Field Theory of Guided Waves, *IEEE Press, New York, NY*, ISBN: 978-0-87942-237-0, 1991.

[41] N. Marcuvitz, Waveguide Handbook, *McGraw-Hill, New York, NY*, ISBN 13: 978-0-86341-058-1, 1951.

[42] S. N. Sinha and M. Jain, "A self-affine fractal multiband antenna," *IEEE Antennas Wireless Propag. Lett.,* vol. 6, pp. 110-112, 2007.

[43] A. Z. Elsherbeni and V. Demir, The Finite-Difference Time-Domain Method for Electromagnetics with MATLAB Simulations, *SciTech Publishing, Inc.*, ISBN 9-78974-6521-04-8, 2009.

[44] W. Kainz, A. Christ, T. Kellom, S. Seidman, N. Nikoloski, B. Beard and N. Kuster, "Dosimetric comparison of the specific anthropomorphic mannequin (SAM) to 14 anatomical head models using a novel definition for the mobile phone positioning", *Physics in Medicine and Biology*, vol. 50, no. 14, pp. 3423, 2005, ISSN: 00319155.

[45] M. A. Jensen and Y. Rahmat-Samii, "EM interaction of handset antennas and a human in personal communications," *Proceedings of the IEEE* , vol. 83, no. 1, pp. 7,17, Jan 1995.

[46] O. P. Gandhi, G. Lazzi and C. M. Furse, "Electromagnetic absorption in the human head and neck for mobile telephones at 835 and 1900 MHz," *IEEE Transactions on Microwave Theory and Techniques*, vol. 44, no.10, pp. 1884,1897, Oct 1996.

[47] K. Zhao, S. Zhang, Z. Ying, T. Bolin and S. He, "SAR Study of Different MIMO Antenna Designs for LTE Application in Smart Mobile Handsets," *IEEE Transactions on Antennas and Propagation*, vol. 61, no. 6, pp. 3270,3279, June 2013.

[48] S.-H. Chang and W.-J. Liao, "A Broadband LTE/WWAN Antenna Design for Tablet PC," *IEEE Transactions on Antennas and Propagation*, vol. 60, no. 9, pp. 4354-4359, Sept. 2012.

[49] X. Zhou, X. Quan and R. Li, "A Dual-Broadband MIMO Antenna System for GSM/UMTS/LTE and WLAN Handsets," *IEEE Antennas and Wireless Propagation Letters*, vol.11, pp. 551-554, 2012.

[50] S. Barbarino and F. Consoli, "UWB Circular Slot Antenna provided with an Inverted-L Notch Filter for the 5 GHz WLAN Band", *Progress In Electromagnetic Research*, vol. 104, pp. 1-13, 2010

[51] Z. Chen, Y.-L. Ban, J.-H. Chen, L.-W. Li and Y.-J. Wu, "Bandwidth Enhancement of LTE/WWAN Printed Mobile Phone Antenna using Slotted Gound Structure", *Progress In Electromagnetic Research*, vol. 129, pp. 469-483, 2012

[52] Z. Chen, Y.-L. Ban, S.-C. Sun and J. L.-W. Li, "Printed antenna for penta-band wwan tablet computer application using embedded parallel resonant structure," *Progress In Electromagnetic Research*, vol. 136, pp. 725-737, 2013.

[53] J. Dong, Y.-C. Jiao, Z.-B. Weng, Q. Qiu and Y. Chen, "A coupled-fed antenna for 4g mobile handset," *Progress In Electromagnetic Research*, vol. 141, pp. 727-737, 2013.

[54] C. Yoon, S.-G. Hwang, G.-C. Lee, W.-S. Kim, H.-C. Lee, C.-H. Lee and H.-D. Park, "A frequency-selecting technique for mobile handset antennas based on capacitance switching," *Progress In Electromagnetic Research*, vol. 138, pp. 99-113, 2013.

[55] K. Zhao, S. Zhang, Z. Ying, T. Bolin and S. He, "Reduce the hand-effect body loss for lte mobile antenna in ctia talking and data modes," *Progress In Electromagnetic Research*, vol. 137, pp. 73-85, 2013.

[56] H.-H. Chou, H.-T. Hsu, H.-T. Chou, K.-H. Liu and F.-Y. Kuo, "Reduction of peak SAR in human head for handset applications with resistive sheets (r-cards)," *Progress In Electromagnetic Research*, vol. 94, pp. 281-296, 2009.

[57] M. T. Islam, Faruque, M. R. I. and Misran, N., "Design analysis of ferrite sheet attachment for SAR reduction in human head," *Progress In Electromagnetic Research*, vol. 98, pp. 191-205, 2009.

[58] S. H. Ronald, M. F. B. A. Malek, S. I. S. Hassan, E. M. Cheng, M. H. Mat, M. S. Zulkefli and S. F. Binti Maharimi, "Designing asian-sized hand model for SAR determination at gsm900/1800: simulation part," *Progress In Electromagnetic Research*, vol. 129, pp. 439-467, 2012.

[59] L.-Y. Kong, J. Wang, and W.-Y. Yin, "A novel dielectric conformal FDTD method for computing SAR distribution of the human body in a metallic cabin illuminated by an intentional electromagnetic pulse (iemp)," *Progress In Electromagnetic Research*, vol. 126, pp. 355-373, 2012.

[60] M. Zhang and A. Alden, "Calculation of whole-body SAR from a 100 MHz dipole antenna," *Progress In Electromagnetic Research*, vol. 119, pp. 133-153, 2011.

[61] A. H. Kusuma, A.-F. Sheta, I. M. Elshafiey, Z. Siddiqui, M. A. S. Alkanhal, S. Aldosari, S. A. Alshebeili and S. F. Mahmoud, "A new low SAR antenna structure for wireless handset applications," *Progress In Electromagnetic Research*, vol. 112, pp. 23-40, 2011.

[62] M. H. Mat, M. F. B. A. Malek, W. G. Whittow, S. H. Ronald, M. S. Zulkefli, N. Saudin and L. Mohamed, "The influence of human head model wearing metal-frame spectacles to the changes of SAR and antenna gain: simulation of frontal face exposure," *Progress In Electromagnetic Research*, vol. 137, 453-473, 2013.

[63] *Computer Simulation Technology*, Web Address - http://www.cst.com.

[64] M. Okoniewski and M. A. Stuchly, "A study of the handset antenna and human body interaction," *IEEE Transactions on Microwave Theory and Techniques*, vol.44, no. 10, pp. 1855,1864, Oct 1996.

[65] K. H. Chan, C. K. Tang, L. C. Fung, S. W. Leung and Y. M. Siu, "Study of using fractional phantom head model on SAR evaluation in mobile antenna design", *Electromagnetic Compatibility and 19th International Zurich Symposium on Electromagnetic Compatibility*, pp. 28-35, APEMC 2008.

[66] C.-H. Li, M. Douglas, E. Ofli, B. Derat, S. Gabriel, N. Chavannes and N. Kuster, "Influence of the Hand on the Specific Absorption Rate in the Head", *IEEE Transactions on Antennas and Propagation*, vol. 60, no. 2, pp. 1066-1074, Feb. 2012.

[67] A. Gasmelseed and J. Yunus, "SAR Calculations in Human Head Model Extracted from Thermal Infrared Images", *Fourth Asia International Conference on*

Mathematical/Analytical Modelling and Computer Simulation (AMS), pp. 253 - 257, 2010.

[68] Z. Wang, X. Chen and C. G. Parini, "Effects of the ground and the human body on the performance of a handset antenna", *IEE Proceedings on Microwaves Antennas and Propagation*, vol. 151, no. 2, pp. 131, 2004, ISSN: 13502417.

[69] V. K. Varadan, K. A. Jose, V. V. Varadan, R. Hughes and J. F. Kelley, "Novel microwave planar phase shifter," *Microwave J.,* vol. 38, 1995.

[70] K. A. Jose, V. K. Varadan and V. V. Varadan, "Electronically tunable Microstrip patch antenna," *Microwave Opt. Technol. Lett.,* vol. 20, no. 1, pp. 166-169, 1999.

[71] V. K. Varadan, F. Selmi and V. V. Varadan, "Voltage tunable dielectric ceramics which exhibit low dielectric constants and applications thereof to antenna structures," US Patent , no. 5557286, Sep. 17,1996.

[72] S. B. Herner, F. Selmi, V. V. Varadan and V. K. Varadan, "Effect of various dopants on the dielectric properties of barium strontium titanate," *Materials Lett.*, vol. 15, no. 5, pp. 317-324, 1993.

[73] R. Ro, V. V. Varadan and V. K. Varadan, "Electromagnetic activity and absorption in microwave chiral composites," *IEE Proc. Pt. H, Microwaves, Antennas and Propagation,* vol. 139, no. 5, pp. 441-448, 1992.

[74] T. Guire, V. V. Varadan and V. K. Varadan, "Influence of chirality on the reflection of EM waves by planar dielectric slabs," *IEEE Trans. Electromag. Compat.,* vol. 32, no. 4, pp. 300-303, 1990.

[75] V. V. Varadan, R. Ro and V. K. Varadan, "Measurement of electromagnetic properties of chiral composite materials in 8-40 GHz range," *Radio Science,* vol. 29, no. 1, pp. 9-22, 1994.

[76] R. Munson, "Conformal Microstrip antennas and Microstrip phased arrays," *Antennas and Propagation, IEEE Transactions on,* vol.22, no.1, pp.74,78, Jan 1974.

[77] J. Howell, "Microstrip antennas," *IEEE Transactions on Antennas and Propagation,* vol.23, no.1, pp.90,93, Jan 1975.

[78] R. J. Mailloux, F. McilvennaJohn and N. Kernweis, "Microstrip array technology," *Antennas and Propagation, IEEE Transactions on,* vol.29, no.1, pp.25,37, Jan 1981.

[79] D. M. Pozar, "Considerations for millimeter wave printed antennas," *Antennas and Propagation, IEEE Transactions on*, vol.31, no.5, pp.740,747, Sep 1983.

[80] D. M. Pozar, "Microstrip antennas," *Proceedings of the IEEE*, vol.80, no.1, pp.79,91, Jan 1992.

[81] K. F. Lee and K. M. Luk, Microstrip Patch Antennas, *Imperial College Press*, ISBN: 978-1-84816-453-6, 2010.

[82] R. B. Waterhouse, Microstrip Patch Antennas: A Designer's Guide, *Kluwer Academic Publishers*, ISBN: 978-1-40207-373-1, 2003.

[83] L. Zhang, W. Zhang, Y.-P. Zhang, "Microstrip Grid and Comb Array Antennas," *Antennas and Propagation, IEEE Transactions on*, vol.59, no.11, pp.4077,4084, Nov. 2011.

[84] Y. Hayashi, K. Sakakibara, M. Nanjo, S. Sugawa, N. Kikuma and H. Hirayama, "Millimeter-Wave Microstrip Comb-Line Antenna Using Reflection-Canceling Slit Structure," *Antennas and Propagation, IEEE Transactions on*, vol.59, no.2, pp.398,406, Feb. 2011.

[85] K. Chang, R. A. York, P. S. Hall and T. Itoh, "Active Integrated Antennas", *IEEE Transactions on Microwave Theory and Techniques*, vol. 50, no. 3, pp.937-944, March 2002.

[86] W. Ismail and P. Gardner, "Low Noise Integrated Active Antenna As Image Reject Mixer (IRM)", *High Frequency Postgraduate Student Colloquium, 2001. 6th IEEE*, pp.125-129, 2001.

[87] M. K. A. Rahim, W. K. Chong and T. Masri, "Active Integrated Antenna with Image Reject Mixer Design", *European Conference on Antennas and Propagation*, pp. 1-4, 2007.

[88] S. Gupta and V. F. Fusco, "Tracking Antenna Architectures Based on a Planar Two-Port Microstrip Patch Mixer Antenna",*IEEE Transactions on Antennas and Propagation*, vol. 45, no. 12, pp. 1863 - 1868, December 1997.

[89] G. Yun, "Compact oscillator-type active antenna for UHF RFID reader", *Electronics Letters*, vol. 43, no. 6, pp. 3-4, March 2007.

[90] D. Bonefaeie and J. Bartolie, "Design Considerations of an Active Integrated Antenna with Negative Resistance Transistor Oscillator", *Radioengineering*, vol. 14, no. 4, pp. 33-39, December 2005.

[91] Y. Zhang, P. Gardner, H. Ghafouri-Shiraj and P. S. Hall, "FDTD Anallysis of Microwave Active Antenna including Nonlinear Model of FET Transistor", 3^{rd} *International Conference on Microwave and Millimeter Wave Technology Proceedings*, pp. 628-621, 2002.

[92] Y. Qin, S. Gao and A. Sarnbell, "Broadband High-Efficiency Circularly Polarized Active Antenna and Array for RF Front-End Application", *IEEE Transactions on Microwave Theory and Techniques*, vol. 54, no. 7, pp. 2910-2916, July 2006.

[93] Y. Qian and T. Itoh, "Progress in Active Integrated Antennas and Their Applications", *IEEE Transactions on Microwave Theory and Techniques*, vol. 46, no. 11, pp. 1891-1900, November 1998.

[94] M. J. Cryan and P. S. Hall, "An Integrated Active Circulator Antenna", *IEEE Microwave And Guided Wave Letters,*, vol. 7, no. 7, pp. 190-191, 1997.

[95] B. Manimegalai, S. Raju and V. Abhaikumar, "A PHEMT Frequency Doubling Active Antenna with BPSK Modulation Capability", *IEEE Antennas and Wireless Propagation Letters*, vol. 3, no. 1, pp. 310-313, 2004.

[96] S. Gupta, P. K. Nath and B. K. Sarkar, "Integrated Microstrip Shorted Antenna using Hybrid Active Circulator", *Microwave Conference, 2000 Asia-Pacific,* pp. 719-722, 2000.

[97] K. S. YEE, "Numerical Solution of Initial Boundary Value Problems Involving Maxwells Equations in Isotropic Media", *IEEE Transactions on Antennas and Propagation*, vol. 14, no. 3, pp. 302-307, December 1966.

[98] V. S. Reddy and R. Garg, "An Improved Extended FDTD Formulation for Active Microwave Circuits", *IEEE Transactions on Microwave Theory and Techniques*, vol. 47, no. 9, pp. 1603-1608, November 1999.

[99] W. Sui, D. A. Christensen and C. H. Durney, "Extending the Two-Dimensional FDTD Method to Hybrid Electromagnetic Systems with Active and Passive Lumped Elements", *IEEE Transactions on Microwave Theory and Techniques*, vol. 40, no. 4, pp. 724-730, November 1992.

[100] Y.-S. Tsuei, A. C. Cangellaris and J. L. Prince, "Rigorous Electromagnetic Modeling of Chip-to-Package (First-Level) Interconnections", *IEEE Transactions on Components, Hybrids and Manufacturing Technology*, vol. 16, no. 8, pp. 876-883, December 1993.

[101] M. P. May, A. Taflove and J. Baron, "FD-TD Modeling of Digital Signal Propagation in 3-D Circuits With Passive and Active Loads", *IEEE Transactions on Microwave Theory and Techniques*, vol. 42, no. 8, pp. 1514-1523, November 1994.

[102] C. H. Durney, W. Sui, D. A. Christensen and J. Zhu, "A General Formulation for Connecting Sources and Passive Lumped-Circuit Elements Across Multiple 3-D FDTD Cells", *IEEE Microwave and Guided Wave Letters*, vol. 6, no. 2, pp. 85, February 1996.

[103] V. A. Thomas, M. E. Jones, M. P.- May, A. Taflove and E. Harrigan, "The Use of SPICE Lumped Circuits as Sub-grid Models for FDTD Analysis", *IEEE Microwave and Guided Wave Letters*, vol. 4, no. 5, pp. 141-143, May 1994.

[104] C. -N. Kuo, V. A. Thomas, S. T. Chew, B. Houshmand and T. Itoh, "Small Signal Analysis of Active Circuits Using FDTD Algorithm", *IEEE Microwave and Guided Wave Letters*, vol. 5, no. 7, pp. 216-218, July 1995.

[105] B. Toland, J. Lin, B. Houshmand and T. Itoh, "FDTD Analysis of an Active Antenna", *IEEE Microwave and Guided Wave Letters*, vol. 3, no. 11, pp. 423-425, November 1993.

[106] V. A. Thomas, K.-M. Ling, M. E. Jones, B. Toland, J. Lin and T. Itoh, "FDTD Analysis of an Active Antenna", *IEEE Microwave and Guided Wave Letters*, vol. 4, no. 9, pp. 296-298, September 1994.

[107] B. Toland, B. Houshmand and T. Itoh, "Modeling of Nonlinear Active Regions with the FDTD Method", *IEEE Microwave and Guided Wave Letters*, vol. 3, no. 9, pp. 333-335, September 1993.

[108] C.-N. Kuo, R.-B. Wu, B. Houshmand and T. Itoh, "Modeling of Microwave Active Devices using the FDTD Analysis Based on the Voltage-Source Approach", *IEEE Microwave and Guided Wave Letters*, vol. 6, no. 5, pp. 199-201, May 1996.

[109] A. R. Djordjevic, B. D. Reljin, D. V. ToSiC and T. K. Sarkar, "Transmission-Line Theory Approach to Solution of State Equations for Linear-Lumped Circuits", *IEEE Transactions on Microwave Theory and Techniques*, vol. 4, no. 3, pp. 479-482, March 1996.

[110] D. M. Sheen, S. M. Ali, M. D. Abouzahra and J. A. Kong, "Application of the Three-Dimensional Finite-Difference Time-Domain Method to the Analysis of Planar Microstrip Circuits", *IEEE Transactions on Microwave Theory and Techniques*, vol. 38, no. 7, pp. 849-857, July 1990.

[111] C. C. Haung and T. H. Chu, "Analysis of MESFET injection-locked oscillators in fundamental mode of operation", *IEEE Transactions on Microwave Theory and Techniques*, vol. 42, no. 10, pp. 1851-1857, October 1994.

[112] A. P. Zhao and A. V. Raisanen, "Application of a Simple and Efficient Source Excitation Technique to the FDTD Analysis of Waveguide and Microstrip Circuits", *IEEE Transactions on Microwave Theory and Techniques*, vol. 44, no. 9, pp. 1535-1539, September 1996.

[113] European Standard EN 50357: Evaluation of human exposure to electromagnetic fields from devices used in Electronic Article Surveillance (EAS), Radio frequency Identification (WID) and similar applications, CENELEC, Brussels, October 2001.

[114] European Council Recommendation (1 99915 I9IEC): Council Recommendation of July 12 1999 on the limitation of exposure of the general public to electromagnetic fields (0 Hz to 300 GHz), Official Journal L 199, 30/07/1999,0059-0070.

[115] IEEE Standards Coordinating Committee 28: IEEE Std C95.3-2002 IEEE recommended practice for measurements and computations of radio frequency electromagnetic fields with respect to human exposure to such fields, 100 kHz - 300 GHz, January 13, 2003.

[116] European Standard EN 50361: Basic Standard for the Measurement of Specific Absorption Rate Related to Human Exposure to Electromagnetic Fields from Mobile Phones (300 MHz 3 GHz), CENELEC, Brussels, July 2001.

[117] ICNIRP: Guidelines for Limiting Exposure to Time-varying Electric, Magnetic, and Electromagnetic Fields (up to 300 GHz), *In: Health Physics*, vol. 74, no. 4, pp. 494-522, 1998.

[118] FCC: http://www.fcc.gov/encyclopedia/radio-frequency-safety